METALORGANIC CHEMICAL VAPOR DEPOSITION GROWTH DEVELOPMENT FOR ULTRAVIOLET VERTICAL CAVITY SURFACE EMITTING LASERS

A Thesis
Presented to
The Academic Faculty

by

Yuh-Shiuan Liu

In Partial Fulfillment
of the Requirements for the Degree
Doctor of Philosophy in the
School of Electrical and Computer Engineering

Georgia Institute of Technology
August 2018

METALORGANIC CHEMICAL VAPOR DEPOSITION GROWTH DEVELOPMENT FOR ULTRAVIOLET VERTICAL CAVITY SURFACE EMITTING LASERS

Approved by:

Professor Russell D. Dupuis, Advisor
School of Electrical and Computer Engineering
Georgia Institute of Technology

Professor Stephen E. Ralph
School of Electrical and Computer Engineering
Georgia Institute of Technology

Professor Shyh–Chiang Shen
School of Electrical and Computer Engineering
Georgia Institute of Technology

Professor Fernando A. Ponce
Department of Physics
Arizona State University

Professor P. Douglas Yoder
School of Electrical and Computer Engineering
Georgia Institute of Technology

Date Approved: 20 July 2018

To my family

ACKNOWLEDGEMENTS

I am heartily thankful to my advisor, Professor Russell D. Dupuis, for his direction, enthusiasm, encouragement, and all the support starting from the first day I joined Advanced Materials and Devices Group (AMDG). He provided resources that are incomparable with any other academic laboratories in the world. I am grateful to my Ph.D. thesis committee members Prof. Russell D. Dupuis, Prof. P. Douglas Yoder, Prof. Fernando A. Ponce, Prof. Stephen E. Ralph, and Prof. Shyh-Chiang Shen for all the valuable insight that greatly enriched my work.

Thanks also goes to all the past and current colleagues in AMDG especially to Dr. Zachory Lochner, Dr. Young Jae Park, and visiting scholar Dr. Weichen Yang and Prof. Ping Chen. I would like to extend my appreciations to my colleagues in the Semiconductor Research Laboratory, Computational Electronics and Photonics Group, and Prof. Ponce's Group at Arizona State University. I especially want to thank Prof. Shyh-Chiang Shen, Prof. P. Douglas Yoder, and Prof. Fernando A. Ponce for leading their group in developing fabrication processes, simulations for the UV–laser diode design, and material characterizations, respectively. I'm grateful to have assistances from Yi–Che (Steven) Lee (SRL), Tsung–Ting (Louis) Kao (SRL), Md. Mahbub Satter (CEPG), Karan Mehta (CEPG), Hongen Xie (ASU), and Shuo Wang (ASU) assisted me throughout the course. I would like to give my special thanks to Tsung–Ting (Louis) Kao for being wonderful team players and wonderful friends; especially, to Louis who spent his valuable time training me on fabrication skills and assisting in growth optimization.

This work was supported by the Microsystem Technology Office (MTO) of the Defense Advanced Research Projects Agency (DARPA) under the following contracts:

Compact Mid-Ultraviolet Technology (CMUVT), Micro-Technology for Positioning, Navigation and Timing (micro–PNT), and Atomic Clocks with Enhanced Stability (ACES) are gratefully acknowledged. In addition, I would like to acknowledge the generous support of the Steve W. Chaddick Endowed Fellowship in Electro-Optics at the Georgia Institute of Technology.

Lastly, I would like to express my loving gratitude to my family. My parents, Nai–Ming Liu and Di–Fang Shyng, who gave me all the possible support to complete my goals. Their encouragement and advice are invaluable to me; especially, they taught me the correct attitude in facing all the problems and challenges which is the main driving force for me to complete this work. I am very grateful to my younger brother, Yuh–Chen Liu, for taking care my parents while I was not around. I'm always proud of him. Another special thanks goes to Wanya Huang for all the sacrifices she made for our son and all the love and support throughout my study.

TABLE OF CONTENTS

LIST OF TABLES

LIST OF FIGURES

SUMMARY

This thesis describes the development of III–nitride materials for ultraviolet (UV) vertical cavity surface emitting lasers or VCSELs. The goal of this research is to develop UV VCSELs targeting a peak emission wavelength of $\lambda = 369.5$ nm for chip–scale Yb atomic clock application. Epitaxial structures for these devices are grown by metalorganic chemical vapor deposition (MOCVD) and several material analysis techniques were employed to characterize these structures such as atomic force microscopy, electroluminescence, Hall–effect measurement, photoluminescence, transmission electron microscopy, and X–ray diffraction. Each of these will be discussed in detail.

A traditional electrical injection VCSEL consists of several key structure components including, top and bottom distributed Bragg reflectors (DBRs) for forming the vertical cavity, spacer layers for optical mode alignment as well as carrier transport, and multi–quantum wells (MQWs) for photon generation. With the growth and fabrication technologies developed to date, this study focuses on solving p–spacer vertical hole transport issue and growth for high quality n–side DBR. By integrating these developed technology, VCSEL under optical pumping as well as electrically inject micro–cavity light–emitting diodes (MCLEDs) will be presented.

To achieve the final goal of the study, the first section focuses on the development of proper p–spacer layer for vertical hole injection. Magnesium (Mg), the commonly used p–type dopant in III–N material system, has large activation energy which limits the p–type conductivity of the material. The situation worsens approaching wider–bandgap material because of an increase in the activation energy of the Mg dopants at the same time. To solve the problem of hole transport for vertical injection, a

high–aluminum mole fraction AlGaN ([Al] $\sim$ 0.6) diode featuring an inverse–tapered p–waveguide design was demonstrated.

Next, the development for n–side DBR will be presented. In this work, three different DBR approaches will be demonstrated. First, a 40–pair electrically conducting n–DBR consisting of silicon–doped $Al_{0.12}Ga_{0.88}N$/GaN bilayers will be presented. To further improve the electrical characteristics for vertical electron transport, a compositionally graded $Al_xGa_{1-x}N$ silicon doped n–DBR with x vary from 0 to 0.12 will be demonstrated. Differences in electrical and optical characteristics of these two n–DBRs will be studied. Lastly, to increase the index contrast between the bilayers (aluminum mole fraction of (Al)GaN material), a novel strain management approach utilizing GaN interlayer enables the possibility to increase the aluminum mole fraction without cracking. A detailed material characterization for understanding the effect of DBR will be presented.

With the technology developed for the p–spacer and the n–side DBR, an optically pumped VCSEL under KrF excimer laser excitation was demonstrated. The p–side DBR utilized HfO_2/SiO_2 dielectric stacks formed by e–beam evaporation. Laser action at 300 K was observed at $\lambda = 374.5$ nm with threshold pumping power density of $P_{th} = 1.62$ MW/cm^2. On the other hand, the electrical injected MCLEDs utilized indium–tin–oxide (ITO) for lateral current spreading on the p–side and N^+–implant to create a current aperture. At room temperature, the peak emission was observed at $\lambda = 371.4$ nm while the spectral linewidth narrowed down to 5.1 nm at the highest measured current injection level. Further studies were carried out to understand the temperature–dependent characteristics of the MCLED.

CHAPTER I

INTRODUCTION

The term Light Amplification by Stimulated Emission of Radiation or "LASER" was first introduced by Gordon Gould at Columbia University in 1959 [1]. The first functional laser (ruby laser with $\lambda = 692$ nm) demonstration was not until 1960 by Maiman at Hughes Research Laboratory [2]. This invention was then soon applied to semiconductor materials and formed laser diodes (LDs) in 1962 [3–6]. Notably, Nick Holonyak, Jr. of General Electric was the first and only group in 1962 demonstrating "visible" red LD using $GaAs_{1-x}P_x$ ternary alloys [5]. As the III–V material technology advanced, Shuji Nakamura demonstrated the first blue LD in 1996 with the GaN based material system [7]. The breakthrough of Group III–nitride material technology enables more possibilities in fabricating optical emitters outputting wavelength from 200 nm to 1772 nm by alloying InN, GaN, and AlN as shown in Fig.1 [8].

Surface emitting lasers have several key advantages over edge emitting lasers including, wafer scale testing, narrow beam divergence, low current operation, easy polarization control, and stable single–mode operation. Since the first demonstration of vertical cavity surface emitting lasers or VCSELs by Soda, et al. [9], various applications are utilizing VCSELs for optical sources such as, optical–fiber data transmission, optically pumped solid–state lasers, and chip–scale atomic clocks. Laser operation of III–N based VCSELs under electrical–injection has been reported by several research teams; however, most of the reported electrically pumped VCSELs have peak emission wavelength in the visible blue–green spectral range [10–15]. The development for UV VCSELs has been impeded due to limitations of electrical conductivity for high

aluminum content $Al_xGa_{1-x}N$, lack of high reflectivity III–N ultraviolet (UV) distributed Bragg reflectors (DBRs), and relatively high sub–bandgap absorption from p–type materials. This thesis will present the development of UV VCSELs targeting a peak emission wavelength of $\lambda = 369.5$ nm for chip–scale Yb atomic clock application.

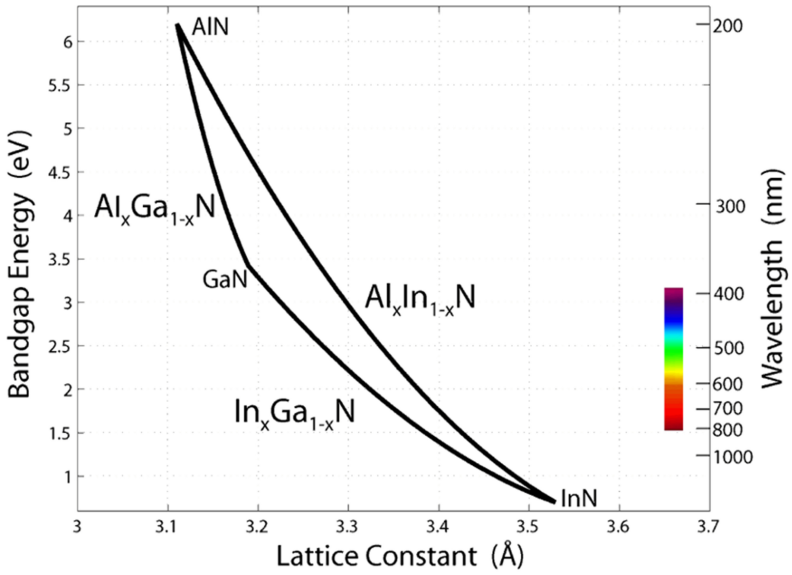

Figure 1: Bandgap energy vs. lattice constant for III–nitride materials [7].

1.1 III–Nitride Material System

In III–nitride family, i.e., AlN, GaN, InN, and their single crystal alloys exist in three different structures: wurtzite, zinc–blende, and rocksalt [16]. The bulk form of these binary compounds are thermodynamically stable in the wurtzite structure, which is optically anisotropic due to the difference in lattice parameters in different directions. In addition to optically anisotropic, the wurtzite structure also has anisotropic internal electric fields due to the piezoelectric and polarizations.

Figure 2 [17] shows the unit cells for both wurtzite and and zinc–blende cubic

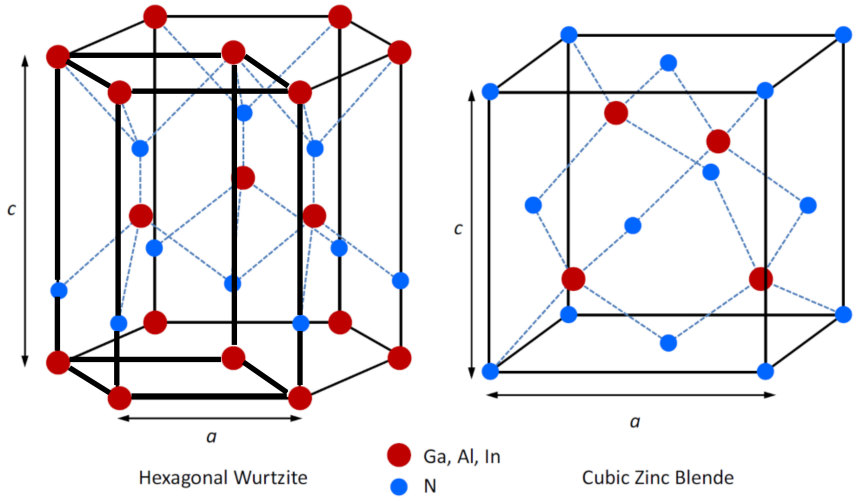

Figure 2: Unit cell of a hexagonal wurtzite structure (left) and a zinc–blende structure (right) [16].

structures. In the case of hexagonal/wurtzite crystal structures, they have 120° rotational symmetry; specifically, the hexagonal structure has six–fold symmetry along the c–axis. As a result, the four–axes Miller–Bravais indices in form of *(hkil)* are introduced for this crystal structure. Indices *(hki)* correspond to the three–axes on the basal plane which are 120° apart in the vector direction and *(l)* corresponds to the c axis. Since the *(hki)* are 120° apart from each other, the relationship between the indices can be express as linear superposition: $i = -(h+k)$. On the other hand, the crystal directions in zinc–blende structure are given by [xyz] are numerically equivalent to the Miller indices of the perpendicular planes.

In an ideal wurtzite structure, the ratio for c/a is 8/3; however, the ratios for AlN, GaN, and InN are 1.601, 1.627, and 1.612, respectively. The deviations from the ideal structure originate from the electronegativity difference between the Group III and Group V atoms when they bond to one another. A dipole is generated based on the differences in electronegativity, and results in a polarization charge which significantly alters the device performance in both optical and electrical properties.

All the wurtzite III–nitride binary compounds are direct–bandgap materials. The

bandgap energy for each III-nitride binary compound is 0.78 eV, 3.4 eV, and 6.23 eV at room temperature for InN, GaN, and AlN, respectively. In order to produce deep–UV optical emitters, AlN, InN, and GaN can be alloyed to form AlGaN or InAlN ternary alloys. The bandgap energy (E_g) and the lattice constant (a_0) of the nitride ternary alloys can be formulated by Vegard's Law as:

$$E_g(A_xB_{1-x}N) = xE_g(AN) + (1-x)E_g(BN) - x(1-x)b \tag{1}$$

$$a_0(A_xB_{1-x}N) = xa_0(AN) + (1-x)a_0(BN) \tag{2}$$

where x is an alloy composition ($0 \leq x \leq 1$), b is known as the bowing parameter, and A and B corresponds to group III element. The widely accepted bowing parameters for AlGaN, InGaN, InAlN are 0.7 eV, 1.4 eV, and 3.0 eV, respectively [18–22].

In this study, all the wafers are grown on either AlN native substrates, or AlN buffer on sapphire substrates, or GaN bulk substrates, or GaN buffer on sapphire substrates; thus, the biaxial strain effect in the material becomes important as it changes the device band structure and induces a piezoelectric polarization field [23–25]. The in–plane strain elements can be described as:

$$\epsilon = \epsilon_{xx} = \epsilon_{yy} = \frac{a_0 - a(x)}{a_0} \tag{3}$$

where a_0 is the lattice constant of substrate and $a(x)$ is the lattice constant for each epitaxial layer. The strain in the perpendicular direction can be written as:

$$\epsilon_\perp = \epsilon_{zz} = -\frac{1}{\nu}\frac{C_{13}}{C_{33}}\epsilon_{xx} \tag{4}$$

where ν is Poisson's ratio and C_{ij}'s are the elastic stiffness constants, which can be obtained based on Vegard's law for ternary alloys. The strain–induced shifts in the conduction band can be modeled as

$$\delta E_c = a_{cz}\epsilon_{zz} + a_{ct}(\epsilon_{xx} + \epsilon_{yy}) \tag{5}$$

Table 1: Physical parameters of III–nitride semiconductors [25, 26].

	GaN	AlN	InN
Lattice Constant, a (Å)	3.189	3.112	3.545
Lattice Constant, c (Å)	5.185	4.982	5.76
Bandgap (eV)	3.39	6.23	0.78
Index of Refraction at 3 eV	2.9	2.15	3.05
Thermal Conductivity, κ (W/cm–K)	1.3	2.0	0.8
Relative Permittivity, ϵ_r	9.5	8.5	15
a_1 (eV)	-4.9	-3.4	-3.5
a_2 (eV)	-11.3	-11.8	-3.5
D_1 (eV)	-3.7	-17.1	-3.7
D_2 (eV)	4.5	7.9	4.5
D_3 (eV)	8.2	8.8	8.2
D_4 (eV)	-4.1	-3.9	-4.1
C_{11} (GPa)	390	396	223
C_{12} (GPa)	145	137	115
C_{13} (GPa)	106	108	92
C_{33} (GPa)	398	373	224
C_{44} (GPa)	105	116	48

where a_{cz} and a_{ct} are the hydrostatic deformation potentials for conduction band in perpendicular and tangential direction, respectively. On the other hand, the shift in valence band is described as

$$\delta E_v = (D_1 + D_3)\epsilon_{zz} + (D_2 + D_4)(\epsilon_{xx} + \epsilon_{yy}) \tag{6}$$

D_1 and D_2 are the hydrostatic deformation potential in valence band while D_3 and D_4 play the role of shear deformation potential in valence band. The relationships between

$$a_1 = a_{cz} - D_1 \qquad a_2 = a_{ct} - D_2 \tag{7}$$

are due to the anisotropic hexagonal structure. Table 1 [26, 27] summarizes various physical parameters of the III–nitride binary materials.

1.2 Metalorganic Chemical Vapor Deposition

Metalorganic Chemical Vapor Deposition (MOCVD) was first introduced by Manasevit [28] at North American Rockwell in 1968. This material growth technology is also known as organometallic chemical vapor deposition (OMCVD), metalorganic vapor phase epitaxy (MOVPE), and organometallic vapor phase epitaxy (OMVPE). The development of this technology was stimulated by the limitations of the state–of–the–art (at the time) liquid phase epitaxy (LPE) growth technology in 1970's. Since the era of LPE, molecular beam epitaxy (MBE), which is introduced by Cho [29], and MOCVD have dominated the research, development, and manufacture of compound semiconductor devices.

In the early development of MOCVD, Manasevit demonstrated the growth of various materials, including GaAs, GaP, AlGaAs, AlN, and GaN [30]. Later, Dupuis, et al. demonstrated some practical devices grown by MOCVD such as, AlGaAs/GaAs solar cells and laser diodes in 1977 [31] and continuous room–temperature operation laser diodes in 1978 [32]. MOCVD is the epitaxial crystal growth technology of choice

for an impressive array of commercial devices for instance, lasers, light emitting diodes (LEDs), avalanche photodiodes (APDs), heterojunction bipolar transistors (HBTs), high electron mobility transistors (HEMTs), and solar cells. Virtually every III–V compound semiconductor material system has been grown successfully by MOCVD. Thousands of MOCVD reactors have been sold worldwide, and reactors capable of growing on 69–2 inch wafers or 19–4 inch wafers *in a SINGLE growth run* are commercially available.

An MOCVD process for depositing compound semiconductors is governed by the chemical equation:

$$R_nA + DH_n \rightarrow AD + nRH \tag{8}$$

where R is an organic radical, such as a methyl– or ethyl–radical, and A and D are constituent species for the deposited solid. An example for III–nitride material is give by

$$(CH_3)_3Ga + NH_3 \rightarrow GaN + 3CH_4 \tag{9}$$

A large number of metalorganic (MO) precursors used in MOCVD growth have been studied and Table.2 shows the commonly used MO sources for III–nitride material growth. During the growth, a molar flow rate of a MO source depends on the flow rate of the carrier gas, the pressure of the bubbler (MO source container), and the equilibrium vapor pressure of the precursor that is a function of temperature. Under thermal equilibrium, the vapor pressure of a MO source can be described with constant A and B in table2 as

$$\log p \text{ (mmHg)} = B - A/T \tag{10}$$

In the case of most commonly used p–type dopant, bis(cyclopentadienyl)magnesium (Cp_2Mg), the vapor pressure equation is revised as

$$\log p \text{ (mmHg)} = B - A/T + 2.18\log T \tag{11}$$

Table 2: Commonly used metalorganic sources in III–nitride material growth.

Metalorganic Compound	Chemical Formula	Molar Mass	Vapor Pressure Constants	
			A	B
Trimethylgallium (TMGa)	$(CH_3)_3Ga$	114.83	1703	8.07
Trimethylaluminum (TMAl)	$(CH_3)_3Al$	72.09	2134.83	8.224
Trimethylindium (TMIn)	$(CH_3)_3In$	159.93	3014	10.52
Bis(cyclopentadienyl) magnesium (Cp_2Mg)	$(C_5H_5)_2Mg$	154.49	4198	25.14

The vapor pressure of these MO sources are highly sensitive to temperature as described by Eq. 10 and 11; thus, the bubblers are usually stored in an isothermal water bath to maintain a constant temperature. Metalorganic precursors are transported to the growth chamber with inert carrier gases, e.g., H_2 or N_2, and the choice of carrier gas depends on the material of interest. Lastly, maintaining the constant total pressure within the bubbler is also critical for maintaining constant bubbling efficiency as the molar flow rate of a MO source can be formulated as

$$Q = \frac{p_{mo}(T)}{p - p_{mo}(T)} \frac{F_{cg}}{C_{STP}} \tag{12}$$

where p is the bubbler pressure, $p_{mo}(T)$ is the equilibrium vapor pressure of the metalorganic source at a given temperature, F_{cg} represnts the flow rate of the carrier gas in standard cubic centimeter per minute (sccm), and C_{STP} is 22,406 cc/mole, which is the molar volume of an ideal gas at room temperature and atmosphere pressure. Besides metalorganic precursors, hydrides are also commonly used as n-type dopants and group V precursors. In III-nitride material growth, silane (SiH_4)

and ammonia (NH_3) are the most commonly used precursors for the n-type dopant and the group V precursor, respectively.

An MOCVD reactor consist of three major components: gas delivery system, growth chamber, and safety infrastructure. Figure 3 [33] shows a simplified schematic diagram for a vertical gas injection MOCVD system. The vertical close–coupled showerhead (CCS) gas injection system enables the intermixing of precursors within close proximity to the substrates, resulting in uniform deposition. In addition, a three–zone heater design allows customized temperature profile across a wafer to further control uniformity of epitaxial layers. In this thesis, a Thomas Swan (now AIXTRON) 6 × 2" rotating disk CCS reactor is used. A Laytec in–situ optical monitoring system, with EpiTT and EpiCurve systems, provides real–time data collection for substrate temperature, wafer curvature, and reflectivity probing at wavelengths of 633 nm and 950 nm. These parameters allow us to extract the growth rate of the film and to monitor the growth chamber conditions.

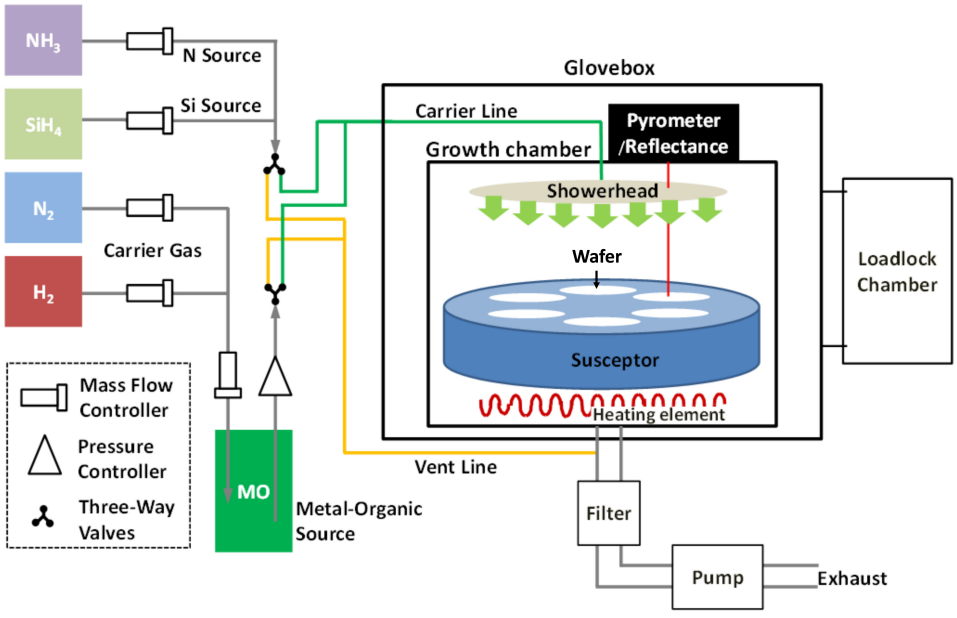

Figure 3: A simplified schematic diagram of an MOCVD reactor. [32]

CHAPTER II

MATERIAL CHARACTERIZATION

Once the epitaxial semiconductor layers are grown, it is very important to study the material quality, electrical, and optical characteristics then correlate the results to growth conditions for optimization. In this chapter, the basic methodologies used to characterize the epitaxial material is presented, including atomic–force microscopy (AFM), electroluminescence (EL), Hall–effect measurement, photoluminescence (PL), secondary ion mass spectrometry (SIMS), transmission electron microscopy (TEM), transmission–line measurement (TLM), and X–ray diffraction (XRD).

2.1 Atomic Force Microscopy

AFM or scanning force microscopy (SFM) provides three-dimensional mapping for a specimen surface with sub–nanometer resolution scale. The precursor of the AFM, scanning tunneling microscope, was invented in 1981 by Gerd Binnig and Heinrich Rohrer [34] who earned Nobel Prize in Physics in 1986. Later, Binnig, Quate, and Gerber invented the first AFM in 1986 [35], which consisted of five major components: a cantilever, probe tip, sample stage, measurement device, and feedback mechanism as shown in Fig.4 [36].

The most important component of the microscope system is the cantilever with the probe tip at its end, which is used to scan a specimen surface. The cantilever is typically made of silicon or silicon nitride (Si_3N_4) and some of cantilevers have aluminum or gold as reflective coating, which is used to enhance the reflectivity of the back side of cantilevers as well as the signal deflected to detector. Because AFM relies on the forces between the probe tip and the specimen, knowing these forces, including mechanical contact force, van der Waals force, capillary force, chemical

bonding force, electrostatic force, magnetic force, Casimir force, and solvation force, is important for proper imaging. Thus, the cantilever is designed to detect forces in the range of 10^{-8} to 10^{-12}N while the deflections are limited to as small as $10^{-4}\mathring{A}$. The probe tip is usually in pyramid shape with 3 to 6 μm height and 15 to 40 nm end radius. Ideally, the probe tip should only have "ONE" atom at its apex for maximum resolution.

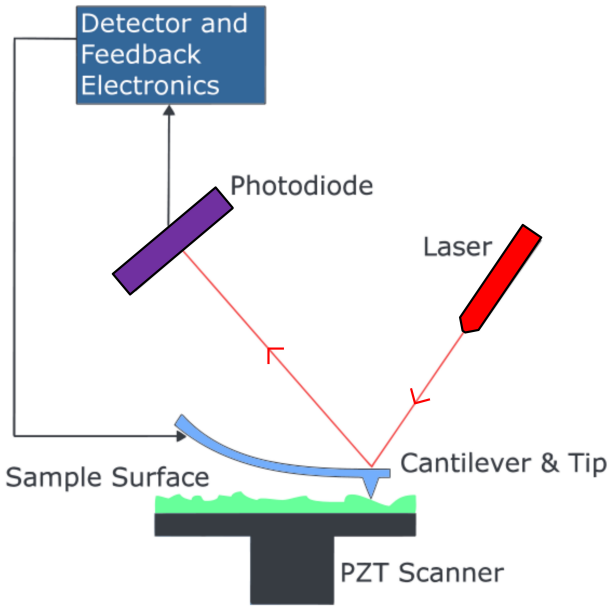

Figure 4: Schematic diagram of an AFM system using laser beam deflection detection. [35]

In this research, a Veeco Dimension 3100 scanning probe microscope is used. It supports two main operation modes, i.e., contact mode and tapping mode. Figure 5 [37] summarizes the distance and the interatomic force, also known as Lennard–Jones potential curve, for the main operation modes. Contact mode is the first and foremost mode of operation and it is also the most common mode of operation. During the operation, the tip is kept in physical contact with the specimen surface and a piezoelectric crystal is used to control the distance between the sample and the tip for maintaining constant contact. Due to the fact that the tip is in hard contact

with the specimen surface, the stiffness of the cantilever needs to be less than the effective spring constant holding the surface atoms together, which is typically on the order of 1 – 10 N/m; thus, most contact–mode cantilevers have a spring constant $<$ 1 N/m. Images are formed by mapping the cantilever deflection with respect to the position of the sample to its topography.

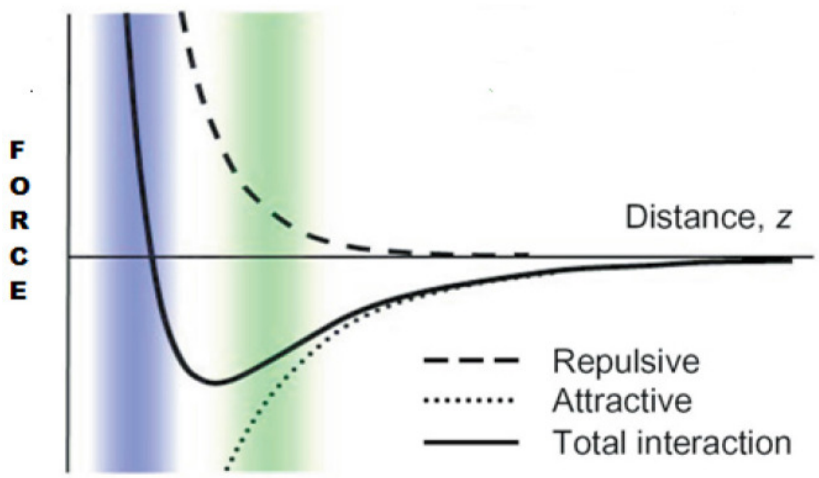

Figure 5: A tip–to–sample distance versus an interatomic force. For a tip–to–sample distance in blue region, microscope is operating under contact mode while in green region refers to non–contact mode. For intermittent–contact operation (tapping mode), tip–to–sample distance lies between contact mode and non–contact mode (white region between blue and green). [36]

In the tapping mode operation, the cantilever is oscillating at its resonant frequency (typically from 100 to 500 kHz) which results in the probe tip "tapping" the surface with constant frequency. The feedback system will maintain the oscillation amplitude constant (typically 100 to 200 nm). Because the probe tip is not constantly physically in contact with sample, this technique allows high resolution topographic imaging of sample surfaces that are easily damaged. In addition, the high frequency makes the surface stiff (viscoelastic), and the tip-sample adhesion forces is greatly reduced; thus, tapping–mode inherently prevents the tip from sticking to the surface

and causing damage during scanning. As a result, all the AFM images present in this thesis are captured under tapping–mode operation.

2.2 Electroluminescence

Electroluminescence (EL) is a widely used characterization methodology to analyze the electrical and optical properties of p–n junction devices. EL injects current into material through the electrical contacts, which are deposited on the contact layers by a CHA Solution electron beam (E–beam) evaporator and then thermally annealed by AnnealSys AS–One rapid thermal annealing (RTA) system. The carriers that are injected through the contacts will travel within the material and radiatively recombine to generate photons with an energy approximately equal to the material bandgap.

In this thesis, a Keithley 2400 DC power supply and an AVTECH pulsed current source are used as the sources for CW and pulsing measurement, respectively. Optical emission from the device is first coupled into a 600 μm diameter multimode optical fiber then passes through a SPEX 500M monochromator with a spectral resolution of 0.02 nm. The optical intensity at each wavelength is then analyzed by Hamamatsu R928 photomultiplier tube (PMT) and an Ortec 776 counter. For the optical polarization measurement, an α–BBO Glen–Laser polarizer with 100,000 : 1 extinction ratio is used to determined the optical polarization (transverse electric or transverse magnetic mode). To characterize devices under various temperature ambient, Lakeshore TTPX cryogenic probe station is used instead.

2.3 Hall–Effect Measurement

Hall–effect measurement is a method to measure the resistivity, majority carrier type, majority carrier concentration, and low–field carrier mobility of a given semiconductor. The most commonly used resistivity measurement technique is known as the van der Pauw method, which was first introduced by Leo J. van der Pauw in 1958 [38, 39]. Figure 6 [40] shows the examples of possible sample configurations of van

der Pauw method. In this thesis, an approximately 1×1 cm^2 square sample is prepared. In the case of n–type III–N material, vanadium–based (V/Al/Ti/Au for $300\mathring{A}/500\mathring{A}/300\mathring{A}/500\mathring{A}$) or titanium–based (Ti/Al/Ti/Au for $300\mathring{A}/500\mathring{A}/300\mathring{A}/500\mathring{A}$) metal alloy is deposited and then a two–step thermal annealling in a N_2 ambient is performed. The choice of the metal alloy as well as the thermal annealling processes depend on the bandgap energy of the n–type III–N material.

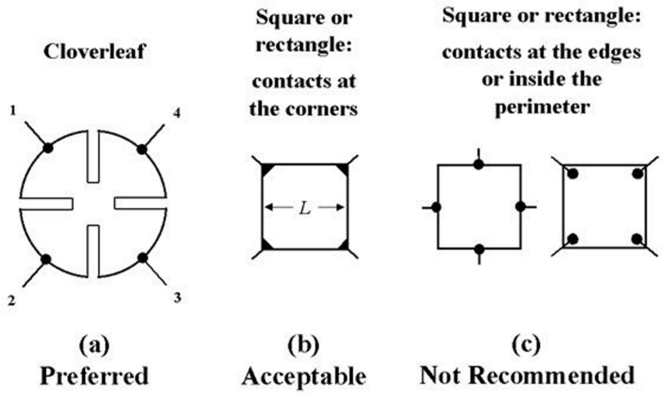

Figure 6: Examples of possible van der Pauw configurations and their preference. [39]

For the p–type III–N material, an extra step is required to prepare the Hall samples. Magnesium is the most commonly used acceptor in III–nitride material; however, it is compensated by hydrogen within the film during epitaxial growth [41]. In order to activate the acceptors, the hydrogen bond must be broken by methods such as low energy electron beam irradiation (LEEBI) [42] or thermal annealing [43]. In this work, wafers are first annealed in air for 3 minutes at 900°C before metal evaporation. The metal stack for p–type material uses nickel–based material (Ni/Ag/Pt for $50\mathring{A}/500\mathring{A}/200\mathring{A}$) and the annealing is done in compressed air.

The experimental arrangement for resistivity measurements using van der Pauw's method is shown in Fig.7. The current is first applied across contact 1 and 2 (I_{12}) and

the voltage is measured across contact 4 and 3 (V_{43}). Next, the current is applied I_{14} and voltage V_{23} is measured. The sheet resistivity (ρ_s) or bulk resistivity (ρ) can be calculated as

$$\rho_s = \rho/t = \frac{\pi}{2ln(2)}\left[\frac{V_{43}}{I_{12}} + \frac{V_{23}}{I_{14}}\right] F(Q) \quad (\Omega/\square) \tag{13}$$

where t is the thickness of the layer, Q and F coefficients corresponds to symmetry and correction factors, respectively.

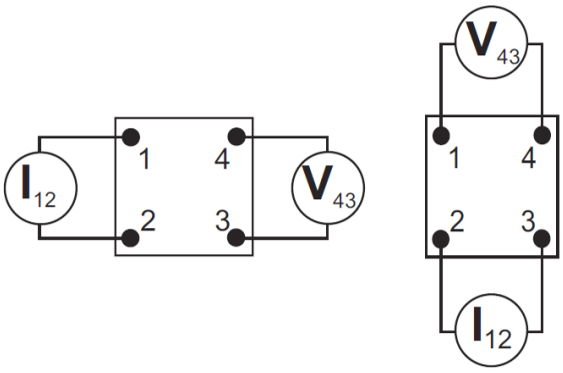

Figure 7: Schematic diagram of resistivity measurement using van der Pauw's method. [39]

The correction factor (F) is used to described the geometrical asymmetry and not for material anisotropy or inhomogeneity. The symmetry factor Q is defined as (in the case shown in Fig.7)

$$Q = \frac{V_{43}I_{14}}{I_{12}V_{23}} \tag{14}$$

or its reciprocal, whichever is greater than 1. Assuming the asymmetry coefficient is not too large (Q < 10), F can be approximated as

$$F = 1 - 0.34657A - 0.09236A^2 \tag{15}$$

where A is

$$A = \left[\frac{Q-1}{Q+1}\right]^2 \tag{16}$$

When the current is fixed to a constant value for all six possible permutations, averaging the voltages V_{xy} measured for both current directions can be used to cancel thermoelectric and other effects; thus, Eq.13 and 14 can be reduced to

$$\rho_s = \frac{\pi}{2ln(2)} \left[\frac{(V_{43} + V_{23})}{I} \right] F(Q) \quad (\Omega/\square) \tag{17}$$

$$Q = \frac{V_{43}}{V_{23}} \tag{18}$$

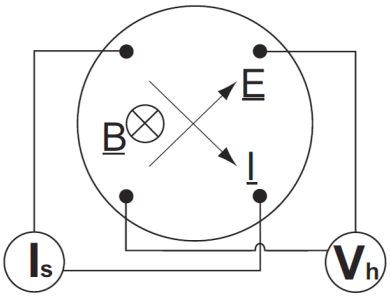

Figure 8: Generalized Hall effect measurement setup. [39]

The experimental setup for Hall effect measurement is shown in Fig.8. A constant current is injected at two non–adjacent contacts and the Hall voltage (V_h) is measured across the remaining contacts while a constant magnetic field B is applied perpendicular to the sample surface. The relation between magnetic and electrostatic forces can be related through the Lorentz Force equation given by

$$\overrightarrow{F} = q(\overrightarrow{E} + \overrightarrow{v} \times \overrightarrow{B}) \tag{19}$$

where q is the elementary charge, $\overrightarrow{E}$ is the electric field, $\overrightarrow{v}$ is particle velocity, and $\overrightarrow{B}$ is magnetic field. By setting the net force equal to zero, the electric field can be related to the magnetic field and the carrier velocity. The current can be calculated based on

$$\overrightarrow{I} = qNtW\overrightarrow{v} \tag{20}$$

where N is the carrier density, t is the thickness of the layer, and W is the separation between two contacts. Thus, the Hall coefficient (R_H) can be obtained by

$$R_{Hs} = R_H/t = \frac{1}{qN} = \frac{V_h}{IB} \quad (m^3/C) \tag{21}$$

Once the Hall coefficient is obtained, the sheet carrier density (N_s) is related to Hall coefficient as

$$N_s = \frac{1}{qR_{Hs}} \tag{22}$$

Finally, the carrier mobility is calculated using

$$\mu = \frac{R_{Hs}}{\rho_s} \tag{23}$$

The Hall measurements carried out in this study were performed at 300 K using an Accent HL5500PC Hall measurement system.

2.4 Photoluminescence

Photoluminescence (PL) is an optical characterization technique for estimating bandgap energy and defect levels in a semiconductor. In order to have radiative transitions, the optical excitation energy added to the semiconductor needs to be larger than the bandgap to promote an electron from valence band to conduction band, creating an electron–hole pair. For direct–bandgap semiconductors, most of the electron–hole pairs will recombine near the band edge, which will create photons with nearly the same energy as the bandgap. The corresponding wavelength for a given photon energy (E) has a relation

$$E = h\nu = \frac{hc}{\lambda} \tag{24}$$

where h is Planck constant, ν is frequency of light, c is speed of light, and λ is the wavelength of light.

A Coherent COMPexPro 110 excimer laser is used as an excitation source in this study. The active gas used in this laser is krypton fluoride (KrF), which emits at a

wavelength of 248 nm ($h\nu \sim 5$ eV) under following reaction

$$2KrF \rightarrow 2Kr + F_2 + h\nu \tag{25}$$

The dimensions of the incident laser beam is 24 (mm) $\times$ 10 (mm) with a pulse duration of 20 ns. The laser output power can range from 20 mJ to 200 mJ while the repetition rate can be set from 1 Hz to 100 Hz. The optical emission from the semiconductor sample is collected into a 600 μm diameter multimode optical fiber then analyzed with an Ocean Optics Maya 2000 Pro UV spectrometer with spectral range from 200 nm to 400 nm and $\sim$ 0.1 nm resolution. For the optical polarization characterization, an α–BBO Glen–Laser polarizer with 100,000 : 1 extinction ratio is used.

2.5 Secondary Ion Mass Spectrometry

Secondary Ion Mass Spectrometry (SIMS) profiling is a method used to measure the specific atomic concentration in a sample as function of depth. The background impurity concentrations, materials compositions, layer thickness, and doping concentrations in the epitaxial layers can be measured simultaneously; however, this is a destructive process.

Typically, a SIMS system consists of a primary ion gun, primary ion column, high vacuum chamber and secondary ion extraction lens, mass analyzer, and ion detection unit. The primary ion gun generate a primary ion beam composed of species such as O_2^+ or Cs^+ to sputter the sample layer by layer. Oxygen primary ions are often used to investigate electropositive elements due to an increase of the generation probability of positive secondary ions, while cesium ions are commonly used to detect electronegative elements. All the atoms and molecules released from the sample surface are known as secondary ions.

For a given SIMS system, there are three basic analyzers available: sector, quadrupole, and time-of-flight (TOF). In this thesis TOF mass spectrometry is used, all ions are

accelerated by an electric field with known strength and the acceleration results in an ion having the same kinetic energy as any other ion that has same charge. The time that it subsequently takes for the particle to reach a detector at a known distance is measured and this time is related to the mass–to–charge ratio of the particle (heavier particles have lower speeds), which allow us to identify ions.

As the sample is sputtered, the ion counts are plotted as a function of time for the ions of interests. At the end of sputtering, the depth of sputtering is calibrated by profilometer to convert from time profile to depth profile. In addition, the concentration of each ions are converted to elemental concentration (ions/cc) under following equation:

$$C_E = RSF\frac{I_E C_M}{I_M} \tag{26}$$

where C_E is the concentration of the element of interest, RSF is the abbreviation of relative sensitivity factor, I_E is the secondary ion intensity, C_M is the major/matrix element concentration, and I_M is the ion intensity of major element. IONTOF Time–of–Flight SIMS is used to collect some of data for relative comparison in this work while the calibrated measurements were made by EAG Laboratories.

2.6 Sheet Resistance Mapping

Although Hall–effect measurements can provide detailed electrical characteristics of the film, the measurement requires the samples to be cut from the wafer and metalization to be applied which are destructive processes. To preserve the maximum wafer area for the device fabrication process, a nondestructive characterization technique is desired. A way around this issue is to use a contactless measurement system manufactured by Lehighton Electronics Inc. LEI–1510C®, which utilizes an eddy–current probing method to obtain the sheet conductance or sheet resistance. With the known material thickness, the bulk resistivity can be calculated as $\rho(\Omega - cm) = R_s(\Omega/sq.) \times t(cm)$. The measurement configuration used in this thesis

consists of 55 test points across the entire 2" wafer as shown in Fig. 9. The eddy current probe consists of a magnetic coil which is driven by alternating current (AC) to generate time–varying magnetic field. A time varying magnetic field will induce loops of electrical current in an electrically conducting epitaxial layer and the magnitude of the current in a given loop is proportional to the strength of the magnetic field, the area of the loop, and the rate of change of flux, and inversely proportional to the resistivity of the material. Since any single conducting layer within the epitaxial structure will response to the time–varying magnetic field, the layer of interest must have a greater conductance than the remaining structure, which includes the substrate. As a result, this characterization technique can be more effective with n–type material in III–N material system assuming the substrate is insulating.

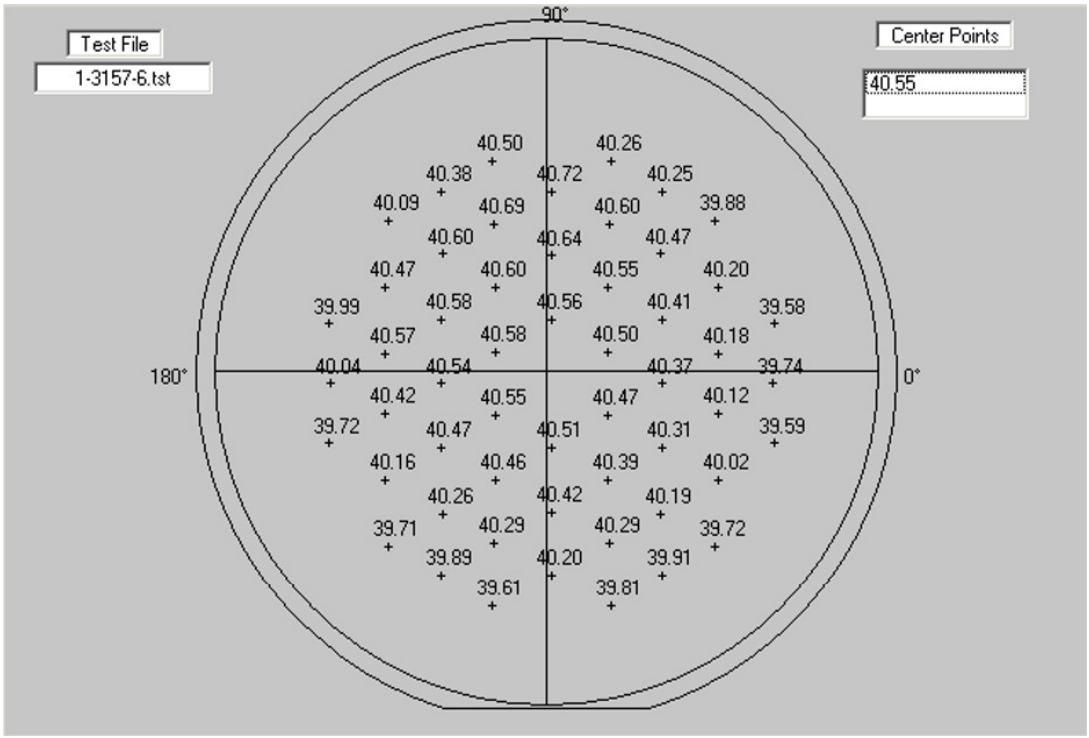

Figure 9: Layout of 55 test point for sheet resistance mapping used in this work.

2.7 Transmission Electron Microscopy

The resolution of an optical system is limited by the Rayleigh criterion:

$$\delta = \frac{0.61\lambda}{n \sin\theta} \tag{27}$$

where λ denotes the wavelength of the optical system, n is index of refraction of the optical lens, and θ refers to the half-angle of the maximum cone of light that can enter or exit the lens. The Rayleigh criterion limits the optimal resolution for an optical ultraviolet microscope to be $\sim$ 200 nm. In order to achieve atomic resolution, an even shorter–wavelength microscopy system is required. Utilizing de Broglie's equation for the wavelength of electrons, Max Knoll and Ernst Ruska in 1931 built the first transmission electron microscope (TEM) [44]. The electron wavelength is related to the electron's kinetic energy by the following relationship

$$\lambda = \frac{h}{\sqrt{2m_e q U_0 (1 + \frac{qU_0}{2m_e c^2})}} \tag{28}$$

where h is Plank's constant, m_e is the electron mass, q is the unit charge, U_0 is the accelerated voltage, and c is the speed of light. Equation 28 suggests that sub–angstrom electron wavelengths can be easily achieved under sufficient bias; therefore, a sub–angstrom resolution microscopy system can be realized.

To achieve high resolution, a TEM system utilizes an electron beam for imaging; therefore, it is crucial to understand the interaction between the electrons and the sample. Figure 10 shows a schematic diagram of the generated signals from a thin specimen under a high–energy beam illumination. The backscattered electrons (BSE) and secondary electrons (SE) can be detected with a scanning electron microscope (SEM). Energy–dispersive X–ray spectroscopy (EDS, EDX, or XEDS) detects the characteristic X–rays for elemental analysis or chemical characterization. The transmitted direct beam is the most important signal for TEM imaging since it carries atomic level information of the sample. Inelastically scattered electrons are

important for another type of TEM imaging known as scanning transmission electron microscope (STEM). STEM measurements allow some important materials analysis techniques, including energy dispersive X–ray (EDX) spectroscopy, electron energy loss spectroscopy (EELS), and annular dark-field imaging (ADF).

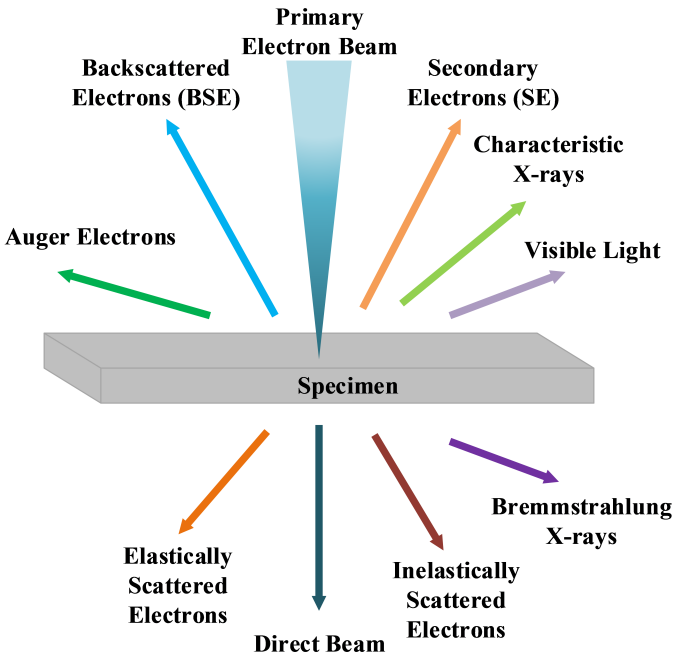

Figure 10: Signals generated when a high–energy electron beam interacts with a thin specimen. Most of these signals can be detected in different types of electron microscopy systems.

In the TEM system, the primary electrons can be generated by two different methods, thermal emission and field emission. Typically, thermal emission sources have shorter lifetime and operate at higher temperature; however, the quality of the vacuum environment is not as critical as for field–emission sources. Since electrons are used as the electromagnetic source for a TEM system, the optical lens in the conventional microscope needs to be replaced by an electrons lens. However, the refraction of the electron beam passing through different mediums is still governed by the Snell's law. Figure 11 [45] shows the schematic outline of a TEM system.

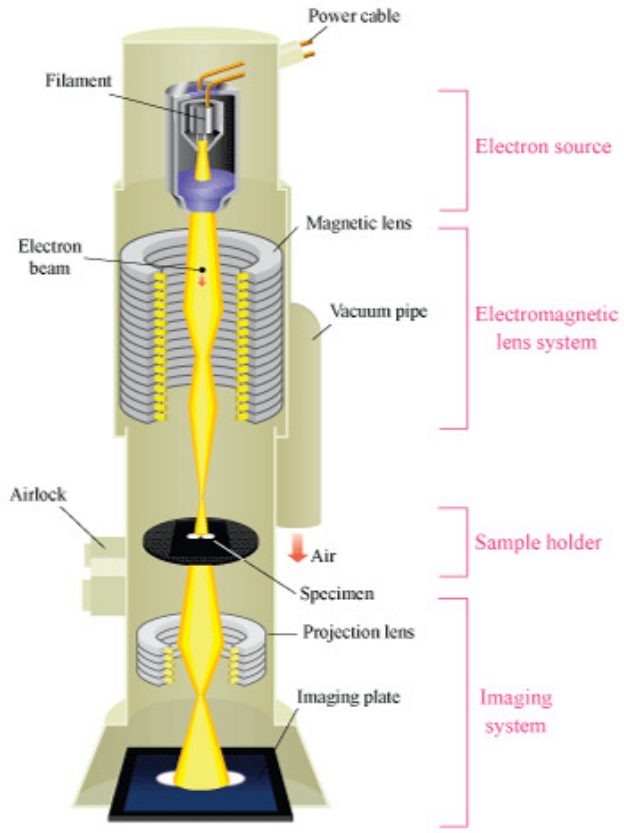

Figure 11: The schematic diagram of a TEM. [44]

A typical TEM system has three main apertures, the condenser aperture (CA), the objective aperture (OA), and the select–area (SA) aperture. The SA aperture is used to acquire select–area diffraction patters (SADP), which is extremely important to determine the zone axis and crystal structure. The OA is located at the back focal plane of objective lens and it is used to determine the imaging modes of microscope, bright–field, dark–field or diffraction mode. Lastly, CA is employed to control the brightness of the image. The operating mode that offers the best resolution images in a given microscope is known as high–resolution transmission electron microscopy (HRTEM), which measures the phase contrast from the transmitted beam of "thin" specimen. On the other hand, STEM rasters the beam across the sample and a very powerful characterization technique that uses a STEM system is high-angle annular

dark-field imaging (HAADF). The image from HAADF is directly related to the atomic number (Z); therefore, relative composition between layers from same type of alloy can be easily determined.

The TEM images and analysis presented in this work was performed by our colleagues at Arizona State University under Professor Fernando A. Ponce.

2.8 Transmission–Line Measurement

The transmission–line measurement (TLM) is developed for measuring the sheet resistance of the semiconductor (R_{sh}) and the the specific metal–semiconductor contact resistance (ρ_c). The metal patterns are created via an ultraviolet photolithography process. First, two layers of photoresist, LOR 5B and S1813 resist, are coated on the wafer using a CEE 100 spin coater. The TLM patterns are structured using a Karl Süss MJB–3 mask aligner for UV–lamp exposure. In order to remove the unwanted photoresist, the wafer needs to go through development and descum processes to insure the patterns are sharp. Standard metal evaporation and rapid thermal annealing (RTA) are performed as described in section 2.3 Hall measurement; however, an extra step is performed before metal annealing, which is called lift–off. Lift–off process is to remove all the photoresist and the areas of unwanted metal stacks. The following discussion separates TLM patterns into two categories based on the shape of metal contacts.

2.8.1 Rectangular Transmission–Line Measurement

The first type of pattern consists of rectangular metal pads as shown in Fig.12. A mesa etching of the semiconductor around the pattern is required to avoid the possibility of fringe effects, which alters the measurement results. After obtaining the resistance for all different metal pad spacings, the specific contact resistance (ρ_c) and the sheet resistance (R_{sh}) can be obtained by plotting the resistances as a function of metal–pad spacing as shown in Fig.13. The sheet resistance of semiconductor material can

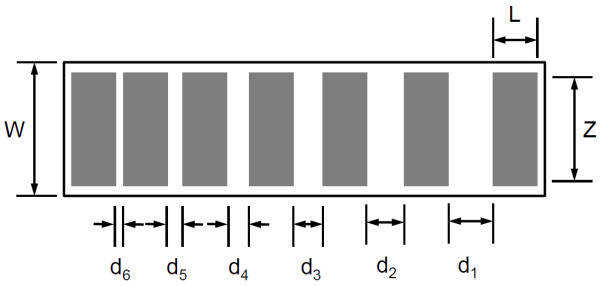

Figure 12: A typical rectangular TLM pattern showing the differences in metal contact pads spacings.

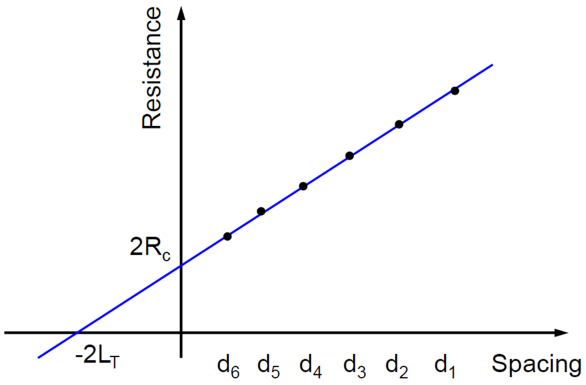

Figure 13: An example plot of measured resistances as function of spacing.

be obtained from the following equation:

$$R_{sh} = slope \times Z \quad (\Omega/\square) \tag{29}$$

where Z is the length of the metal pads as shown in Fig.12. When the contact separation becomes zero, the intercept of the line at the y–axis (resistance axis) corresponds to twice the contact resistance, $2R_c$. On the other hand, when the resistance becomes zero, the intercept of the line at the x–axis (metal–pads spacings) is two times the transfer length, $2L_T$. The specific contact resistance can be calculated as:

$$\rho_c = R_c \times Z \times L_T \quad (\Omega - cm^2) \tag{30}$$

The rectangular TLM pattern used in this thesis has metal pad dimensions $L = 50\mu m$ and $Z = 80\mu m$ while the spacings are 4 μm, 8μm, 16 μm, and 32 μm.

2.8.2 Circular Transmission–Line Measurement

Unlike rectangular TLM pattern, circular TLM (CTLM) doesn't require a mesa etching since the pattern itself eliminates the possibilities of fringe effect [46]; however, CTLM usually has larger patterns, which require more wafer area compared to linear (rectangular) TLM. A CTLM test structure consists of a metal stack for circular inner region with radius L, a gap of width d, and a metal stack for outer region as shown in Fig.14. The total resistance between the internal and the external contact can be

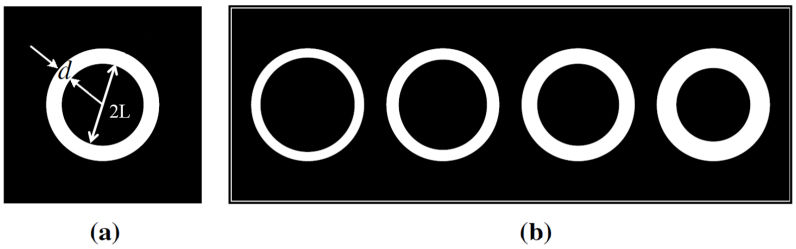

Figure 14: An example of CTLM test structure. The dark regions represent metal contacts. Spacing d and radius of inner circle are shown in panel (a).

formulated as:

$$R_T = \frac{R_{sh}}{2\pi}\left[\frac{L_T}{L}\frac{I_0(L/L_T)}{I_1(L/L_T)} + \frac{L_T}{L+d}\frac{K_0(L/L_T)}{K_1(L/L_T)} + ln\left(1+\frac{d}{L}\right)\right] \tag{31}$$

where L_T is known as transfer length, I and K denote the modified Bessel functions of the first order. In the practical design L $\ll$ 4L$_T$, the Bessel function ratios I_0/I_1 and K_0/K_1 tend to become unity, which simplifies Eq.31 to:

$$R_T = \frac{R_{sh}}{2\pi}\left[\frac{L_T}{L}\frac{L_T}{L+d} + ln\left(1+\frac{d}{L}\right)\right] \tag{32}$$

The only two unknowns in the Eq.32, R_{sh} and L_T, can be calculated based on the total resistance measurement on different spacings. The specific contact resistance

can be calculated from the relation:

$$\rho_c = L_T^2 R_{sh} \tag{33}$$

The CTLM test structure performed in this work has $L+d = 120\mu m$ or $L+d = 200\mu m$ while the spacing d varies from 4 μm, $8\mu m$, 16 μm, 32 μm, and 64 μm.

2.9 X–Ray Diffraction

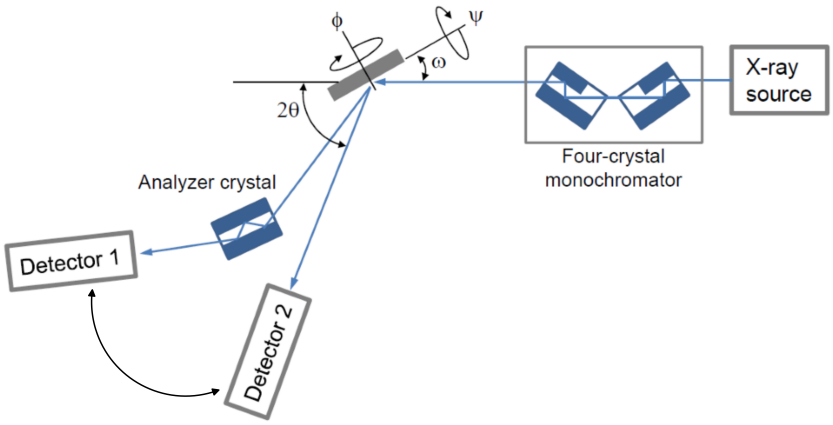

Figure 15: Schematic diagram for a typical HRXRD measurement system. [46]

X–ray diffraction (XRD) is a non–destructive process used to analyze the thickness, lattice parameters, strain, composition, degree of relaxation, and defect densities of epitaxial layers and device structures. In this work, all the XRD scans were measured by a Phillips X'Pert MRD (Material Research Diffractometer) High Resolution X–ray diffractometer (HRXRD). The X–ray source is generated from Cu $K_{\alpha 1}$ transition, which emits X–ray with wavelength of 1.540562 $\mathring{A}$. The X–ray beam is then collimated by four–bounce Ge(220) Bartels monochromator before impinging on the sample. Once the beam is "diffracted" from the sample, two different diffracted beam paths are available. The main difference is that one of the diffracted beam paths has an analyzer crystal (also known as a beam conditioner) installed, which provides a

beam with an angular resolution below 1 arcsec. A typical configuration of a HRXRD measurement system is shown in Fig.15 [47].

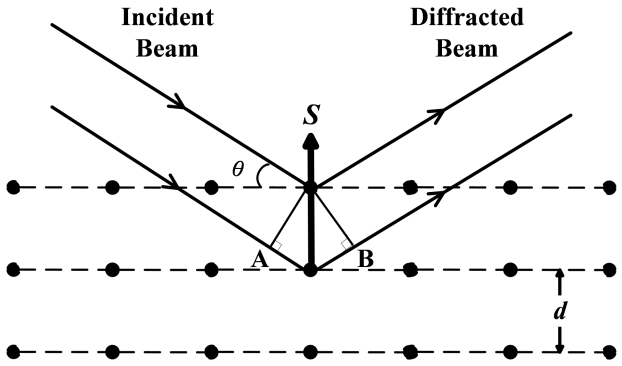

Figure 16: The Bragg condition for diffraction is shown. AB is defined as the path length difference (nλ), d is crystal plane spacing, θ defines the angle between incident beam and the crystal plane, and $\vec{S}$ represents scattering vector. [47]

The fundamental process employed in XRD is probing a crystal with X–ray radiation having a wavelength (λ) smaller than the crystal lattice spacing, as shown in Fig.16 [48]. When the X–rays are scattered by the electron cloud surrounding each atom in the crystal, constructive interference occurs if and only if the the path length difference is equal to $2d\sin\theta$, which is also known as Bragg's law. Experimentally, the angle 2θ is measured and the diffraction pattern is related to the spacings of the crystal planes and size of crystallites. In order to investigate different diffraction spots, measurement angles (ω, 2θ, ϕ, and ψ) are altered to meet the Bragg condition, as shown in Fig.16 [48].

By sweeping different angle or angles for diffraction, the XRD measurement provides various information about the material. For instance, ω-scans are usually used for measuring the film quality since the diffraction peak broadening by dislocations can be easily seen. In the Hirsch model, dislocation density can be formulated as

$$\rho_c = \frac{\beta^2}{9b^2} \tag{34}$$

Table 3: Summary of different scan types available on high–resolution X–ray diffractometers [47].

Scan type	Description
2θ–ω	The sample is rotated by ω and the detector is rotated by 2θ with an angular ratio of 1 : 2. In reciprocal space, scattering vector ($\vec{S}$) moves outwards from the origin. The length of $\vec{S}$ changes, but its direction remains the same and depends on the offset. For 2θ–ω scans, the x–axis is in units of 2θ, whereas for ω–2θ, the x–axis is in units of ω. When there is no offset and $\omega = \theta$ this is a symmetrical scan (θ–2θ) which is vertical in reciprocal space. Standard scan type for powder diffraction.
ω–2θ	Simply a 2θ–ω scan, but with ω on the x–axis. Standard scan type for reflectivity and high–resolution work.
2θ	The sample and source remain stationary and the detector is moved. $\vec{S}$ traces an arc along the circumference of the Ewald sphere. Both the length and the direction of $\vec{S}$ change.
ω	The detector remains stationary and the sample is rotated about the ω axis. In reciprocal space, $\vec{S}$ traces an arc centered on the origin. The length of $\vec{S}$ stays the same, but its direction changes.
Q	Software can be used to scan ω and 2θ in non–integer ratios, scanning $\vec{S}$ along a given direction in reciprocal space. Reciprocal space maps of any desired shape can then be collected.
ϕ	Rotation of the sample about the ϕ axis. The length of $\vec{S}$ stays the same, but the sample is moved, bringing the reciprocal lattice spot through $\vec{S}$ so that the direction of $\vec{S}$ changes with respect to the sample.
χ	Similar to ϕ scans, except that the sample is rotated about the χ axis.

where β describes the broadening (FWHM) of the rocking curve in radian and b is the Burgers vector in cm. On the other hand, ω–2θ or 2θ–ω scans probe the diffraction spots along the direction that typically has less broadening; thus, these scans are usually used for lattice parameter or composition determination. Both ω and ω–2θ scans are also known as "rocking curves", as both scans involve 'rocking' the sample about the ω–axis. Table 3 summarized different scan types that are commonly used

in XRD [48].

In order to understand the information on interplanar spacings and defect–related broadening, a reciprocal space map (RSM) can be used to verify the information. An RSM consists of a series of ω–2θ scans at successive ω values and presents the results in map form. An RSM measurement is recorded in angular units; thus, the units should be converted into reciprocal lattice units (RLUs) for proper analysis. The following equations relate the coordinates of the reciprocal point (Q_x, Q_y) with the angular units ω and 2θ:

$$Q_x = \frac{2\pi}{\lambda}\left[\cos\omega - \cos(2\theta - \omega)\right] \tag{35a}$$

$$Q_y = \frac{2\pi}{\lambda}\left[\sin\omega + \sin(2\theta - \omega)\right] \tag{35b}$$

Figure 17 shows an example of RSM for AlGaN grown on AlN template on sapphire substrate. The Q_y axis represents the reciprocal lattice constants in the vertical direction (c–axis), which indicates the difference in the composition. On the other hand, difference in Q_x axis refers to the difference in the in–plane lattice constant (a–axis), which is a very important parameter to determine the in–plane percentage relaxation ($R_{\%}$). The percentage relaxation can be calculated as [49]

$$R_{\%} = \frac{d_{\parallel}^{L(meas)} - d_{\parallel}^{Sub(meas)}}{d_{\parallel}^{L(0)} - d_{\parallel}^{S(0)}} \times 100 \tag{36}$$

where $d_{\parallel}$ is the in–plane lattice spacing and superscripts L denotes layer, Sub denotes substrate, 0 refers to to reference lattice parameter, and $meas$ represents the measured value.

In order to calculate the percent relaxation of the layer, a method to determine the lattice parameter is required. From Bragg's law ($n\lambda = 2d_{hkl}\sin\theta$), the angle θ is required for obtaining the distance d_{hkl} between a particular set of planes. In the hexagonal material system, the following equation relates the d_{hkl} to the lattice parameters a and c

$$\frac{1}{d_{hkl}^2} = \frac{4}{3}\frac{h^2 + k^2 + hk}{a^2} + \frac{l^2}{c^2} \tag{37}$$

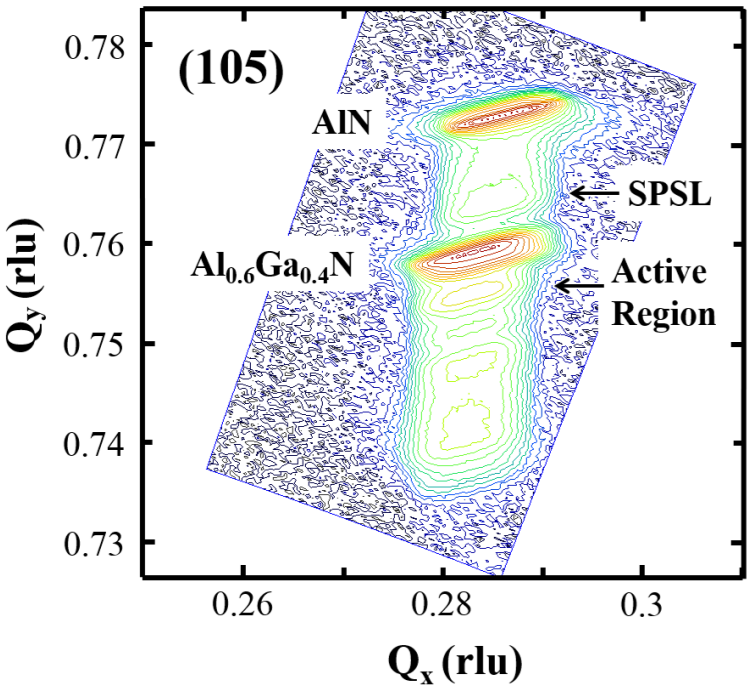

Figure 17: The angular and reciprocal space representation of an RSM measurement.

Since there are two lattice parameters (unknowns) to be determined, two d_{hkl} measurements are required. Typically, one high–angle "symmetric" reflection is measured (e.g., d_{0002}), from which the lattice constant c can be found directly. Then another high–angle "asymmetric" reflection is measured (e.g., $d_{20\bar{2}4}$). Using the value of c found previously, the lattice constant a can be extracted. Utilizing Eq.36, the composition and the relaxation of the film grown on the substrate can be obtained.

As mentioned earlier, the XRD measurements performed in this work are taken using a Philips X'Pert MRD HR–XRD with a Cu $K_{\alpha 1}$ source and four Ge (220) crystals as the beam monochrometer. The system is equipped with two separate detector optics; beam path 2 has a typical configuration used for the rocking curve scans, while beam path 1 is equipped with a Ge (110) channel–cut crystal that is aligned to the (220) reflection as an analyzer crystal for the RSM scan.

CHAPTER III

EFFICIENT VERTICAL HOLE TRANSPORT IN UV EMITTERS

3.1 Introduction

III–N–based optoelectronic devices have been actively studied and developed due to a wide range in direct bandgap energy, which covers the full spectrum of optical emission from the near–infrared to deep–UV. Today, UV semiconductor light emitters serve many applications in modern society, such as high–quality UV LEDs that are commercialized for water sanitation and bio–chemical agent detection applications. An essential key to fabricate an efficient UV emitter is to efficiently inject holes into the active region through highly conductive p–type layers. However, magnesium (Mg), the commonly used p–type dopant in III–N material system, has large activation energy. The issue aggregates as the material bandgap widens due to the fact that electrically active concentration of ionized impurity atoms is limited by the Fermi–Dirac distribution as

$$N_A^- = \frac{N_A}{1 + g_A e^{(\frac{E_A - E_{F,p}}{k_B T})}} \tag{38}$$

where N_A is the chemical concentration of the substitutional acceptors, g_A is the degeneracy factor, E_A is the acceptor activation energy, and $E_{F,p}$ is the quasi–Fermi level for holes. In addition to the limitation in the electrically active concentration of holes, the large effective mass for holes further worsens the situation. The limitation in the p–type material conductivity can lead to an increase in Joule heating and the parasitic series resistance that causes additional voltage drop for electrical devices.

To tackle the vertical hole transport issue, Cheng, et al., utilized an $Al_xGa_{1-x}N$/

$Al_yGa_{1-y}N$ superlattice (SL) as a p–waveguide layer to enhance vertical hole transport while maintaining the UV optical transparency. Current densities of 11 kA/cm^2 and 21 kA/cm^2 were demonstrated under DC and pulse measurement conditions, respectively. [50] Even though the demonstrated high current density shows a potential avenue to realize UV LDs, the p–SL design induces an artificial hole blocking layer and leads to a large diode turn–on voltage which is accompanied by serious Joule heating resulting in a limitation on the achievable optical gain. Instead of a p–SL design, we employed an inverse–tapered design whose bandgap energy decreases along the growth direction as reported by Satter, et al., [51] which allows us to reach a similar current density at a significantly lower voltage as reported in this work.

3.2 Energy Band Diagram Analysis

To understand the origin of the relatively high turn on voltage as well as the artificial hole blocking layer, numerical simulations for various valence–band structures were used to to study the vertical hole transport path. Table 4 describes the device structure employing the inverse–tapered p–waveguide design, which was designed by Dr. Satter based on Ref. [51], and the corresponding valence band diagram is shown in Fig. 18 (a). Since hole transport mainly takes place between the p–ohmic metal and the active region, the study only focuses on this region of the valence band diagram instead of analyzing the full device structure. On the other hand, Fig. 18 (b) presents a different p–waveguide structure, which was designed by me for comparison purpose, by employing a p–SL design with an additional example of an abrupt valence–band discontinuity in the p–waveguide. The p–SL design used an $Al_{0.6\rightarrow0.3}GaN$ grading layer and eighty periods of $Al_{0.4}Ga_{0.6}N/Al_{0.8}Ga_{0.2}N$ (2.5 nm/2.5 nm) SL structure as material for p–waveguiding_1 and p–waveguiding_2 of Table 4, respectively. The two equilibrium valance band structures presented in Fig. 18 were provided by Dr. Satter to provide additional visual aid for my following analysis.

Table 4: A simulated laser diode structure.

Layer Name	Material	Thickness (nm)	Doping Concentration (cm^{-3})
Contact	GaN	20	1e19
P–waveguiding_1	$Al_{0.60\rightarrow0}GaN$	150	1e19
P–waveguiding_2	$Al_{0.60}GaN$	400	1e19
P–waveguiding_3	$Al_{0.47\rightarrow0.60}GaN$	50	1e19
Spacer	$Al_{0.47}GaN$	5	1e19
QW(×4)	$Al_{0.32}GaN$	2	UID
QWB(×4)	$Al_{0.47}GaN$	5	UID
Grading	$Al_{0.60\rightarrow0.47}GaN$	50	-1e18
N–waveguiding	$Al_{0.60}GaN$	500	-1e18
SPSL	(4nm $Al_{0.75}GaN$| 4nm $Al_{0.60}GaN$)×12	96	-1e18
Buffer	$Al_{1.00\rightarrow0.75}GaN$	200	-1e18
Substrate	AlN	-	-

Comparing the valence–band structures shown in Fig. 18 starting from the surface of the p–GaN contact layer, a step–like potential barrier was found in Fig. 18 (b) highlighted with red dashed boxes at the GaN/$Al_{0.3}Ga_{0.7}N$ interface. This valence–band discontinuity can trap holes at the interface, which requires even larger bias to drive carriers through, resulting in larger turn–on voltages. The UV LD demonstrated by Yoshida, et al., has this valence–band discontinuity in their design and our simulation suggests that this discontinuity contributes to a larger turn–on voltage as was observed [52]. To minimize the hole–trapping effect at the interface described previously, one approach is to reduce the valence–band discontinuity. In addition to that, we can take the advantage of polarization charge in wurtzite materials, a compositionally graded p–$Al_xGa_{1-x}N$ layer can form a smoother valence band structure as shown in Fig. 18

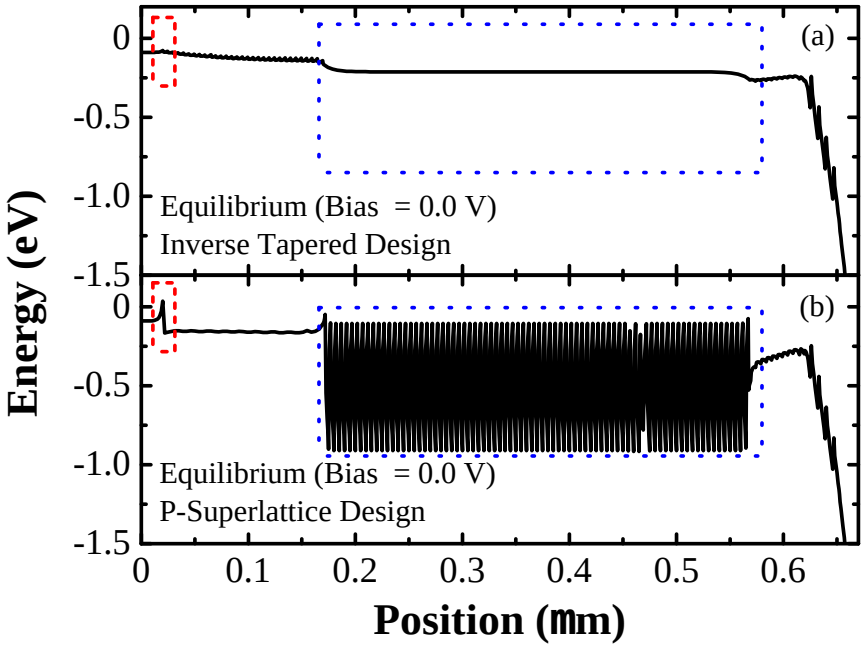

Figure 18: Electronic band structure of valence band between the p–GaN contact and the active region for (a) inverse–tapered design and (b) superlattice design in the p–type $Al_xGa_{1-x}N$ waveguide layers. Two main differences in the band structures are highlighted with red and blue boxes. (Credit to Dr. Satter)

(a). Furthermore, the biggest advantage of the polarization charge is the volumetric redistribution of the fixed negative polarization charge throughout the waveguide which electrostatically attracts the holes toward active region [51]. Another difference between the two valence–band diagrams in Fig. 18 is the use of a constant–composition $Al_{0.6}Ga_{0.4}N$ layer versus an $Al_{0.4}Ga_{0.6}N/Al_{0.8}Ga_{0.2}N$ SL for the p–type waveguiding_2 layer of table 4 as highlighted with blue dotted boxes. As discussed earlier, the valence–band discontinuity creates potential barriers along the hole transport path. Although the potential barriers are thin in the SL case, the large effective mass of holes results in a short coherence length, which is about two orders of magnitude less than the thickness of the p–waveguiding_2 layer. As a result, tunneling

cannot be be a significant contributor for hole–transport and a larger bias is required to achieve a given hole concentration in the active region. On the other hand, the inverse–tapered $Al_xGa_{1-x}N$ *p*–waveguide design exhibits a relatively smooth valence–band structure between the *p*–contact layer and the active region, which reduces the parasitic resistance through the *p*–type region. The SL design might be more beneficial in current spreading than the inverse–tapered design when the current spreading in the metal electrode is limited, which may be the case of surface–emitting UV LEDs. Lateral transport of holes in the *p*–waveguide/cladding of edge–emitting LDs and in hole–injection layer of backside–emitting LEDs will not be a major issue of design concern.

3.3 Experimental Procedures

To experimentally determine if the inverse–tapered *p*–waveguide design can reduce the device turn–on voltage while maintaining high current densities, an AlGaN–based UV MQW double–heterojunction (DH) emitter structure was grown on an aluminum–polar (0001) native AlN "bulk" substrate. The epitaxial growth was performed in a Thomas–Swan (now AIXTRON) 6×2" close–coupled showerhead metalorganic chemical vapor deposition (MOCVD) reactor system. Sigma-Aldrich Fine Chemicals (SAFC) Epipure® trimethylaluminum (TMAl) and trimethylgallium (TMGa) were used for group III precursors while ammonia (NH_3) was used for the group V precursor. Silane (SiH_4) and bis-cyclopentadienylmagnesium (Cp_2Mg) were used for *n*–type and *p*–type dopant sources, respectively. The AlN substrates were etched in a 3:1 H_2SO_4:H_2PO_4 solution at 90 °C as described in Ref. [53] before being loaded into a growth chamber. High–temperature (∼1100 °C) annealing in a high–purity NH_3 and H_2 ambient was performed to desorb any remaining surface oxide prior to the epitaxial growth. Next, the growth chamber was ramped to a growth temperature of ∼ 1150 °C and a growth pressure of 75 Torr for smooth epitaxial layer formation.

The V/III ratio ranged from less than 100 for AlN as well as high AlN mole fraction $Al_xGa_{1-x}N$ material growth to $\sim$ 2000 for GaN–rich material. In the mean time, the growth temperature was reduced from $\sim$ 1150 °C to $\sim$ 1060 °C corresponding to the increase in the GaN mole fraction ternary layers.

Following the epitaxial growth, the wafers were fabricated into narrow–mesa ridge waveguide UV emitter devices by Dr. Kao and the process flow is described as below: The ridge and mesas were first formed by inductively–coupled plasma reactive–ion etching (ICP–RIE). To avoid dry etching damage, a more chemically driven etching mechanism was performed; therefore, the ridege sidewalls were formed with an angle of $\sim$ 80 ° respect to the mesa. To ensure smooth sidewalls formation to avoid leakage current path, photoeletrochemical (PEC) etching of the mesa sidewalls was performed with a 150 W Xe arc lamp. A vanadium–based metal stack (V/Al/Ti/Au = $300\mathring{A}/500\mathring{A}/300\mathring{A}/500\mathring{A}$) and a nickel–based metal stack (Ni/Ag/Ni/Au = $50\mathring{A}/500\mathring{A}/200\mathring{A}$) were deposited for n–type and p–type ohmic metal contacts, respectively. Due to the thermal conductivity differences between sapphire and AlN bulk substrates, the metal annealing recipe (10 minutes at 450 °C and 30 seconds at 850 °C in nitrogen ambient for n–metal while 450 °C for 2 minutes in compressed air for p–metal) originally developed for similar structures on sapphire substrates cannot directly transfer to the structures on AlN substrates. The transmission–line measurement (TLM) data showed slightly non–ohmic behaviors for the p– and n–contacts. Surface passivation using spin–on–glass (SOG) was performed to enhance both electrical and optical confinement of the device. Access via holes were subsequently opened in the SOG using a Plasma–Therm ICP–RIE system. Next, a 1–μm-thick Ti/Au interconnect layer was deposited by an e–beam evaporator system to complete the front–side device processing. Next, the back–side of wafer was lapped and polished down to 40 $\sim$ 50 μm to reduce the Joule heating of device under high bias, and cleaved facets along m–planes were formed subsequently.

3.4 Results and Discussion

The epitaxial structure employed in this study is as shown in Table 1 except the listed doping concentrations are only used for the purpose of simulation. To understand the actual electrical characteristics for various n–type AlGaN layers with optimized silane dopant source flow, Hall measurements and CTLM measurements were performed. A summary of the free electron concentration (n), electron mobility (μ), and bulk resistivity (ρ) can be found in table 5. On the other hand, electrical characterizations for p–type AlGaN can be more limited since Hall and CTLM measurements require ohmic contacts and these contacts can be extremely challenging due to lack of large work function metals and limitations in the achievable free–hole concentration for the p–type AlGaN layers. However, it is known that material resistance dominates in CTLM measurements under high bias. As a result, an estimated bulk resistivity for p–AlGaN can be extracted as table 6. Due to lack of certainty of the free hole concentration, SIMS measurements were performed to obtain the chemical concentration of Mg and it was found that a doping concentration of $\sim 3 \times 10^{19}$ cm^{-3} was achieved for the entire p–waveguide structure presented in table 4. The achieved electrical properties of AlGaN layers demonstrated a very close match (within an order of magnitude in terms of chemical concentration) to that of the doping concentration used in the simulation.

Table 5: Summary of electrical properties from n–type AlGaN.

Sample Description	n (cm^{-3})	μ (cm^2/V·s)	ρ (Ω·cm)
n–$Al_{0.73}Ga_{0.27}N$	7.1×10^{17}	8.872	0.65
n–$Al_{0.6}Ga_{0.4}N$	8.9×10^{17}	12.7	0.52
n–$Al_{0.47}Ga_{0.53}N$	2.1×10^{18}	23.8	0.12

Compared to a conventional III–N LD structure, an electron blocking layer (EBL)

Table 6: Summary of the electrical properties of p–type AlGaN.

Sample Description	ρ (Ω·cm)
p–$Al_{0.6}Ga_{0.4}N$	18.25
p–$Al_{0.47}Ga_{0.53}N$	8.75
p–$Al_{0.4}Ga_{0.6}N$	7.25

was not used; instead, a graded–index (of refraction) separate–confinement heterostructure (GRINSCH) design was used to confine both the carriers and the optical mode at the same time, which is a structure commonly used in traditional III–V LDs. To verify the grown structure, the wafer was examined by high angle asymmetric (105) reciprocal–space mapping (RSM) taken by a high–resolution triple–axis X–ray diffractometer as shown in Fig. 19. The vertical axis Q_y, plotted in reciprocal lattice units or rlu ($\mathring{A}^{-1}$) represents the reciprocal of the lattice constant c and the horizontal axis Q_x represents the reciprocal of the in–plane lattice constant a. The two most recognizable peaks in the data are the AlN substrate peak and that of the $Al_{0.6}Ga_{0.4}N$–waveguiding layers (for both p– and n–) as labeled. Between these two peaks, the X–ray diffraction from the $Al_xGa_{1-x}N$ graded buffer layer and the short–period SL structure that was used between buffer and n–waveguiding layers are shown along the reducing Q_y direction. The rest of the structure includes the MQW active region as well as the $Al_xGa_{1-x}N$ graded layer between the waveguiding and the GaN p–contact layers. Proper grading in the p–waveguide layer plays a vital role for implementing an inverse–tapered design since any compositional discontinuity can result in an artificial blocking layer for the transport of holes. While the change along Q_y provides vital information regarding the chemical composition of the material, Q_x provides the strain information throughout the structure. Since Q_x is the reciprocal of the in–plane lattice a, any changes in average Q_x reflects the changes in in–plane lattice constant or relaxation. Figure 19 clearly shows and example of lattice relaxation by

comparing changes in average Q_x value for $Al_{0.6}Ga_{0.4}N$ layer and AlN substrate.

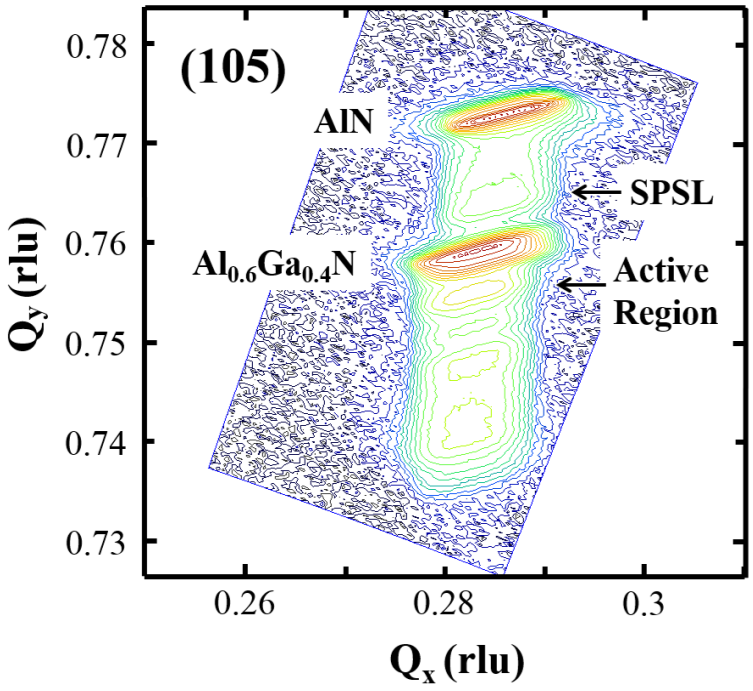

Figure 19: Asymmetric X–ray reciprocal–space mapping (RSM) based on the (105) diffraction peaks of the AlGaN UV multiple–quantum well (MQW) double–heterostructure (DH) emitter. The rlu variable represents the reciprocal lattice unit.

After device fabrication by Dr. Kao, a series of measurements were performed on MQW DH emitters and the following presented measurement result was acquired by me and Dr. Kao together. Figure 20 illustrates the I–V curves of a device under a DC condition and the inset of Fig. 20 presents the I–V curve on a semi–log scale. Based on the measurement results, the leakage current was determined to be less than 0.1 pA ($J < 2$ nA/cm^2), suggesting that high–quality epitaxial material was achieved on the AlN substrate. The p–n junction ideality factor (n) was determined to be 7.4 arising from the non–ohmic contact properties as well as the carrier confinement from the active region and GRINSCH structures. Even though the non–ohmic metal contacts

contributed an additional voltage to the device turn–on voltage, the diode has a turn–on voltage at ∼9 V , which is significantly lower than the value of ∼15V reported previously for similar structures.[50] On the other hand, the controlled sample grown on AlN template on sapphire substrate has a turn–on voltage of ∼ 7V with ohmic contacts. At the maximum measured forward voltage of 15 V, the device sustained a current level of at least 500 mA, which is equivalent to a current density of ∼10 kA/cm^2, and the series resistance at this current density was measured to be ∼15 Ω.

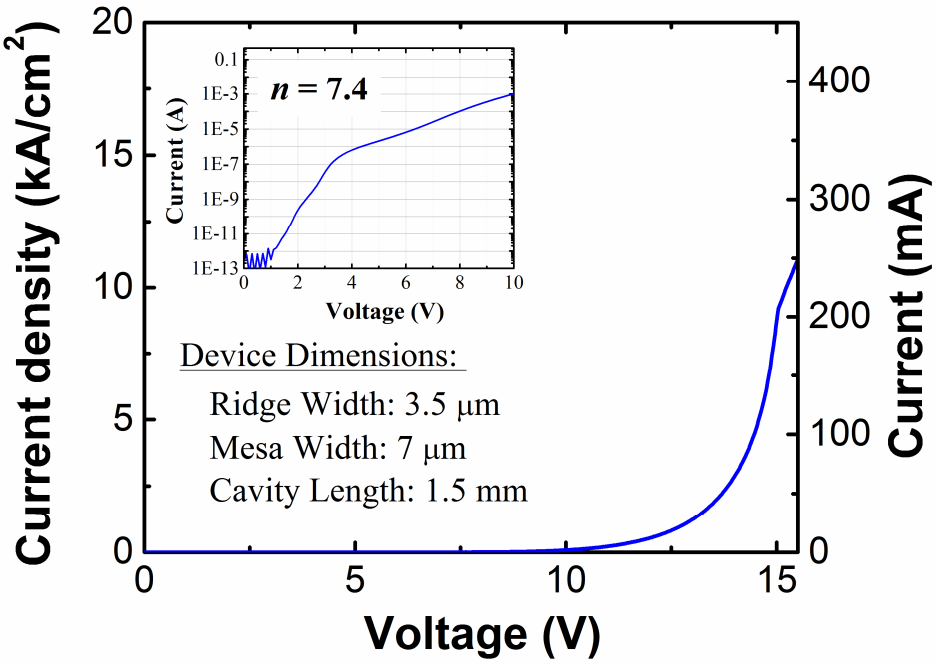

Figure 20: Current–voltage (I–V) characteristic of the UV MQW DH emitter with the inverse–tapered $Al_xGa_{1-x}N$ p–waveguide under a DC measurement condition. Inset presents the I–V measurement under semi–log scale and ideality factor (n) is equal to 7.4 while leakage current is less than 1 pA. (Credit to Dr. Kao)

To further push the device performance to its limits, pulsed I–V measurements with a pulse width of 50 μs and a pulse period of 100 ms (or 0.05% duty cycle) were made and the measured I–V curve is shown in Fig. 21. To enable high–power

measurements, the high–power source measurement units (SMUs) were used that typically have less accuracy for small current readings. The maximum measured forward voltage is 20 V with the measured current of 1.07 A, which is equivalent to a current density of ∼18 kA/cm^2, and the measured series resistance at 20 V is determined to be ∼11 Ω. Although the achieved current density was not as high as the previously reported 21 kA/cm^2 [50], the thickness of the p–type $Al_{0.6}Ga_{0.4}N$–waveguiding layer was two times thicker than used in the previously reported work which certainly contributes to the additional resistance. In addition, the current pulser used in this work has 250 times longer pulse width compared to the previously reported work and more severe Joule heating can be expected.

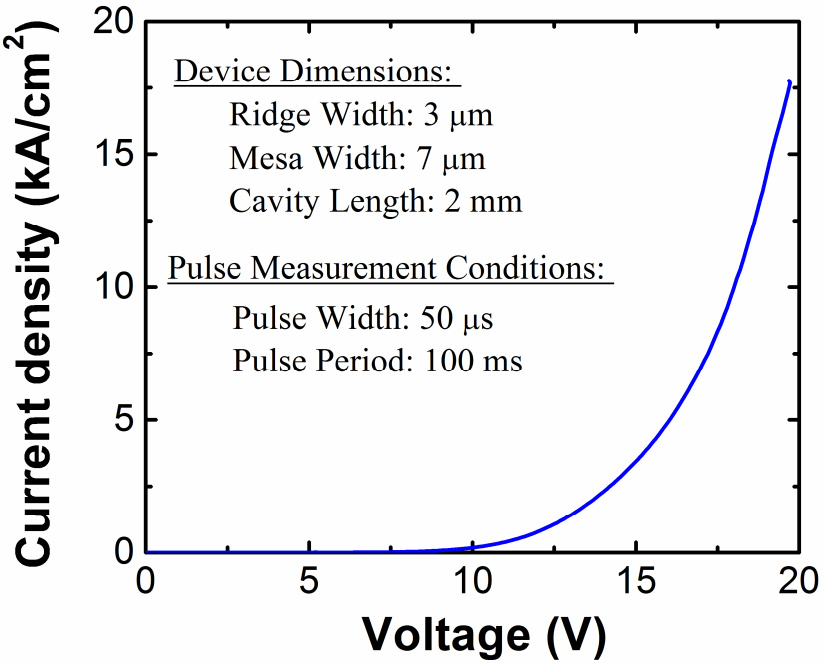

Figure 21: I–V characteristic of the inverse–tapered $Al_xGa_{1-x}N$ p–waveguide MQW DH emitter under pulsed measurements condition with a pulse width of 50 μs and a pulse period of 100 ms (or 0.05% duty cycle). (Credit to Dr. Kao)

3.5 Summary

In summary, a high–aluminum–containing ([Al] $\sim$ 0.6) AlGaN MQW DH emitter grown by MOCVD was achieved. Employing an inverse–tapered $Al_xGa_{1-x}N$:Mg p–waveguide design effectively reduces the forward resistance and leads to a reduced turn–on voltage while maintaining a high level of current conduction. The measured device can sustain a current density of 10 kA/cm^2 and 18 kA/cm^2 under DC and pulsed measurement conditions, respectively. These results show that the inverse–tapered p–waveguide design may be an effective way to improve the hole transport in wide–bandgap UV $Al_xGa_{1-x}N$ LEDs and could lead to the realization of UV LDs. With the conclusion from this study, a p–type III–N based distributed Bragg reflector (DBR) is extremely difficult to achieve with efficient vertical hole transport; therefore, a dielectric DBR will be employed for our final surface emitting laser structure. Utilizing dielectric DBR on p–side also comes in a trade off for requiring a lateral current spreading mechanism. A combination of inverse–tapered p–waveguide and lateral hole transport design will be used for our final p–spacer design.

CHAPTER IV

ELECTRICALLY CONDUCTING N–DBR

4.1 Introduction

Vertical–cavity surface–emitting lasers(VCSELs) have numerous applications including, optical fiber data transmission, optically pumped solid–state lasers, and chip–scale atomic clocks. The performance of a conventional current–injection VCSEL largely depends on the crystal quality of distributed Bragg reflectors (DBRs) composed of epitaxially grown semiconductor materials [54]. For the III–nitride material system, the growth of high–reflectivity DBR structures is extremely challenging due to the large lattice mismatch between GaN and AlN as well as the relatively low refractive index contrast of this material system. To mitigate the tensile strain originating from lattice mismatch, Waldrip, et al. [55] and Huang, et al. [56] reported the tensile strain can be compensated by inserted AlN interlayers or an GaN/AlN superlattice, respectively. Aside from strain–engineering AlGaN–based DBRs, Carlin, et al. [57] employed an AlInN ternary alloy, latticed matched to GaN, for InAlN/GaN DBR growth. Other epitaxial DBR approaches included introducing boron ternary alloy [58, 59] as well as forming air gaps between nitride materials [60, 61]. Despite the great progress in developing nitride DBRs, the majority of structures demonstrated to date limit the possibility for electrical conduction due to the wide–bandgap nature of AlN as well as the potential barriers forming from band offsets between DBR layers. Without an electrically conducting DBR structure, lateral contacts are required, which inevitably reduces the number of devices per wafer as well as increasing fabrication complexity. Unlike the majority of AlGaN/GaN heterostructures where the structure thickness is significantly smaller than the coherence length of an electron,

the total epitaxial thickness of the n–DBR significantly exceeds the coherence length of an electron resulting in difficulties in realizing the electrically conducting n–DBR. To the best of our knowledge, Arita, et al. [62] is the only research team which has reported an electrically conducting III–N DBR; however, this paper only describes the ability to pass current without any further characterization. As a result, a detailed characterization study for an electrically conducting n–DBR was carried out in this thesis research.

4.2 Experimental Procedures

In this work, we demonstrated an electrically conducting n–type DBR consisting of a silicon–doped 40–pair $Al_{0.12}GaN_{0.88}N$/GaN DBR heterostructure with the thicknesses of each layer designed to be a quarter optical wavelength thick. Utilizing the optical constants for nitrides in the literature [63], the quarter–wave thicknesses for $Al_{0.12}GaN_{0.88}N$ and GaN were determined ($t = \frac{\lambda}{4n}$) as 36.16 nm and 34.95 nm, respectively. The epitaxial growth was performed in a Thomas–Swan (now AIXTRON) 6 × 2" close–coupled showerhead MOCVD reactor system. Epipure® trimethylaluminum ($Al(CH_3)_3$, TMAl) and trimethylgallium ($Ga(CH_3)_3$, TMGa) from SAFC were used for group III precursors while high purity ammonia (NH_3) from Matheson Tri–Gas® was used for the group V precursor. To obtain n–type electrical conduction properties, silane (SiH_4) was used as the n–type dopant source. The average growth rate for this 40–pair n–DBR is about 0.8 μm/hr and the growth was performed on a $\sim$ 3.5 μm thick silicon–doped GaN template grown on a (0001) sapphire substrate in a H_2 ambient with the constant growth pressure and temperature of 200 Torr and $\sim$ 1060 °C, respectively.

The silicon–doped GaN templates were prepared by a three–step growth process. The epi–ready c–plane sapphire substrate with 0.3° offcut was first cleaned in–situ with H_2 at $\sim$ 1100 °C at 200 Torr. The growth temperature was lowered down to

540 °C and the growth pressure was increased to 500 Torr for the growth of an ∼ 20 nm thick low temperature GaN nucleation layer. Next, the growth temperature was increased to ∼ 1060 °C while the growth pressure was increased to 300 Torr to continue the 3D growth for forming "islands" tohelp reduce the threading dislocation density. Lastly, the silicon doping was introduced at growth temperature of ∼ 1060 °C and a growth pressure of 200 Torr to complete the growth of an ∼ 3.5 μm thick n–GaN template. The quality of the n–GaN template was characterized by X–ray diffraction utilizing an ω scan. The linewidth from (002) and (102) planes diffraction have typical linewidth of ∼ 230 arcsec and 270 arcsec. After completing the n–GaN template, the growth continued with a 40–pair of AlGaN/GaN n–DBR. The free–carrier concentration for the n–GaN template and each layer in the n–DBR were estimated to be 4 $\times 10^{18}$ cm^{-3} and 1 $\times$ 10^{18} cm^{-3}, respectively. The mobility for $Al_{0.12}GaN_{0.88}N$ and GaN at the given free–carrier concentration was measured to be ∼ 170 cm^2/V/s and ∼ 230 cm^2/V/s, respectively.

To study the electrical properties of the DBR, the wafer through a series of fabrication processes performed by Mr. Haq. First, a ∼ 3 μm deep mesa was created to expose the n–GaN layer below the DBR using ICP–RIE. After the mesa etching, the exposed mesa surface is treated in a diluted KOH–based solution under ultraviolet light illumination to remove the dry–etching–induced surface damage. Finally, n–type ohmic contacts, a Si–based metal alloy (Si/Al/Ti/Au = 125$\mathring{A}$/500$\mathring{A}$/250$\mathring{A}$/500$\mathring{A}$), with a 60 μm diameter circular mesa geometry were deposited on top of the mesa and the bottom of the etched access trench followed by a thermal annealing performed in a N_2 ambient at 675 °C.

4.3 Results and Discussion

Figure 22 shows the reflectivity spectra measured at 300K using a Shimadzu UV2401PC ultraviolet–visible spectrometer for a 40–pair $Al_{0.12}GaN_{0.88}N$/GaN n–DBR structure

grown on an n–type silicon–doped GaN template. The spectrometer is equipped with halogen and deuterium lamps for visible and ultraviolet wavelength measurements, respectively. In this study, the halogen lamp was used for obtaining reflectivity above

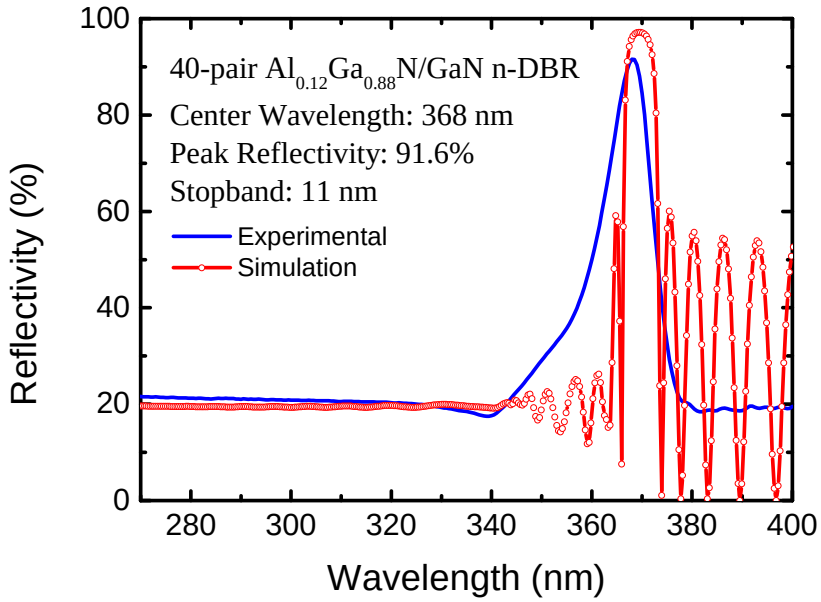

Figure 22: Reflectivity spectra for measured (blue–solid curve) and simulated (red–circled curve; Credit to Mr. Mehta) 40–pair silicon doped $Al_{0.12}Ga_{0.88}N$ /GaN DBR structure grown on a silicon doped n–GaN template.

283 nm while the deuterium lamp was used for the reflectivity between 200 to 283 nm and the measurement step was 0.5 nm. Although GaN:Si has a finite absorption around 368 nm due to excitonic absorption near the material bandgap energy [64], the measured silicon–doped $Al_{0.12}GaN_{0.88}N$/GaN DBR still demonstrated a peak reflectivity of 91.6% at 368 nm with a stopband of 11 nm. As a comparison, the ideal reflectivity spectrum, obtained via a numerical method performed by Mr. Mehta, is also shown in Fig. 22 and a peak reflectivity of 97.2% can be achieved. The calculation assumes fully strained structure and the real part of refractive index was

obtained from Ref. [63] while the imaginary part was obtained from Ref. [65]. The calculation was performed with transfer matrix method (TMM) and the complex refractive index covers the consideration of optical absorption. The nature of such narrow stopband originates from the relatively small refractive index contrast between $Al_{0.12}GaN_{0.88}N$:Si and GaN:Si. To increase the stopband bandwidth, an $Al_xGa_{1-x}N$:Si layer with larger aluminum mole fraction is required; however, increasing the Al mole fraction will create a larger electrical resistance through the n–DBR structure due to the larger potential barrier at the silicon–doped $Al_xGa_{1-x}N$/GaN hetero–interfaces resulting from an increased conduction–band offset. In addition to the limitation of carrier transport through potential barriers, higher aluminum mole fraction $Al_xGa_{1-x}N$:Si materials will experience even larger tensile strain, which usually induce defect formation and potentially cracks.

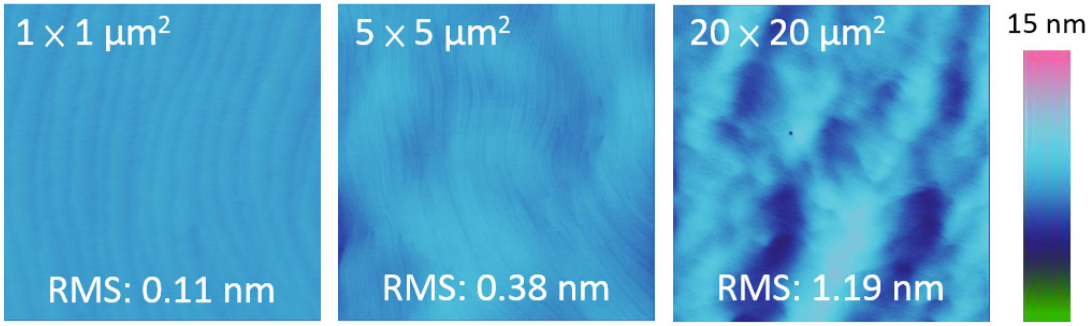

Figure 23: Atomic-force microscopy measurements of the 40–pair silicon doped $Al_{0.12}Ga_{0.88}N$/GaN DBR structure on a silicon doped n–GaN template taken at 1×1 μm^2, 5×5 μm^2, and 20×20 μm^2 and the corresponding root–mean–square roughness is 0.11 nm, 0.38 nm, 1.19 nm, respectively.

To achieve a high reflectivity with the relatively small refractive index contrast between $Al_xGa_{1-x}N$:Si and GaN:Si, a mirror like surface is required to reduce surface or interface scattering. The relation between surface roughness and the achievable

reflectivity is governed by Debye–Waller factor as:

$$R = R_0 \text{Exp}\left[-\left(\frac{4\pi\sigma}{\lambda} n \sin\theta\right)^2\right] \tag{39}$$

where R_0 is the reflectivity without any roughness, n is the refractive index of the material at the given wavelength (λ), σ is the root–mean–square (RMS) roughness, λ is the wavelength of interests, and θ is the angle of incident light. Another commonly used equation to describe the relationship between surface roughness and reflectivity is Nevot–Corce factor which is formulated as:

$$R = R_0 \text{Exp}\left[-n_i n_t \sin\theta_1 \sin\theta_2 \left(\frac{4\pi\sigma}{\lambda}\right)^2\right] \tag{40}$$

All the symbols in Nevot–Corce factor are similar to Debye-Waller factors; however, Nevot–Corce factor takes into account the differences in refractive index between two layers. As a result, the subscript i and t in refractive indexes as well as 1 and 2 for angels (θ) account the differences of two wave vectors. In addition, smooth surface formation is required for a high–quality active region growth on top of the n–DBR structure for VCSELs or microcavity light–emitting diodes (MCLEDs). Illustrated in Fig. 23 is the surface morphology of a 40–pair $Al_xGa_{1-x}N/GaN$ n–DBR grown on (0001) sapphire measured by atomic force microscopy (AFM). Even with n–type silicon doping and the tensile strain in $Al_xGa_{1-x}N$, smooth surface formation with terraced step–flow, characteristic of two–dimensional (2D) layer–by–layer III–nitride epitaxial growth, was observed. The RMS roughness is 0.11 nm, 0.38 nm, 1.19 nm for 1×1 μm^2, 5×5 μm^2, and 20×20 μm^2 measurements, respectively. To understand how this roughness will affect the achievable reflectivity, we'll take our 20×20 μm^2 AFM measurement result as an example for a numerical study. By considering the roughness of 1.19 nm and assuming normal incident light, we can calculate the surface roughness should cause the reflectivity to be reduced by 0.4% at air–semiconductor interface using the Nevot–Corce factor. Although the loss per interface seemes negligible, it is important to consider our DBR is multilayer structure has many interfaces.

By considering all the scattering loss between interfaces, the roughness can be a detrimental factor for achieving high reflectivity DBRs.

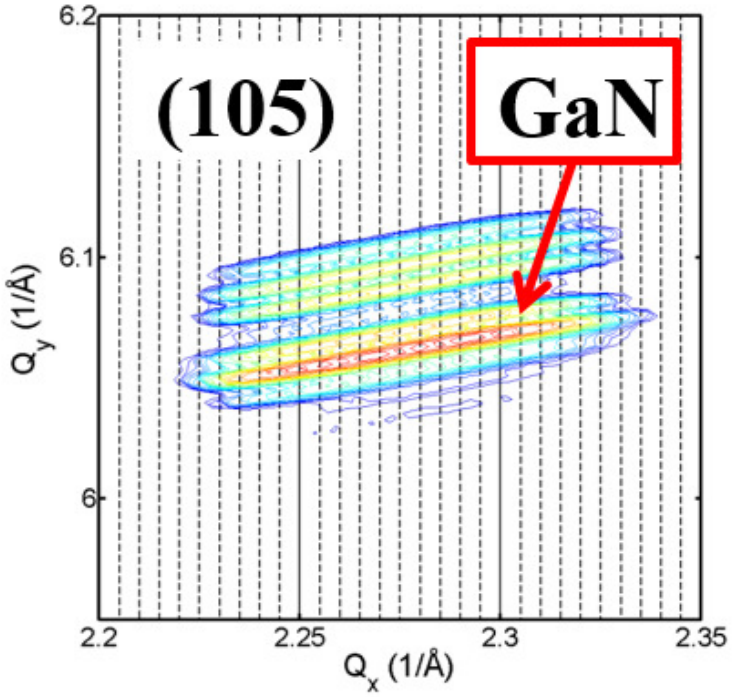

Figure 24: Asymmetric X–ray reciprocal–space mapping (RSM) based on the (105) diffraction peaks of the n–DBR. The rlu variable represents the reciprocal lattice unit.

During the modeling of the n–DBR reflectivity, a fully strained assumption was made. To verify such an assumption, high–angle asymmetric X–ray reciprocal–space mapping (RSM) on the (105) reflection plane was performed as shown in Fig. 24. The most intense peak observed from the measurement was from the n–GaN template as pointed out with the red arrow while the remaining observed peaks correspond to the n–DBR structure and its satellite peaks. Note that the entire n–DBR structure share the same average Q_x value near 2.28 $\AA^{-1}$ which indicates the n–DBR is fully strained to n–GaN template. This vital information can have significant influence on the simulated reflectivity spectrum as the biaxial strain can modify the material bandgap which also changes the optical absorption coefficient of the material and the

change in lattice constant affects the real part of refractive index.

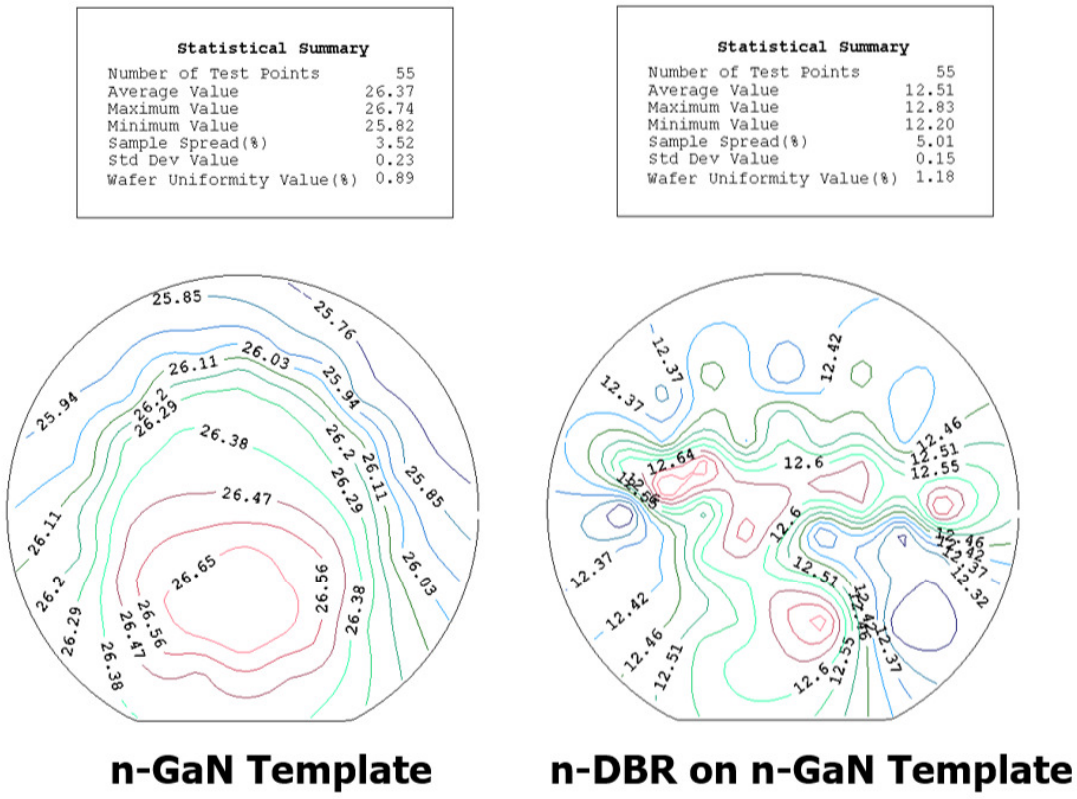

Figure 25: Sheet resistance mapping of the n–type GaN template (left) and 40–pair silicon doped $Al_{0.12}Ga_{0.88}N$/GaN DBR structure on silicon doped n–GaN template (right) utilizing LEI–1510C® system.

With the detailed characterization of the DBR by optical reflectivity measurements, surface topography by AFM, and crystal quality assessed by XRD, the n–DBR is then studied with a Lehighton sheet–resistance mapper model LEI–1510C®. Since the eddy current probing methodology is sensitive to the most highly conducting layer within a structure, it is important to understand the sheet resistance of the n–GaN template prior to study n–DBR sample. Demonstrated in the left panel of Fig. 25 is the typical sheet resistance map of 3.5 μm thick of n–GaN template. The mean sheet resistance was measured as 26.37 Ω with a standard deviation of 0.23 Ω, which

demonstrated a very uniform layer. With the growth of the n–DBR on top of n–GaN template, the same sheet resistance measurement was performed and the result is presented in the right panel of Fig. 25. Note that the average sheet resistance is now reduced down to 12.51 Ω which clearly demonstrated the n–DBR structure can promote excellent lateral conduction due to the 2–dimensional electron gas (2DEG) formed at the high index and low index material interface.

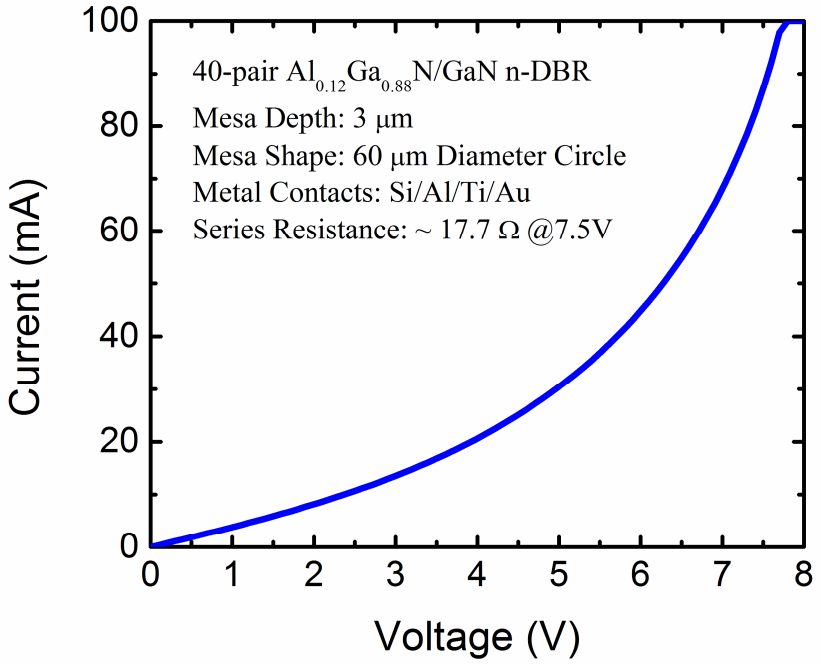

Figure 26: I–V characteristic of the 40–pair silicon doped $Al_{0.12}Ga_{0.88}N$/GaN DBR structure on silicon doped n–GaN template under a DC measurement condition at room temperature. The series resistance was determined to be 17.7 Ω near the maximum measured current of 100 mA. (Credit to Mr. Haq)

Illustrated in Fig. 26 are the current–voltage (I–V) characteristics of the n–DBR measured at room temperature under DC conditions, which was collected by Mr. Haq. The measurement was terminated at the maximum measured current of 100

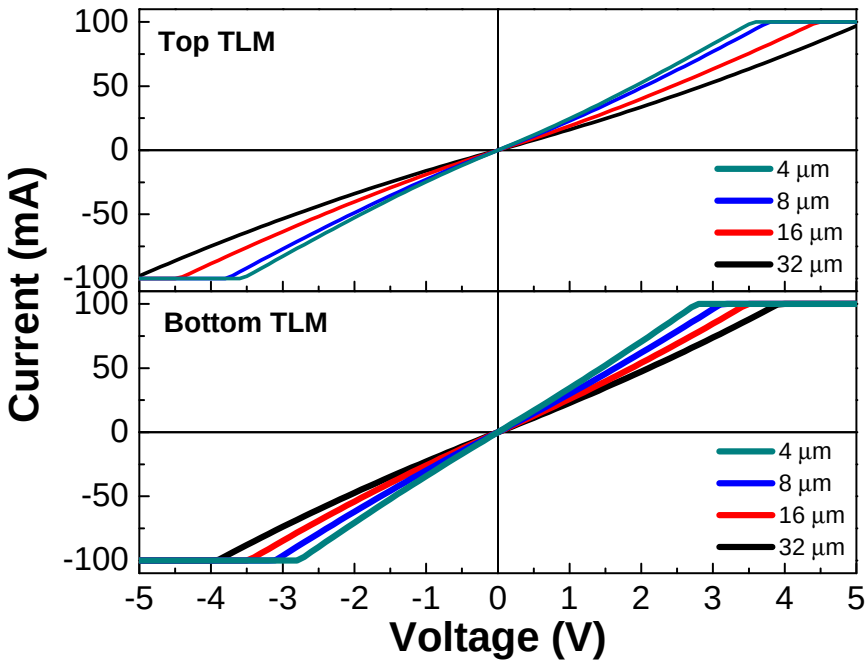

Figure 27: Transmission line measurement for metal contact on top (top panel) and the bottom (bottom panel) of the mesa. (Credit to Mr. Haq)

mA ($\sim$ 7.7 V) and non–linear I–V characteristics were observed, which may be attributed to the inhomogeneous pile–up of charge under bias, which subsequently affects the internal electrical field profile. By taking the differential of the I–V curve, the series resistance of 17.7 Ω can be determined near the maximum measured current of 100 mA. The measured series resistance is the combination of the resistance of two metal contacts, the vertical resistance through the n–DBR, and the lateral resistance on the bottom of mesa for the lateral device in this work. To extract each of the resistances from the measured series resistance, TLM measurements were performed on top and bottom of mesa to study the contacts resistances and the sheet resistances of the material as presented in Fig. 27. The measurement, which was done by Mr. Haq, shows that ohmic contacts were achieved; thus, the contact resistance for the top and bottom contacts were calculated as 7.3 and 3.6 Ω, respectively, while the lateral resistance on the bottom of the mesa contributed additional 1.3 Ω. By subtracting

contacts and lateral resistances from series resistance, the vertical resistance through the n–DBR structure can be determined as 5.5 Ω, which corresponds to an overall bulk resistivity of 0.52 Ω–cm.

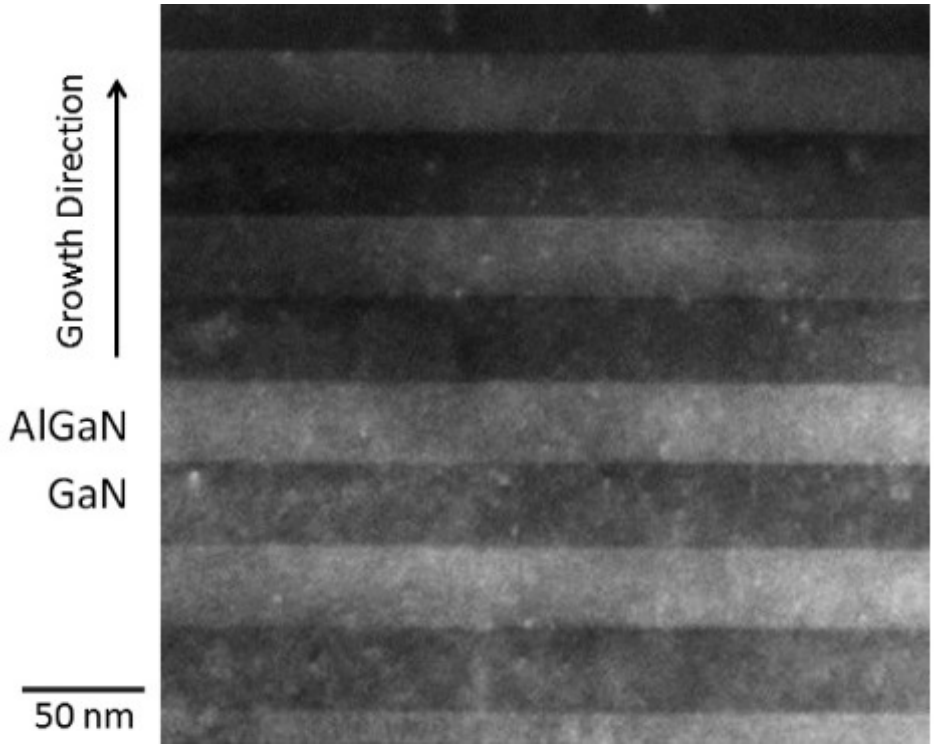

Figure 28: Large–magnification cross–section image of portion of the 40–pair silicon–doped $Al_{0.12}Ga_{0.88}N$/GaN DBR structure. This transmission electron microscopy bright–field image was taken with $g = 0002$. The brighter layers correspond to $Al_{0.12}Ga_{0.88}N$:Si while the darker layers correspond to GaN:Si. The speckles were originated from the surface damage caused by FIB process during sample preparation. (Credit to Dr. Xie)

Cross–section samples of the 40–pair n–DBR were prepared for transmission electron microscopy (TEM) measurement by our colleague Dr. Xie and Prof. F. A. Ponce at Arizona State University using mechanical polishing and focused Ga ion beam (FIB) etching to create a uniform thickness sample across the entire n–DBR structure. Figure 28 is a large–magnification cross–section image of portion of the

40–pair n–DBR, taken under bright–field conditions with $g = 0002$ collected by Dr. Xie. Abrupt and perfectly flat interfaces between the GaN:Si and the $Al_{0.12}Ga_{0.88}N$:Si layers are clearly shown with distinctive contrasts. The brighter layers correspond to $Al_{0.12}Ga_{0.88}N$ while the darker layers correspond to GaN:Si. The observed flat interfaces are important to improve the optical reflectivity by reducing the interface roughness scattering. Furthermore, the flat interfaces and the smooth surfaces (the RMS roughness for a 20×20 μm^2 scan is 1.19 nm) described in Fig. 23 are important indications that the entire n–DBR structure was grown in the Frank–van der Merwe (layer–by–layer) mode as the interfaces observed in the middle of structure and the finishing surface demonstrated comparable morphology. Since the entire n–DBR is fully strained as assessed with RSM shown in Fig. 24, the TEM analysis didn't observe any additional strain–related defect formation at the $Al_{0.12}Ga_{0.88}N$/GaN hetero–interfaces. From these images, accurate values of the thicknesses of the GaN:Si and $Al_{0.12}Ga_{0.88}N$:Si layers can be determined. The TEM thickness measurements agree very well with the nominal expected growth thickness values. The observed thicknesses deviations, which was determined to be less than 3% for both GaN and $Al_{0.12}Ga_{0.88}N$ layers, from calibrated growth using high–resolution triple–axis X–ray diffractometer can originate from run–to–run variations, wafer uniformity, and progressively slow changing in growth chamber condition throughout the growth run.

4.4 Summary

In summary, an n–type electrically conducting DBR using a 40–pair silicon doped $Al_{0.12}Ga_{0.88}N$/GaN DBR structure grown by MOCVD was demonstrated. The DBR structure exhibits a peak reflectivity of 91.6% at 368 nm with a $\sim$11 nm stopband. A high crystalline quality was verified by AFM and TEM imaging techniques. By performing a mesa–etching and metal–contact formation on this n–$Al_{0.12}Ga_{0.88}N$/GaN DBR structure, the electrical characteristics of this n–DBR can be extracted. Near

the maximum measured current of 100 mA, a vertical electrical resistance of 5.5 Ω, which corresponds to bulk resistivity of 0.52 Ω–cm was extracted. The demonstration of this n–DBR serve as the foundation of further surface–emitting devices present in this work as it achieved high–reflectivity as well as current conduction simultaneously.

CHAPTER V

AlGaN–BASED DBR WITH GaN INTERLAYER

5.1 Introduction

VCSELs have been employed in numerous applications instead of edge–emitting lasers owing to the advantages of lower threshold current operation, circular and low–divergence output beam, and lower temperature sensitivity. Much effort has been invested in III–nitride based VCSELs for the visible and ultraviolet wavelength ranges [10, 13, 14, 66] . As pointed out in previous chapter that the performance of current–injection VCSELs strongly depends on the crystal quality of the distributed Bragg reflectors (DBRs) typically composed of epitaxially grown semiconductor materials [54]. However, in the III–nitride material system, epitaxial growth of high–quality DBR structures remains an extremely difficult challenge due to the large lattice mismatch between GaN and AlN as well as the relatively low refractive index contrast of this material system. The issue can be more complicated if the target wavelength is near $\lambda = 365$ nm which is the peak emission (and absorption) wavelength of GaN. This is due to the fact that it is favorable to grow the active region on a GaN substrate while the choice of optically transparent material that can be epitaxially grown on GaN to form a high–reflectivity DBR without tensile–strain–induced cracking is, however, very limited. As a result, the refractive index contrast is further limited and a large number of DBR layer pairs is required to achieve a UV reflectivity above 90% such as exhibited by the previously reported electrically conducting n–DBR [67]. To avoid the cracking issue, an AlN substrate can be used instead of a GaN substrate. The disadvantage for using an AlN substrate is the strong compressive strain exerted on the active region will limit the quality of the material and further reduce

the achievable internal quantum efficiency. Without the high crystalline quality of the active region, the compromised quantum efficiency leads to poor device performance. To the best of our knowledge, an electrically injected VCSEL operating in this wavelength with a semiconductor DBR has not yet been reported. In this chapter, a novel strain–management method to epitaxially grow AlGaN–based DBRs on an AlN–based substrate such that it provides larger refractive index contrast than the DBRs operating in the same wavelength range grown on a GaN substrate while maintaining the strain state for high–quality active region growth.

5.2 Experimental Procedures

The epitaxial growth was performed in a Thomas–Swan (AIXTRON) 6 × 2" close–coupled MOCVD reactor system. EpiPure® Trimethylaluminum ($Al(CH_3)_3$, TMAl) and trimethylgallium ($Ga(CH_3)_3$, TMGa) were used for group III precursors while ammonia (NH_3) was used for the group V precursor. The AlN template recipe used in this work was modified from the previous reported work by Li et. al. [68] such that it is compatible to our MOCVD system with temperature operating range of less than 1150 °C. Similar to GaN template, process started from the high temperature thermal cleaning with H_2 at 1100 °C at 75 Torr. The growth temperature was then lowered to 800 °C at 75 Torr with V/III ratio of 1000 for low temperature 2 nm AlN nucleation growth. Unlike GaN template, the nucleation started with TMAl preflow to avoid mixed polarity of the III–face and the N–face on the grown surface which typically generates rough surfaces. As a comparison, GaN templates typically introduce an NH_3 preflow for nitridation (the timing is critical as too long will turn the resulting epitaxial growth into N–face) to ensure metal–face (Al) surface. The TMAl pretreatment is extremely time sensitive as well since too long may result cracked templates while too short will result in reduce surface coverage of AlN and the formation of column–like surface features. The nucleation thickness was kept at

2 nm due to the fact that AlN has very strong bounding which requires a significant amount of thermal energy to desorb material; therefore, the alternative solution is to limit the thickness of the nucleation layer. Next, the growth temperature was ramped to 1150 °C for recrystallizing the thin deposited material in an NH_3 ambient for one hour. The growth continued with two high–temperature AlN layers grown at a growth temperature of 1150 °C and a growth pressure of 75 Torr for 100 nm thick each. The only difference between the two high–temperature layers is the first layer has higher V/III ratio of 200 while the V/III ratio for second layer is reduced to 100 for promoting 3D growth initially before starting to smooth out the layer. Lastly, $\sim$ 2.8 μm thick main AlN was grown at a growth temperature of 1110 °C and a growth pressure of 37.5 Torr while the V/III ratio was kept at 50 to complete the growth. The linewidth from (002) and (102) planes diffraction have typical linewidth of $\sim$ 349 arcsec and 500 arcsec. Note that the linewidth for AlN template is roughly 85% more than the case of the GaN template if we focus on the (102) reflection plane linewidth and this is simply because AlN template does come with higher dislocation density. One thing to point out is that during the MOCVD epitaxial growth process, AlN requires significantly more thermal energy (the required growth temperature exceeded my reactor specification) to enhance the lateral growth of AlN islands. As a result, the roughening process was eliminated which leads to higher dislocation density for AlN films commonly used for MOCVD GaN epitaxial growth.

Following growth of an AlN template layer on the sapphire substrate, the temperature was lowered to $\sim$ 860 °C to grow an $\sim$ 11 nm thick GaN interlayer. The temperature was then ramped back to $\sim$ 1060 °C to complete the DBR growth. The purpose of this GaN interlayer is to manage the material strain state such that a higher quality DBR and active region can be grown on top of the AlN as reported by Wang et al. [69] The DBR reported in this work consists of 45–pairs of quarter–wavelength–thick layers of undoped $Al_{0.30}Ga_{0.70}N$ and $Al_{0.04}Ga_{0.96}N$. Although silane

doping was not introduced in this work, the relatively low AlN mole fraction (less than $x = 0.3$) still provides the possibility of electrical conduction for similar Si–doped DBRs. Compared to the AlN interlayer approach reported by Waldrip, et al. [55], our approach utilizing a single GaN interlayer significantly reduces the required epitaxial growth time as well as enabling the possibility for electrical conduction while maintaining good optical reflectivity.

5.3 Results and Discussion

A detailed analysis of the crystal structure of the DBR was performed using high–angle annular dark–field (HAADF) imaging in a JEOL ARM200F scanning transmission electron microscope (STEM), operating at 200kV by the research group lead by Prof. F. A. Ponce at Arizona State University. The sample was prepared by mechanical wedge–polishing, followed by Ar ion–milling at 4 kV. Figure 29 shows a cross–section HAADF image, along a $\{11\bar{2}0\}$ zone axis, of the 45–pair $Al_{0.30}Ga_{0.70}N/Al_{0.04}Ga_{0.96}N$ DBR on a GaN interlayer on an AlN template taken by Mr. Wang. The entire 45–pairs of the DBR with a total thickness of ~ 3.3 μm is clearly observed. The HAADF intensity at the given detector angle can be described as [70]:

$$I_{HAAFG}(q) = \left(\frac{1}{2\pi^2 a_0 q^2} Z\right)^2 \tag{41}$$

where a_0 is Bohrs radius; Z is atomic number; and $q = \frac{2\sin(\theta)}{\lambda}$ with θ referring to the scattering angle of electrons with respect to incident electron beam. The equation indicates that the intensity is roughly proportional to Z^2; therefore, in this image, the darker layers represent higher AlN mole fraction AlGaN layers, and brighter layers represent higher GaN mole fraction layers. Abrupt interfaces between the $Al_{0.30}Ga_{0.70}N$ and $Al_{0.04}Ga_{0.96}N$ layers are observed throughout the image. The average thickness for the $Al_{0.30}Ga_{0.70}N$ and $Al_{0.04}Ga_{0.96}N$ layers were determined to be 38.3 nm and 33.3 nm, respectively. The measured thicknesses represent a close match to

the intended ideal quarter-wavelength values of 37.5 nm and 35.4 nm for $Al_{0.30}Ga_{0.70}N$ and $Al_{0.04}Ga_{0.96}N$ based on the refractive index reported in the literature [63].

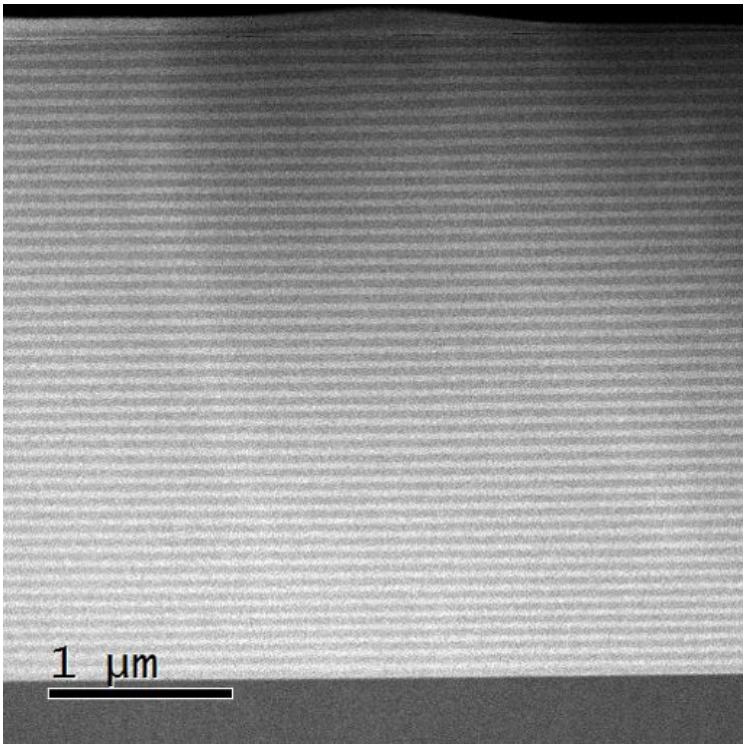

Figure 29: Cross–section HAADF image for a 45–pair $Al_{0.30}Ga_{0.70}N/Al_{0.04}Ga_{0.96}N$ DBR on a GaN interlayer on an AlN template, taken along a $\{11\bar{2}0\}$ projection. (Credit to Mr. Wang)

To further study the GaN interlayer grown in between the AlN template and the DBR, higher–magnification images were acquired by Mr. Wang. A higher–magnification cross-section image along a $\{11\bar{2}0\}$ zone axis including the GaN interlayer is shown in Fig. 30a. A thin layer of 11 nm GaN interlayer is clearly observed. Despite the lattice mismatch between AlN and GaN, the thin GaN interlayer still maintains a smooth 2–D (i.e. layer–by–layer) growth, and sharp interfaces between the AlN/GaN/AlGaN layers are observed. Without this thin GaN interlayer to manage the strain, the growth of either $Al_{0.30}Ga_{0.70}$ or$Al_{0.04}Ga_{0.96}N$ layers on AlN would likely turn into rough surface morphology [71, 72]. Although the rough surface of

AlGaN layers grown on AlN can potentially be smoothed out by growing a thicker AlGaN layer, such an approach is not suitable for UV DBR growth with quarter–wave thick layers. The rough surface formation from the initial nucleation mismatch would subsequently limit the maximum achievable reflectivity [73]. Furthermore, the GaN interlayer also prevents the possible composition-pulling effect as a strain–relief mechanism since the formation of a quasi-three–sublayer structure is also undesired and likely to occur at the AlGaN/AlN interface [74]. To verify that the GaN interlayer is grown as designed, further analysis on the acquired HAADF profile was performed by using Digital Micrograph 3.7 software. Shown in Fig. 30b is the relative intensity profile versus the relative location of the layers measured near the first–grown pair of the DBR. As discussed earlier, the HAADF intensity is roughly proportional to Z^2 and the higher intensity refers to larger GaN mole fraction. In the profile, the GaN/AlN–template interface occurs at $\sim$ 107 nm with the relatively low HAADF intensity identifying the AlN template layer. Moving along from right to left, a sharp increase in the HAADF intensity was observed which indicates our strain–management GaN interlayer. The GaN layer thickness measured from the HAADF scan matched our intended 11 nm and the rapid changes in intensity also suggest a sharp interface at the GaN/AlN hetero–interface. Notice that the composition–pulling effect as strain relief mechanism reported in Ref. [74] is not observed here and this indicates the importance of the GaN interlayer in reducing the strong compressive strain resulting from growth on AlN. Starting from the relative position of $\sim$ 95 nm is the beginning of the 45–pair of $Al_{0.30}Ga_{0.70}N/Al_{0.04}Ga_{0.96}N$ DBR structure. The thicknesses for the DBR layers shown in this profile are slightly thinner than the average value. This was observed throughout the entire DBR structure that the average thickness per pair increases along the growth direction and this may be related to a continuous shift in the growth conditions during the growth of the DBR having a total thickness of $\sim$ 3.3 μm.

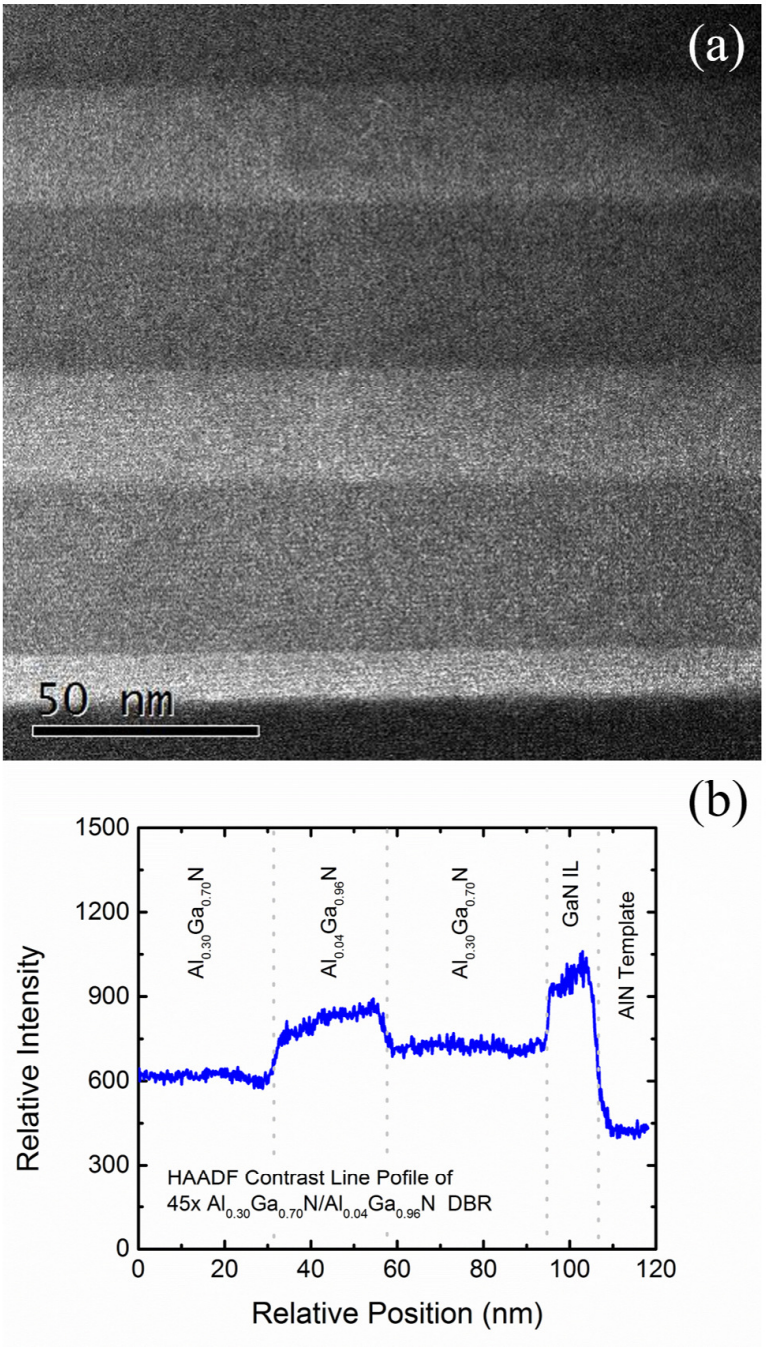

Figure 30: (a) Magnified cross-section image along a $\{11\bar{2}0\}$ projection near the AlN and GaN interlayer interface. (Credit to Mr. Wang) (b) HAADF intensity profile versus relative location for the region in (a) and the growth direction is to the left.

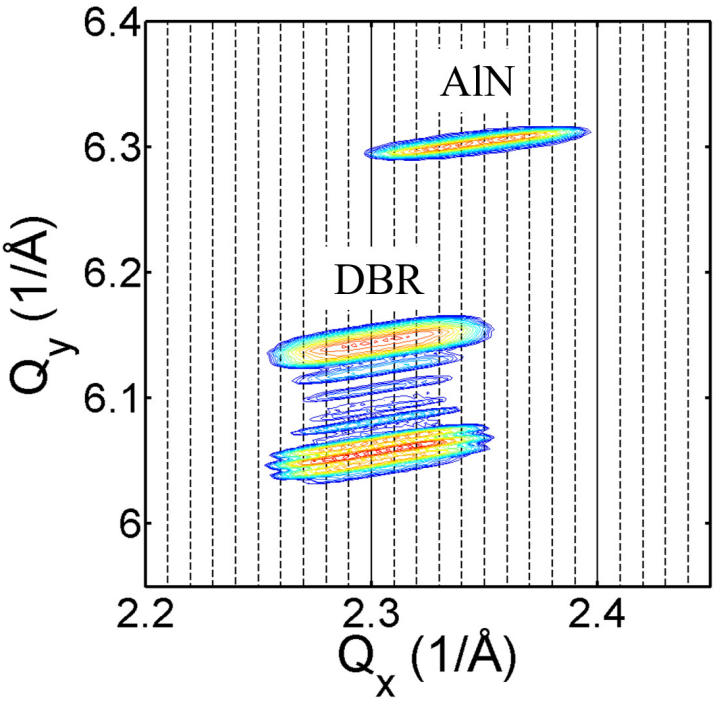

Figure 31: X–ray diffraction reciprocal–space mapping about the high–angle asymmetry plane $\{10\bar{1}5\}$ of AlN.

To study how the strain state changed for the 45–pair $Al_{0.30}Ga_{0.70}N/Al_{0.04}Ga_{0.96}N$ DBR grown on top of a GaN interlayer on AlN on sapphire, the structure was characterized using reciprocal space mapping (RSM) about a high–angle asymmetry plane $\{10\bar{1}5\}$ of AlN taken using a high–resolution triple–axis X–ray diffractometer (XRD), shown in Fig. 31. The perpendicular and parallel axes represent the reciprocal lattice c (Q_y) axis and a (Q_x) at the asymmetry plane $\{10\bar{1}5\}$, respectively. Each diffraction peak has an elongated shape due to the fact that the DBR was grown on an AlN template on a sapphire wafer instead of on a high–quality bulk AlN substrate [48]. As a result, the broadening of Q_x in the RSM originated from the relatively high dislocation density of the AlN templates was observed. The AlN template peak was found to center near $Q_x = 2.34435$ $\mathring{A}^{-1}$ and $Q_y = 6.30361$ $\mathring{A}^{-1}$ while peaks for the remaining structures were found to center near $Q_x = 2.30176$ $\mathring{A}^{-1}$. Since the thickness of the GaN

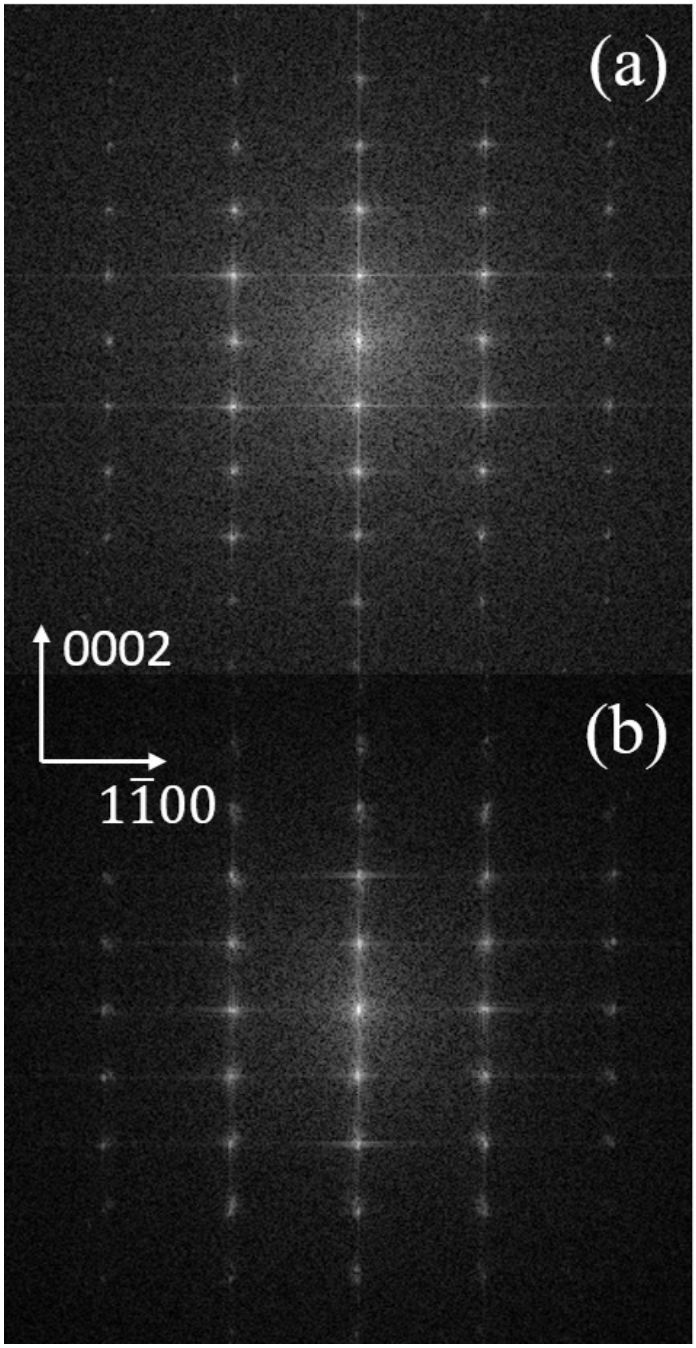

Figure 32: Fourier transform analysis on the acquired image along a $\{11\bar{2}0\}$ projection in the vicinity of (a) the DBR/GaN interlayer interface, and (b) the GaN interlayer/AlN interface.

interlayer is too thin to be resolved from RSM, it is assumed that the final strain state of GaN interlayer become closely matched to the lattice constant of the AlGaN DBR as the value of Q_x for the DBR did not change gradually. This assumption was verified by further TEM analysis utilizing Fourier transform technique.

To verify that the DBR is fully strained on the GaN interlayer and relaxation only occurs at the GaN interlayer/AlN interface, Fourier transform analysis through Digital Micrograph software was performed on the captured TEM image to acquire diffraction patterns at the interfaces. Specifically, this study focuses on the DBR/GaN–interlayer and GaN–interlayer/AlN hetero–interfaces. Shown in Fig. 32 are the diffraction patterns along a $\{11\bar{2}0\}$ zone axis, computed from the Fourier transform analysis with vertical and lateral directions corresponding to (0002) and $(1\bar{1}00)$, respectively. Since the lateral direction of the diffraction pattern reflects the changes in the in–plane lattice constant, any lattice relaxation in the material will be exhibited as additional diffraction spots that have different lateral spacings. As a result, we can evaluate the relaxation that occurs at the DBR/GaN interlayer and the GaN interlayer/AlN hetero–interfaces from Fig. 32(a) and (b), respectively. The diagonal elongated diffraction spots are observed in Fig. 32(b), which is an indication of crystal relaxation. On the other hand, Fig. 32(a) is an example of a fully strained structure as no changes in the in–plane direction were observed from the diffraction pattern. Thus, we can assume in the following calculations that the in–plane lattice constants of the GaN interlayer and the layers in the DBR are approximately constant (fully strained) since relaxation is only observed at the GaN interlayer/AlN interface from our Fourier transform analysis. The following equation relates the in–plane lattice constant a and Q_x in a hexagonal crystal system:

$$a = \frac{4\pi}{\sqrt{3}} \frac{\sqrt{(h^2 + k^2 + hk)}}{Q_x} \tag{42}$$

Using the above equation, we can extract the center (average) of the elongated peak,

as well as the in–plane lattice constant a for both AlN template and GaN interlayer, which share the same Q_x value as the 0^{th} order peak of the DBR. The in–plane percentage relaxation $R_{\%}$ of the GaN interlayer with respect to the AlN template is given by

$$R_{\%} = \frac{a_m(L) - a_m(S)}{a_0(L) - a_0(S)} \times 100 \tag{43}$$

where the subscripts m and 0 denote the measured and ideal values. On the other hand, the L and S variables represent the layer (GaN interlayer in this case) and the substrate, respectively. Utilizing in Fig. 31 the reported ideal in–plane lattice constant for AlN and GaN, [64] the calculated relaxation generated via the GaN interlayer is found to be $\sim 74\%$. The analysis with XRD and TEM clearly show that the existence of a GaN interlayer can relax the strong compressive strain from the AlN template such that the final strain states become closely match to the lattice constant of the AlGaN DBR. In addition to the observed strong relaxation, the growth of the entire DBR structure remained fully strained throughout the 45–pair DBR, which enabled smooth surface formation as shown in the previous images.

In addition to TEM and XRD analysis, Fig. 33 shows the reflectivity spectra measured at 300K by a Shimadzu UV2401PC ultraviolet–visible spectrometer with blue–solid curve. The spectrometer is equipped with halogen and deuterium lamps for visible and ultraviolet wavelength measurements, respectively. In this study, the halogen lamp was used to obtain the reflectivity for wavelengths longer than $\lambda > 283$ nm. while the deuterium lamp was used for the reflectivity between $200 < \lambda < 283$ nm, using a measurement step of 0.5 nm. Although $Al_{0.04}Ga_{0.96}N$ is not fully transparent near 368 nm due to the tail of the excitonic absorption near the material bandgap energy [64] and thus has a slight absorption, the 45–pair $Al_{0.30}Ga_{0.70}N/Al_{0.04}Ga_{0.96}N$ DBR still exhibits a peak reflectivity of 95.4% with a bandwidth of 15 nm. Furthermore, the measured average thicknesses for each of the layers obtained via TEM

analysis (38.3 nm and 33.3 nm for $Al_{0.30}Ga_{0.70}N$ and $Al_{0.04}Ga_{0.96}N$) were employed to simulate the ideal reflectivity curve as presented in Fig. 33 as a red-triangle curve which was calculated by Mr. Mehta. To account for the strain relaxation originating from the GaN interlayer based on our XRD analysis ($\sim$ 74% relaxation) and the excitonic absorption from the material, the complex refractive indices were calculated according to previous reports [63, 65]. The simulated reflectivity spectrum demonstrated a peak reflectivity of 99.7 % with a bandwidth of 13 nm. In the case for a DBR without a GaN interlayer, the peak reflectivity was slightly reduced down to 99.3 % compared to 99.7% for the DBR with a GaN interlayer. Although the GaN interlayer can introduce additional optical absorption, the increase index contrast between the GaN interlayer and the AlN template (versus $Al_{0.30}Ga_{0.70}N$ and AlN) outweighs the penalty from increased optical loss.

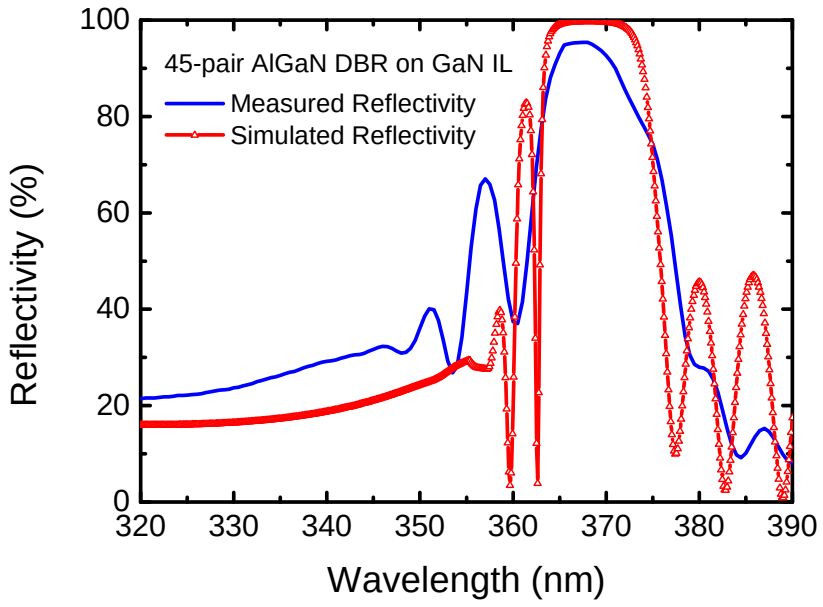

Figure 33: Measured (blue–solid curve) and simulated (red–triangle curve) reflectivity spectra for the 45–pair $Al_{0.30}Ga_{0.70}N/Al_{0.04}Ga_{0.96}N$ DBR on a GaN interlayer on an AlN template. (Credit to Mr. Mehta for simulated curve)

5.4 Summary

In summary, a crack–free growth of a 45–pair $Al_{0.30}Ga_{0.70}N/Al_{0.04}Ga_{0.96}N$ distributed Bragg reflector (DBR) by metalorganic chemical vapor deposition was demonstrated. By inserting an 11 nm–thick GaN interlayer upon the interface with the AlN template was able to properly manage the strain so that smooth low–aluminum–content $Al_xGa_{1-x}N$ layers were formed. The DBR material quality as well as the interfaces were studied using STEM–HAADF imaging and smooth surfaces with sharp interfaces were observed throughout the structure. Furthermore, high–resolution XRD RSM scans and diffraction patterns showed that the GaN interlayer effectively relaxes the compressive strain from the AlN and enables smooth surface formation for the subsequently grown $Al_xGa_{1-x}N$ layers. The 45–pair AlGaN–based DBR has a peak reflectivity of 95.4% at 368 nm with a bandwidth of 15 nm.

Although the strain management with GaN interlayer brings countless benefits, it also comes with significant trade off. With the achieved high reflectivity from the AlGaN–DBR, a cavity structure was subsequently grown on top of it which consists of AlGaN spacer layers and 5–pair of MQW. Utilizing a quadrupled Nd:YAG laser with $\lambda = 266$ nm for PL measurements, the emission intensity for a MQW grown on the DBR is significantly dimmer than the same MQW grown on a GaN template. A further two–beam dark–field TEM study shown in Fig. 34 by our colleagues at Arizona State University shows a significant density of dislocations were generated at the GaN interlayer due to strong relaxation. What makes the situation worse is these edge–type dislocations didn't stay within in–plane direction, they propagated through the entire DBR structure by zig–zagging through the entire DBR as the thickness of each quarter–wavelength–thick layer isn't thick enough to allow dislocations to coalesce. On the other hand, the work reported by Wang et. al. [69] only has a single thick AlGaN layer which allows dislocations to coalesce and prevent continuing threading up. Adding a thick AlGaN layer on top of the GaN interlayer prior to DBR

growth may be an alternative solution for future study. The other possible solution can be growing three–quarter wavelength thick bilayers instead of quarter wavelength thick to allow dislocations to have a better chance to coalesce.

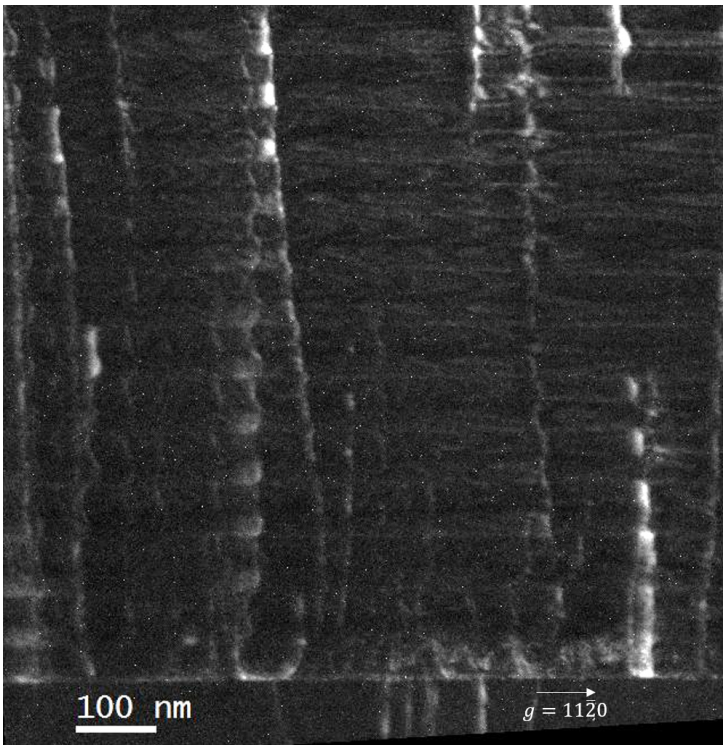

Figure 34: Twp–beam dark–field TEM image at $[1\bar{1}00]$ zone. All the dislocations lines are pure edge–type generated at AlN/GaN interface due to lattice misift.

CHAPTER VI

IMPROVED ELECTRICAL CONDUCTIVITY FOR N–DBR

6.1 Introduction

In the past few years, significant research efforts have been made to develop III–nitride–based VCSELs for numerous applications including, optical fiber data transmission [75–77], optically pumped solid–state lasers [78–80], and chip–scale atomic clocks [81–84]. The crystal quality of the DBRs, which are typically composed of epitaxially grown semiconductor materials, plays a vital role in VCSEL operation as the photon lifetime (τ_p) in the cavity largely depends on the reflectivity of the DBRs [54]. For the III–nitride material system, the growth of high–reflectivity DBR structures is extremely challenging due to the large lattice mismatch between GaN and AlN as well as the relatively low refractive index contrast of the nitride material system as shown in Fig. 35 [63]. In the previous chapter, an electrically conducting n–type DBR consisting of a silicon–doped 40–pair $Al_{0.12}Ga_{0.88}N$/GaN DBR structure was demonstrated. This DBR has a peak reflectivity of 91.6% at 368 nm with a bandwidth of 11 nm. In addition, the 40–pair n–DBR shows the vertical resistance of 5.5 Ω, which corresponds to a bulk resistivity of 0.52 Ω–cm, near the maximum measured current of 100 mA [85]. An electrically conducting III–nitride n–type DBR eliminates the requirement of a lateral n–type contact, which allows larger number of devices per wafer as well as reducing fabrication complexity. However, the non–Ohmic current–voltage (I–V) characteristics measured on the conventional AlGaN–GaN n–DBR is not desirable as it can lead to larger Joule heating, which can limits the optical gain of the active region. In this chapter, we found that the graded n–DBR can transport

carriers more effectively in the vertical path and a comparison study was carried out to understand both optical and electrical characteristics for conventional and graded n–DBR.

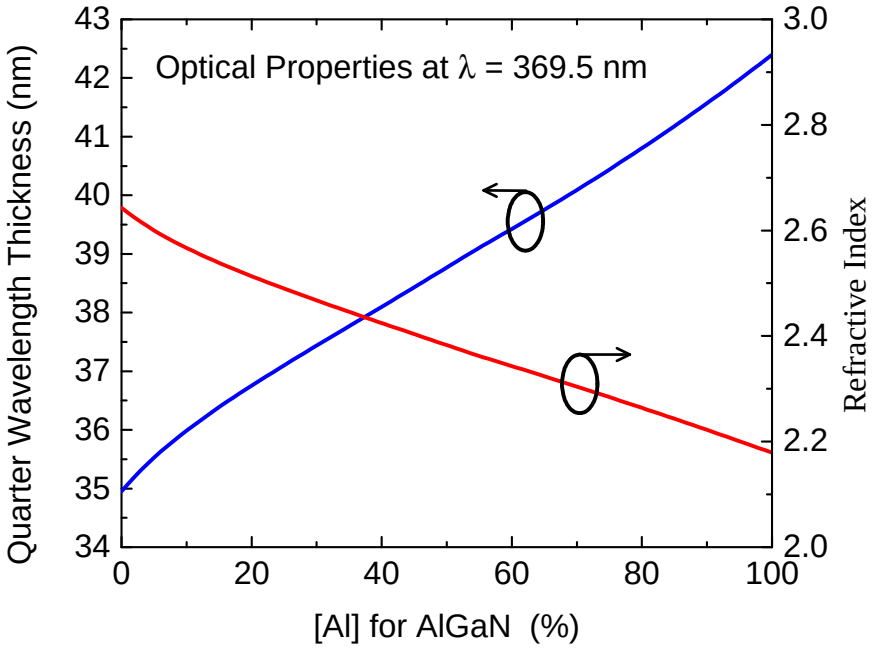

Figure 35: Refractive index of $Al_xGa_{1-x}N$ at 369 nm (red) and the corresponding quarter wavelength thickness (blue). [62]

6.2 Experimental Procedures

To improve the I–V characteristics of the n–DBR, the previously reported 40–pair silicon–doped $Al_{0.12}Ga_{0.88}N$/GaN DBR was modified to a 40–pair silicon–doped graded $Al_xGa_{1-x}N$ DBR with x continuously varied from 0 to 0.12 and 0.12 to 0 as the bilayers. The changes in n–DBR structure reduces the thickness of high aluminum mole fraction material as well as redistribute the polarization charge for favoring electrical characteristics. The epitaxial growth on (0001) sapphire substrate was performed in

a Thomas–Swan (now AIXTRON) 6 × 2" close–coupled showerhead MOCVD reactor system. Epipure® trimethylaluminum ($Al(CH_3)_3$, TMAl) and trimethylgallium ($Ga(CH_3)_3$, TMGa) from SAFC were used for group III precursors while ammonia (NH_3) from Matheson Tri–Gas® was used for the group V precursor. The n–type conductivity of the material was realized by including silane (SiH_4) as dopant source during the DBR structure growth. The growth started with a ~ 3.5 μm silicon–doped GaN template which was prepared by a three–step growth process described in the previous chapter. Then the growth continued with a graded $Al_xGa_{1-x}N$ DBR structure. The graded structure was realized by modulating the TMAl flow rate while maintaining a fixed TMGa and NH_3 flow rate throughout the DBR growth. The entire graded n–DBR structure was grown in a H_2 ambient and the growth pressure and temperature were kept at constant 200 Torr and ~ 1060 °C, respectively. To establish a fair comparison between the conventional and the graded–composition $Al_xGa_{1-x}N$ n–DBRs, the source molar flow rates of the dopant for both cases were carefully controlled such that the free carrier concentration was maintained at 1×10^{18} cm^{-3} for the entire n–DBR structure while that for the n–GaN template was estimated to be 4×10^{18} cm^{-3}.

Following the epitaxial growth, the wafer was fabricated by Dr. Kao for vertical current conductivity characterization. First, a ~ 3 μm deep mesa was created to expose the n–GaN layer below the DBR using inductively–coupled plasma reactive–ion etching (ICP–RIE). After the mesa etching, the exposed mesa surface was treated in a diluted KOH–based solution under ultraviolet light illumination to remove the dry–etching–induced surface damage. Finally, a Ti/Al/Ti/Au metal stack was used as n–type ohmic contacts on the top and the bottom of 60 μm diameter circular mesas followed by a thermal annealing performed in a N_2 ambient. The transmission line measurement (TLM) data for the case of the graded n–DBR is shown in Fig. 36. The corresponding sheet resistance was calculated to be 13 Ω/sq while the

contact resistance was calculated to be 1.2×10^{-5} Ω–cm^2 for the bottom contact. On the other hand, the top contact has sheet resistance of 9.8 Ω/sq and a contact resistance of 9.8×10^{-6} Ω–cm^2. As pointed out earlier, to establish a fair comparison in the electrical properties between the conventional and the graded n–DBR, all the fabrication processes were performed in the same batch to minimize the variations.

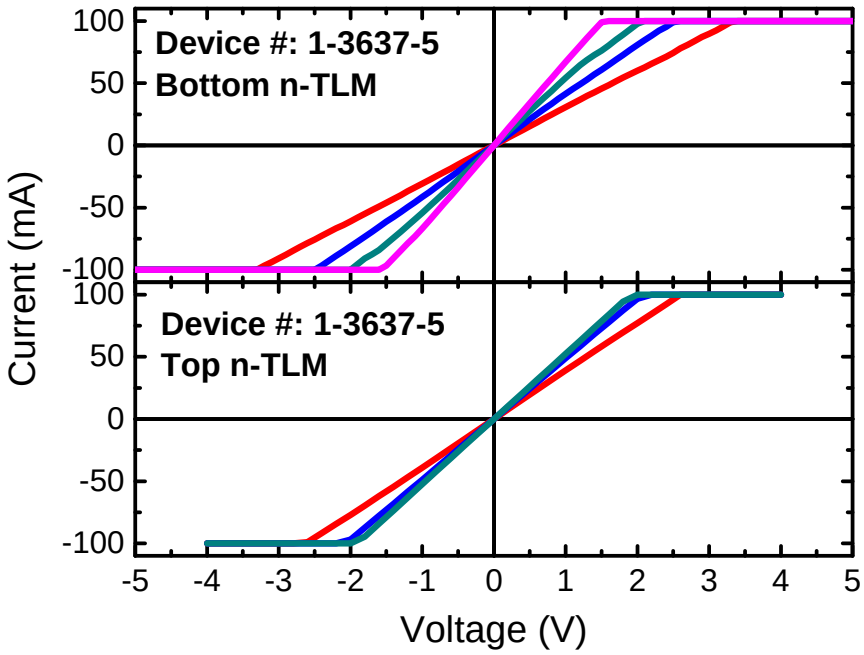

Figure 36: TLM measurement for top and bottom metal contact consists of Ti/Al/ Ti/Au. (Credit to Dr. Kao)

6.3 Results and Discussion

Since the previous chapter presented a thorough analysis of a conventional $Al_xGa_{1-x}N/Al_yGa_{1-y}N$ n–DBR, this section will first present the material characterization of the graded n–DBR followed by a comparison of the electrical properties. Figure 37 shows the cross–sectional high-angle–annular dark-field imaging (HAADF)

image of the DBR acquired by Dr. Xie and Mr. Wang at Arizona State University. As discussed earlier, HAADF technique is very sensitive to the projected Z number, which makes the contrast brighter in the thicker region of the sample as shown in the Fig. 37 (a) near the n–GaN template layer (closer to the bottom of the image). From the capture image, all the 40–pairs of graded $Al_xGa_{1-x}N$ DBR

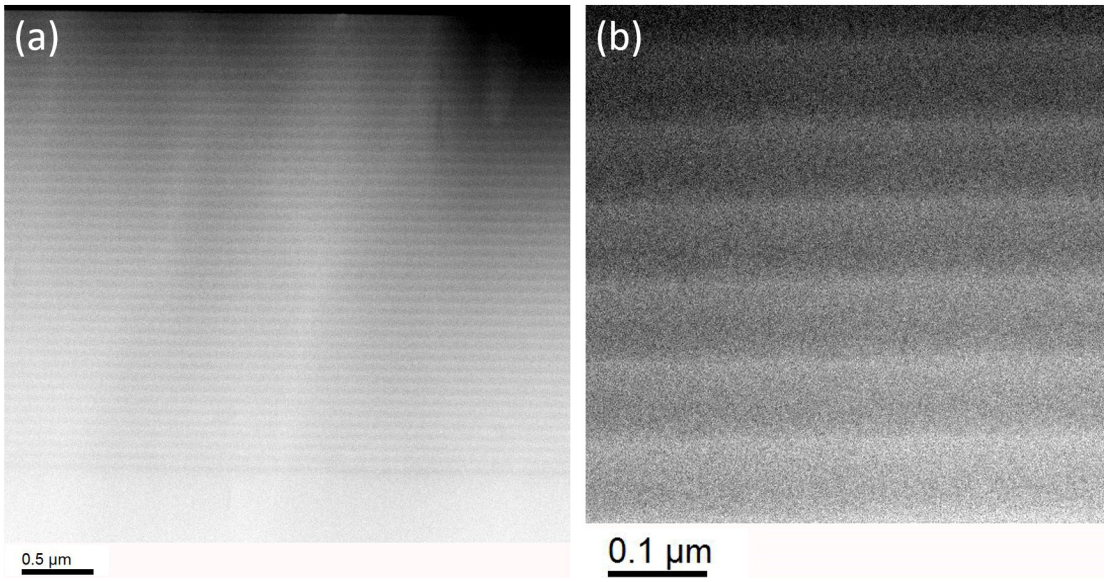

Figure 37: All the 40–pairs of the graded $Al_xGa_{1-x}N$ DBR structure were clearly observed in the HAADF image as shown in (a) and the zoom–in image can be found in (b). (Credit to Dr. Xie and Mr. Wang)

structure were clearly observed while the interfaces didn't appear as sharp as for the previous conventional n–DBR due to the continuously graded interfaces. A higher magnification image of the graded n–DBR structure is shown in Fig. 37 (b). This

image has a similar scale to the previous conventional n–DBR TEM image, and we can conclude that the bilayer structure is clearly gone and the contrast is continuously varying along the growth direction.

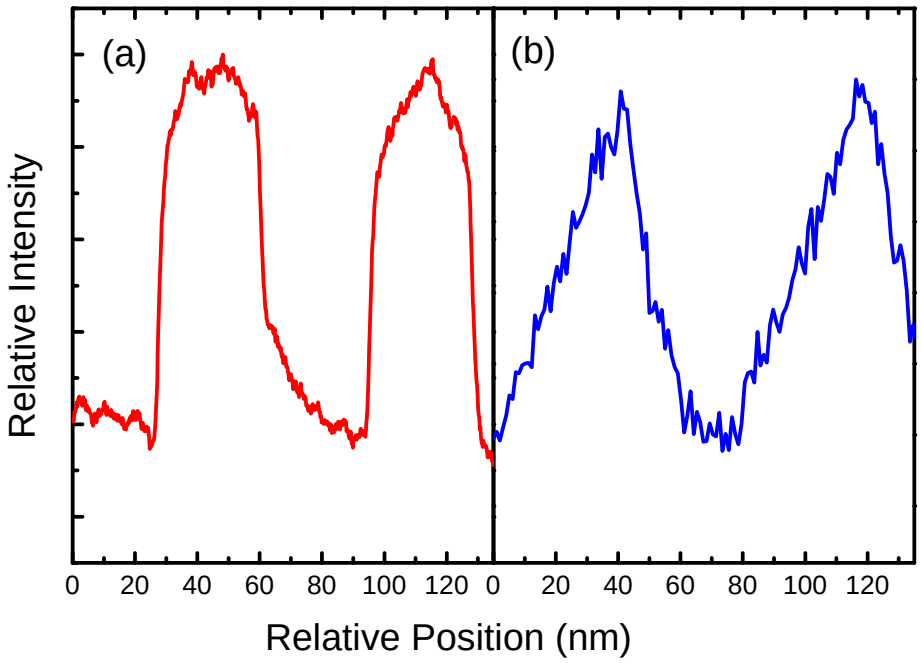

Figure 38: HAADF intensity profile for (a) conventional n–DBR and (b) graded n–DBR.

For a more quantitative analysis, normalized HAADF intensity profiles for conventional and graded n–DBRs are shown in Fig. 38 (a) and (b), respectively. The vertical scale (y–axis) is the relative intensity of the TEM image using line scan analysis with corrections for thickness effects; the horizontal scale (x–axis) shows the relative position along the growth axis (c–axis). The brighter position in relative intensity profile indicates to higher GaN mole fraction while lower intensity corresponds to higher AlN mole fraction in the $Al_xGa_{1-x}N$ alloy. The data of Fig. 38 (a) clearly demonstrates the thickness of each of the layers in the DBR have roughly a quarter–wavelength thickness while the composition profile can be roughly approximated as

a square wave. On the other hand, the HAADF data of Fig. 38 (b) shows that a half–period of the DBR has an average layer which is a quarter–wavelength thick of the graded AlGaN as intentionally designed. Furthermore, a distinctively different alloy composition profile was observed as Fig. 38(b) which can be approximated as a triangle wave profile instead of the square wave shown in Fig. 38 (a).

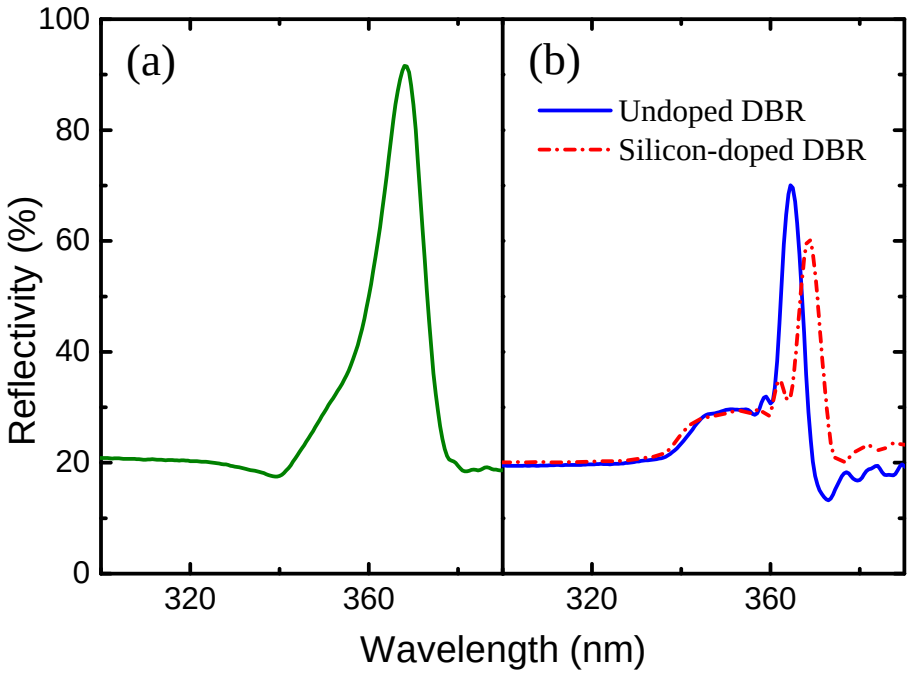

Figure 39: Optical reflectivity spectra for 40–pair DBR with (a) conventional silicon–doped structure and (b) graded $Al_xGa_{1-x}N$ with undoped (blue solid line) as well as silicon–doped (red dash dot curve) structure.

Next, the optical reflectivity of the DBR samples were examined at 300K using a Shimadzu UV2401PC ultraviolet–visible spectrometer. The same measurement conditions as were used for the previous conventional n–DBR were also used for the graded DBR. A halogen lamp was used for obtaining the reflectivity above 283 nm while the deuterium lamp was used for the reflectivity between 200 to 283 nm and the measurement step was 0.5 nm. Shown in Fig. 39 (a) is the reflectivity

spectra of the 40–pair conventional n–type AlGaN/GaN DBR while Fig. 39 (b) illustrates the reflectivity spectra for the graded silicon–doped (dash dot red curve) and undoped (solid blue) graded $Al_xGa_{1-x}N$ DBR structures. As mentioned earlier, the conventional n–DBR demonstrated a peak reflectivity of 91.6% at 368 nm with a bandwidth of 11 nm. On the other hand, the 40–pair undoped graded $Al_xGa_{1-x}N$ DBR exhibits a peak reflectivity of 70 % at 364.5 nm with a bandwidth of $\sim$ 5.5 nm while the peak reflectivity of silicon–doped graded $Al_xGa_{1-x}N$ DBR was measured to be 60.5 % at 368.5 nm with a bandwidth of $\sim$ 5.5 nm. Since the center wavelength for the reflectivity spectra from both DBRs are reasonably close, a direct comparison between the DBRs can be made without factoring in the differences in absorption. It was clear that the conventional AlGaN n–DBR demonstrates far superior optical reflectivity properties (in both peak reflectivity and bandwidth) than the graded $Al_xGa_{1-x}N$ n–DBR and this result is consistent with the work reported by Brummer et al. [86] Aside from the reduction of reflectivity originating from the differences in the DBR structure, a further reduction of the reflectivity from the graded silicon-doped $Al_xGa_{1-x}N$ DBR may attributed to the larger excitonic absorption introduced by the Si doping [64].

To study the origin of the reflectivity differences between the 40–pair silicon–doped and undoped $Al_xGa_{1-x}N$ DBR, AFM measurements were carried out to ensure the excitonic subbandgap absorption is mainly responsible for this difference. Presented in Fig. 40 is the surface morphology of 40–pair silicon–doped graded $Al_xGa_{1-x}N$ n–DBR grown on (0001) sapphire substrate. Even with n–type silicon doping and the tensile strain experienced throughout the n–DBR structure, smooth surface formation with terraced step-flow, characteristic of two–dimensional (2D) layer–by–layer III–nitride epitaxial growth, is observed. The root–mean–square roughness is 0.25 nm, 0.45 nm, 0.94 nm for 1×1 μm^2, 5×5 μm^2, and 20×20 μm^2 measurements, respectively. With the obtained root–mean–square roughness from the wafer surface, the effect

of the surface roughness on the reflectivity of material can be obtained through the Nevot–Corce factor based on Eq. 40. Comparing the surface roughness of the 40–pair silicon–doped $Al_xGa_{1-x}N$ DBR and the conventional n–DBR, the differences in surface morphology of two n–DBRs cannot be responsible for such dramatic change in the reflectivity of the graded n–DBR; thus, the main reflectivity differences can be attributed to the larger excitonic sub–bandgap absorption.

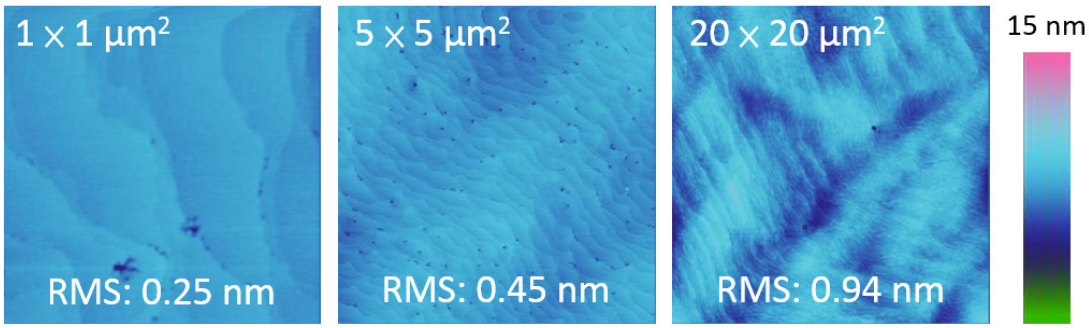

Figure 40: Atomic–force microscopy measurements of the 40–pair silicon doped graded $Al_xGa_{1-x}N$ DBR structure with x vary from 0 to 0.12 on silicon doped n–GaN template taken at 1×1 μm^2, 5×5 μm^2, and 20×20 μm^2 and the corresponding root–mean–square roughness is 0.25 nm, 0.45 nm, 0.94 nm, respectively.

Illustrated in Fig. 41 are the I–V characteristics of the conventional and graded n–DBR measured at room temperature under DC measurement conditions. The measurements were terminated at the maximum measured current of 100 mA and a very distinctive I–V relation was observed from the two n–DBRs. The conventional n–DBR shows a dynamic resistance throughout the measurement range. On the other hand, a completely different behavior was observed from the graded n–DBR as it demonstrates a constant resistance throughout the measurement range. The origin of this phenomenon can be explained by the differences in dominant carrier transport mechanisms. In the case of the conventional n–DBR, the abrupt hetero–interfaces

formed potential barriers due to the conduction band offsets between $Al_{0.12}Ga_{0.88}N$ and GaN which limit the dominant carrier transport mechanism to thermionic emission. In the case of thermionic emission, the current density can be formulated as (by neglecting the actual shape of potential barrier for simplification):

$$J_{TE} = A^* T^2 e^{-\phi_B/V_t} \left(e^{V_a/V_t} - 1\right) \tag{44}$$

where A^* is Richardson constant, T is temperature, ϕ_B is potential barrier height, V_a is applied bias, and V_T refers to thermal energy. The Richardson constant is give by:

$$A^* = \frac{4\pi q m^* k^2}{h^3} \tag{45}$$

with h as Planck constant, k as Boltzmann constant, m^* as effective mass of carrier, and q is fundamental charge. On the other hand, the thermal energy V_T can be described as $V_T = kT/q$. Based on the thermionic emission current density equation, we can clearly see that the current increases exponentially with an increase in the applied bias. However, under negative bias, the current didn't collapse as predicted by the equation. Instead, it was exhibiting an exponential behavior as well and this is because the structure is symmetric; therefore, the final I–V characteristics is the sum of two thermionic emission characteristics with opposite current flow direction.

On the other hand, the graded n–DBR doesn't have such potential barriers as experienced in the conventional n–DBR. As a result, the dominant carrier transport mechanism is now drift–diffusion and the corresponding current density equation is formulated as (in the case of our n–type material):

$$J_{drift-diff} = q\mu_n nE + qD_n \nabla n \tag{46}$$

where μ_n is carrier mobility (electron in this case), n is free carrier concentration, and D_n is diffusion constant. For both drift and diffusion components, the equation clearly shows the linear behavior is expected given the drift component is linearly

proportional to electric field while the diffusion component is linearly proportional to the gradient of the carrier distribution.

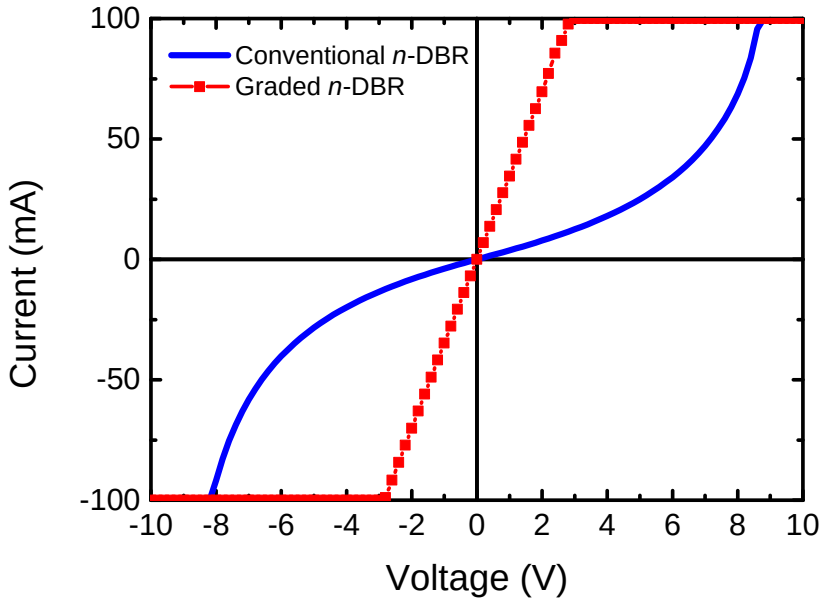

Figure 41: I–V characteristic of the 40–pair silicon doped $Al_{0.12}Ga_{0.88}N$/GaN and graded $Al_xGa_{1-x}N$ DBR structures on silicon doped n–GaN templates under DC measurement conditions at room temperature. The graded $Al_xGa_{1-x}N$ n–DBR demonstrated a constant resistance while the conventional $Al_{0.12}Ga_{0.88}N$/GaN n–DBR demonstrated a dynamic resistance.

By further analyzing the graded n–DBR, the series resistance can be determined to be 25 Ω. To extract the vertical resistance through the graded n–DBR from the measured series resistance, the previously performed TLM measurements by Dr. Kao on the top and bottom of the mesa can be used to calculate the contact resistances and the sheet resistances of the material. The two contact resistances and the lateral resistance on the bottom of the mesa were determined to be 0.46, 0.45, and 3.5 Ω, respectively. By subtracting contact and lateral resistances from the measured series resistance, the vertical resistance through the graded n–DBR structure can be

determined as 20.6 Ω, which corresponds to the bulk resistivity of 1.45 Ω–cm.

6.4 Summary

In summary, an improved in electrical conductivity was demonstrated by using graded $Al_xGa_{1-x}N$ layers to form the n–DBR instead of the conventional n–DBR structure. A clear advantage of using the graded n–DBR was observed from the I–V characteristics as the vertical resistance through the n–DBR is lower and is a constant while the conventional n–DBR demonstrated a larger and dynamic resistance. The static resistance from the graded n–DBR is particularly beneficial if the device is designed to have back–side n–contact instead of lateral n–contact. This observed phenomenon of differences in I–V characteristics originated from the differences in carrier transport mechanism and can be explained by the carrier transport equations. However, using graded n–DBR comes with the trade–off of the maximum optical reflectivity due to the excitonic sub–bandgap absorption loss which is detrimental to the optical reflectivity. As a result, the proper choice of material compositions for a given wavelength is the key to utilize the n–type DBR for III–N VCSELs.

CHAPTER VII

OPTICALLY PUMPED UV VCSEL WITH N–DBR

7.1 Introduction

Since the first demonstration of VCSELs by Soda, et al.[9], numerous applications have replaced edge–emitting lasers with VCSELs owing to the advantages of lower threshold current operation, circular and low–divergence output beam, and lower temperature sensitivity compared to edge–emitting laser diodes. With the advancement in technology, several research teams demonstrated current–injection III–N-based VCSELs with either a hybrid–mirror structure [14, 66] or double–sided dielectric DBR structure[10, 87], laser operation in sub–400 nm regime has rarely been reported.[13] Even under the optical pumping excitation scheme, there are only few VCSELs with operating peak wavelengths in the sub–400 nm region. [88, 89] This is primarily due to the fact that the threshold power for laser action increases as the lasing wavelength decreases since the rate of spontaneous emission increases as $1/\lambda^3$. Another limiting factor for realizing ultraviolet III–N VCSELs is having limited choices for optically transparent materials with large refractive index contrast for DBR formation and optical cavity formation which inevitably increases threshold current density. In this chapter, one of the previously developed III–N based DBRs [67] as summarized in chapter IV, V, and VI will be utilized for realizing an optically pumped ultraviolet VCSEL near our targeted wavelength of $\lambda = 369.5$ nm.

To down–select the DBR that has highest chance in fabricating an optically pumped VCSEL, the pros and cons for each DBRs will be carefully analyzed and the summary of the DBR characteristics can be found in table 7. Although the 45–pair undoped $Al_{0.3}Ga_{0.7}N/Al_{0.04}Ga_{0.96}N$ DBR provides the highest reflectivity among

all of the DBRs studied in this work, the dislocations generated at the interface of the GaN interlayer and the AlN template significantly degrade the quantum efficiency of MQW structure. While we pointed out earlier that the material quality can be potentially restored by forcing dislocations to annihilate within a thick AlGaN layer prior to the DBR growth, experimental verification is still required and the required total epitaxial thickness will increase significantly. Furthermore, utilizing a GaN interlayer on an AlN substrate prohibits us from gaining the benefit of a low dislocation native substrate which ultimately limits the potential in achieving even better lasers. As a result, a 40–pair n–type $Al_{0.12}Ga_{0.88}N$/GaN is chosen for this part of the study given it has the second highest reflectivity with relatively high vertical conductivity. One of the advantages of employing an electrically conducting DBR structure is to eliminate the requirement for lateral contacts, which inevitably reduces the number of devices per wafer as well as deducing the fabrication complexity. However, the n–DBR also introduces higher absorption due to excitonic absorption near the GaN bandgap [64] and limits the achievable optical reflectivity and thus increases threshold pumping power density. In this chapter, an optically pumped VCSEL operating at $\lambda = 374.9$ nm with a hybrid mirror structure and an effective 8λ–thick optical cavity will be presented.

7.2 Experimental Procedures

The epitaxial growth was performed in a Thomas–Swan (AIXTRON) 6 × 2" close–coupled showerhead MOCVD reactor system. EpiPure® trimethylaluminum ($Al(CH_3)_3$, TMAl), trimethylgallium ($Ga(CH_3)_3$, TMGa), and trimethylindium ($In(CH_3)_3$, TMIn) were used for group III precursors while ammonia (NH_3) was used for the group V precursor. To obtain n–type electrical conduction properties for the n–DBR, silane (SiH_4) was used as n–type dopant source. Upon the completion of the last n–DBR layer as mentioned in chapter IV, the growth was then continued to complete the

Table 7: Summary of the III–N based DBR in this work.

DBR Description	Center Wavelength (nm)	Peak Reflectivity (%)	Stopband (nm)	Bulk Resistivity (Ω cm)
40–pair n–type $Al_{0.12}Ga_{0.88}N/GaN$	368	91.6	11	0.52*
45–pair undoped $Al_{0.3}Ga_{0.7}N/\ Al_{0.04}Ga_{0.96}N$	368	95.4	15	–
40–pair undoped $Al_xGa_{1-x}N$ $(x : 0 \leftrightarrow 0.12)$	364.5	70	5.5	–
40–pair n–type $Al_xGa_{1-x}N$ $(x : 0 \leftrightarrow 0.12)$	368.5	60.5	5.5	1.45†

*dynamic resistance; †static resistance

optically pumped VCSEL cavity. Although the epitaxial structure employed in this work was designed for an optical pumping experiment, the structure was also capable of realizing an electrical injection surface–emitting device by introducing doping in both spacer layers. Described in Fig. 42 is the schematic cross–section view of the structure. The active region consisted of a five–pair InGaN/AlGaN MQW structure with well and barrier thicknesses of 3 nm and 5 nm, respectively. To form an indium containing III–N layer, the growth chamber is required to operate in N_2 ambient instead of normal H_2 ambient growth condition. As a result, the entire active region was grown under N_2 ambient to avoid a large thermal stress exerted on the epitaxial structure as well as avoiding indium desorption. The mole fraction of indium in the InGaN ternary alloy largely depends on the growth temperature of the layer. In this work, the quantum wells were grown at a growth temperature of $\sim$ 850 °C. On the other hand, the quantum barrier was grown at $\sim$ 950 °C to ensure the best achievable AlGaN material quality before the indium desorption from the InGaN quantum well

occurs. The active region was sandwiched by two 120 nm $Al_{0.06}Ga_{0.94}N$ spacer layers to form a physical thickness corresponding to a 2λ optical cavity for the VCSEL structure. To complete the VCSEL structure, SiO_2 and HfO_2 were selected to form a top dielectric DBR due to the fact that SiO_2 and HfO_2 are both optically transparent as well as having a large refractive index contrast between the two materials (SiO_2: n $\sim$ 1.47, HfO_2: n $\sim$ 2.17) near the UV operating wavelength. In the previous work, a similar SiO_2/HfO_2 DBR was proven to be effective for a UV DBR as six–pairs of SiO_2/HfO_2 can achieve a reflectivity of 97% at 249.5 nm [90]. In this work, the dielectric DBR formation utilizing e–beam evaporator was performed by Mr. Haq.

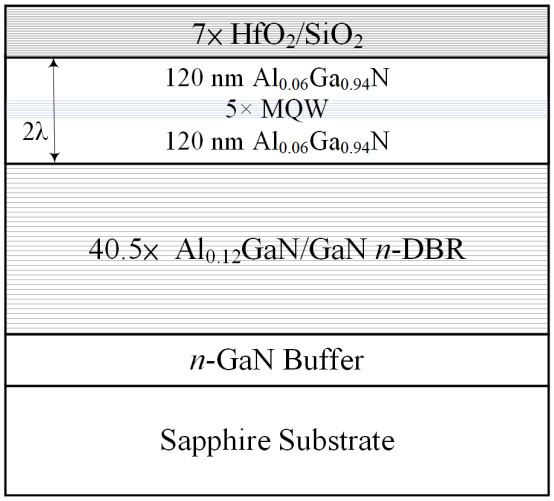

Figure 42: Cross–section schematic diagram of the optically pumped VCSEL structure.

To ensure that the active region was aligned to the optical mode for maximizing the confinement factor (Γ), numerical simulations for the optical mode distribution were studied and the simulations were performed by Mr. Mehta. Figure 43 shows the refractive index profile as well as the optical intensity profile with an inset figure showing the optical intensity distribution near the active region. Several standing–wave patterns were formed within the cavity and the third quantum well was perfectly

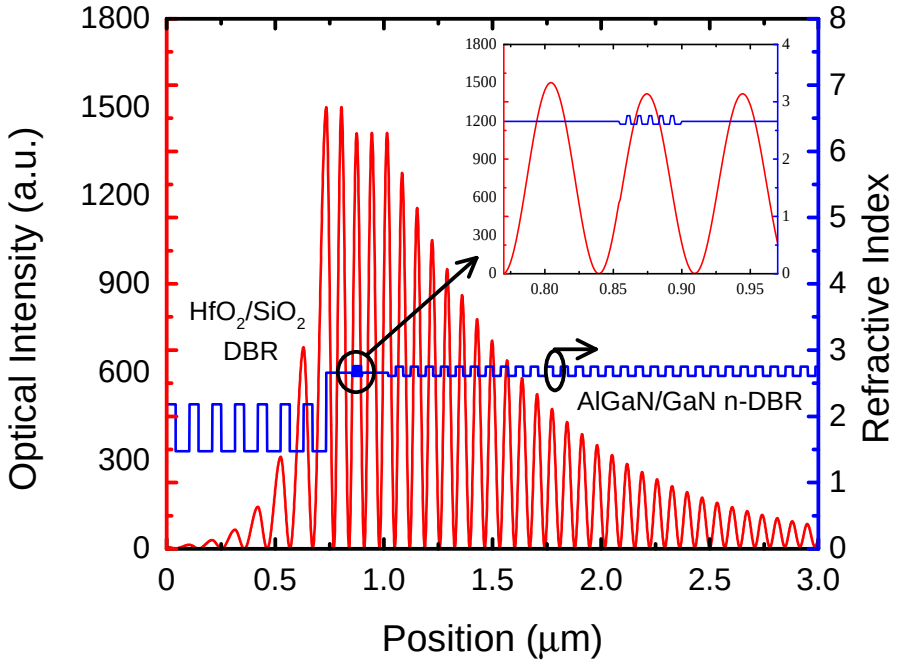

Figure 43: Refractive index profiles and simulated optical field distribution within the laser structure. (Credit to Mr. Mehta)

aligned to the peak of optical mode, which suggests that the maximum Γ of 2.2% was achieved from the given epitaxial structure. Since the emission wavelength of a VCSEL is defined in part by the cavity length, it is important to include the penetration depths ($1/e$ decay) of the optical mode into both the top and bottom DBRs. Due to lower reflectivity per pair from the semiconductor DBR, the optical field had a significantly longer penetration depth compared to the dielectric DBR as described in Fig. 43. After including both of the penetration depths as well as the physical thickness of the cavity, the overall effective cavity thickness was calculated to be $\sim$1.13 μm or an $\sim 8\lambda$–thick cavity. The effective cavity length is significantly more important than the physical cavity length as it determines the lasing condition as well as Q–factor of the cavity. To form a microcavity light–emitting diode (MCLED) ,

AlGaN layers need to be doped for proper electrical conductivity, and a more complex fabrication process is required including a current–restricting aperture defined by ion–implantation as well as ohmic contacts formation.

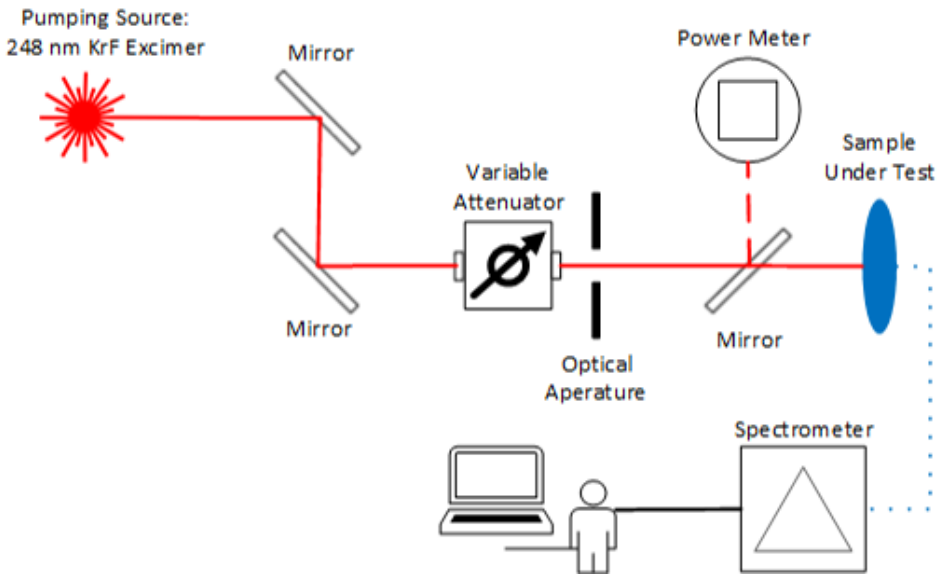

Figure 44: Schematic diagram of optical pumping measurement system.

The optically pumped laser experiments were performed using a Coherent COMPexPro excimer laser system operating with a pulse width of 20 ns at a repetition rate of 10 Hz. The laser system used in this work was originally configured for ArF ($\lambda = 193$ nm or $h\nu = 6.4$ eV) instead of KrF ($\lambda = 248$ nm or $h\nu = 5$ eV). As a result, the rear high reflector and the output coupler attached on the laser tube have peak reflectivity near 193 nm instead of 248 nm. Since KrF provides the largest optical gain in fluoride–base excimer laser family, the lasing condition can still be established with the ArF optics set, but the peak power was significantly reduced from highest achievable 400 mJ down to $\sim$ 110 mJ. The pump laser beam first passed through an optical aperture with a width of 0.1 cm and length of 1.27 cm and was then incident

on the surface of the dielectric DBR. To maximize the transmission of the pump laser, the incident beam was aligned perpendicular to the wafer surface. Optical attenuators were inserted to vary the optical pump power for measuring the optical output power as a function of excitation density (L–L curve). An optical fiber was placed in the proximity of the sapphire substrate (i.e., the unpolished back side of the wafer) for spontaneous and stimulated light–emission detection (as shown in Fig. 44). The photon emission was collected and analyzed using an Ocean Optics Maya 2000 Pro spectrometer with a spectral resolution of 0.2 nm. In order to obtain the polarization of the VCSEL emission, a Glan–Laser α–BBO polarizer with 100,000:1 extinction ratio was inserted between the sample and the optical fiber.

To visualize how the cavity mode can affect the laser characteristics, a variant of the structure was grown as a comparison. Instead of using $Al_{0.06}Ga_{0.94}N$ for spacing layers as described in Fig. 42, the aluminum mole fraction was increased to $Al_{0.12}Ga_{0.88}N$ for both sides of the spacing layers. By increasing in the aluminum mole fraction, the cavity mode will shift since the original longitudinal mode no longer has good overlap with the gain spectrum. As a result, the observed cavity mode will emerge with a different peak wavelength.

7.3 Results and Discussion

Following the growth, an optical reflectivity measurement was performed as illustrated in Fig. 45 with the blue curve showing the reflectivity spectrum before the dielectric DBR deposition. Due to the lack of the top DBR for this particular reflectivity measurement, the cavity resonance is limited and thus the cavity mode is difficult to observe. The absorption of the five-pair MQW was clearly shown as the optical reflectivity dropped significantly near 360 nm compared to the DBR reflectivity spectrum without the VCSEL cavity. As mentioned earlier, the asymmetry of the reflectivity spectrum of the bottom DBR is typically centered near 370 nm [67].

Although the epitaxially grown structure prohibited us from measuring the reflectivity directly, the center wavelength of the reflectivity spectrum is expected to be well–aligned to the cavity mode based on the presented reflectivity spectrum. Next, the seven–pair HfO_2/SiO_2 dielectric DBR was deposited on the wafer via e–beam evaporation to form the full VCSEL structure. The reflectivity of the dielectric DBR was characterized from the companion glass slide in the same DBR evaporation run. The seven–pair dielectric DBR had a reflectivity center wavelength of 369 nm with peak reflectivity of 92.4%. Due to the large index contrast between HfO_2 and SiO_2, the stopband of the DBR was determined to be $\sim$ 60 nm. The red–triangle curve described in Fig. 45 describes the reflectivity spectrum from the full VCSEL structure. The optical cavity mode was clearly observed near $\sim$ 370 nm from the full VCSEL structure reflectivity spectrum.

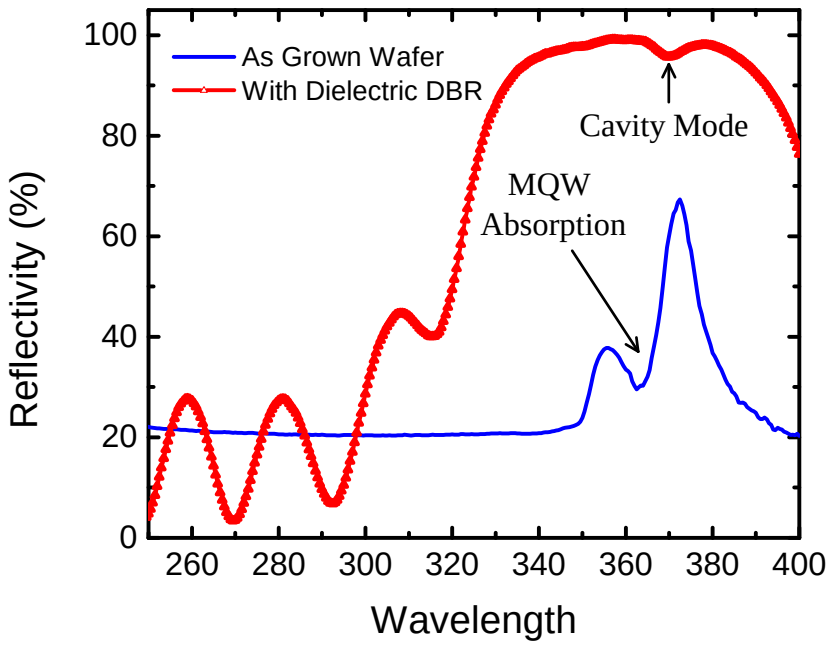

Figure 45: Optical reflectivity from the as grown wafer (blue curve) and after dielectric DBR formation (red–triangle curve).

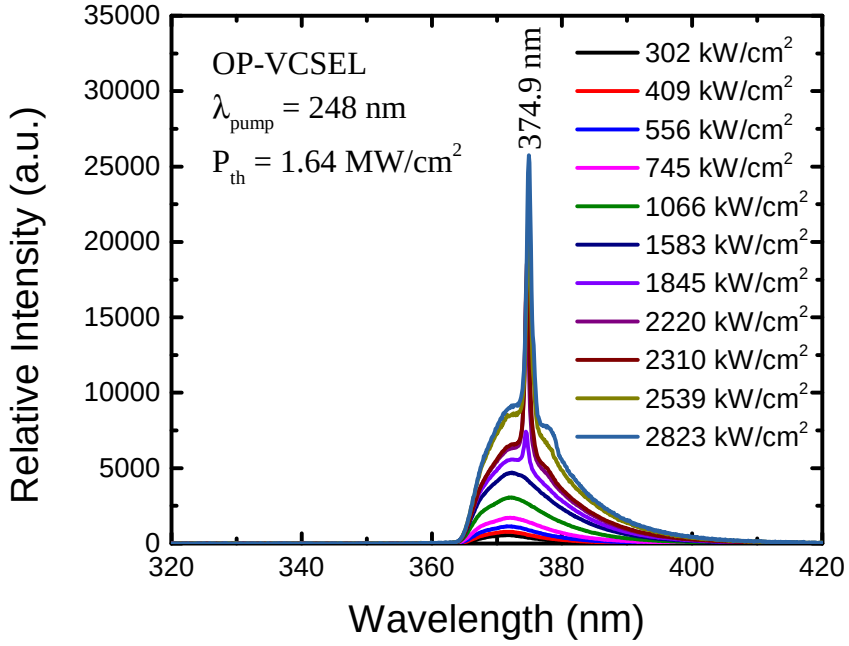

Figure 46: Laser emission spectra with pump power densities below and above threshold at room–temperature.

The optical emission spectra collected at room–temperature under various pumping power densities are shown in Fig. 46. The optical peak emission wavelength was determined to be $\lambda = 374.9$ nm with the spectral linewidth recorded as 0.66 nm (extracted via curve fitting) at the maximum measured optical pump–power of 2.82 MW/cm^2. A significant change in emission spectra was observed as the pumping power density increased above ~ 1.8 MW/cm^2 with a rapid narrowing feature near λ 375 nm. As the pumping power density further increase from ~ 1.8 MW/cm^2 to the highest measured power of ~ 2.8 MW/cm^2, a slight red shift of less than ~ 0.5 nm was observed. In addition to the narrow feature observed from the emission spectra, the remaining emission feature consists of a relatively broadband (as compared to the laser emission) spectra which directly related to the cavity mode as the peak emission perfectly aligned with the cavity mode observed from the reflectivity spectrum

as presented in Fig. 45.

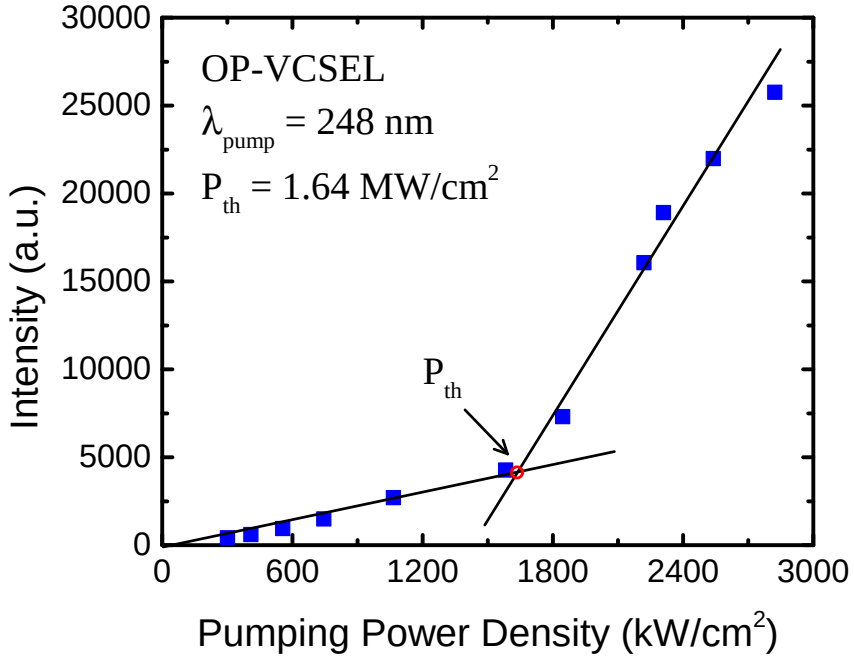

Figure 47: Light–output intensity as a function of the optical pump power density at room–temperature with lasing at $\lambda = 374.5$ nm.

Using measured emission spectra under various pumping power densities at 300 K, the optical output power as a function of excitation density (L–L curve) can be extracted as shown in Fig. 47. For the determination of the L–L curve the integration of the entire spectrum was not performed due to the fact that the spontaneous portion of the emission was amplified and the effect of the amplified spontaneous emission (ASE) will dominate and the true characteristics of the stimulated emission in the laser can be difficult to understand. To mitigate this issue, a different calculation approach was adopted. Due to the fact that laser emission typically exhibits a Lorentz lineshape and the integrated intensity for a given Lorentz function can be calculated

with a simple equation:

$$\int_{-\infty}^{\infty} L(\lambda)d\lambda = \int_{-\infty}^{\infty} \frac{A}{\pi} \frac{\frac{1}{2}w}{(\lambda - \lambda_0)^2 + \left(\frac{1}{2}w\right)^2} = \frac{1}{2}wA\pi \tag{47}$$

where A is peak intensity, λ_0 is peak emission wavelength, and w is the linewidth of the emission spectrum. As a result, the output power of the laser as a function of pumping power density can be estimated based on the the peak intensity of the laser emission as shown in Fig. 47. The L–L curve demonstrates a distinct stimulated emission threshold characteristic at a threshold pump power density (P_{th}) of 1.62 MW/cm^2.

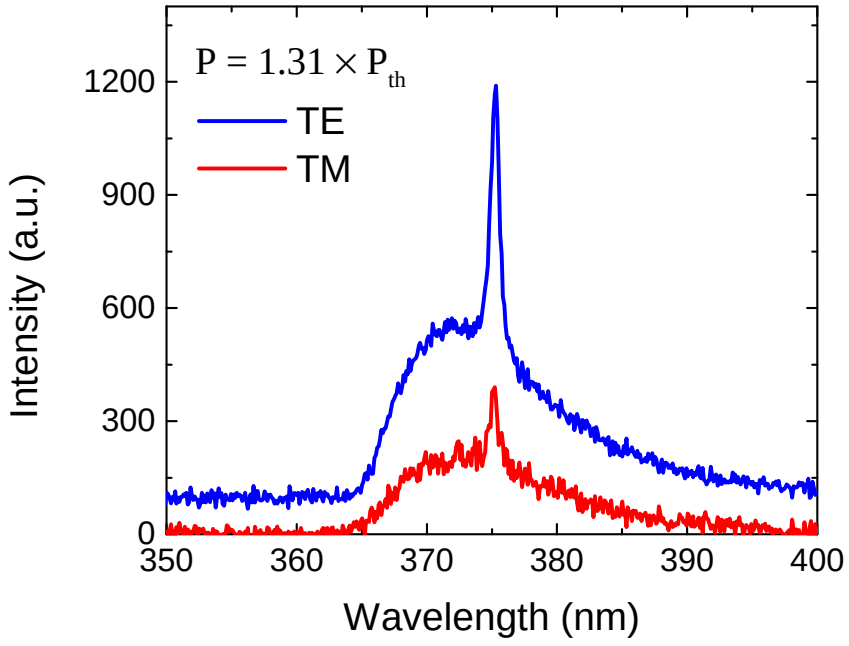

Figure 48: Optical emission spectra for both TE and TM polarizations recorded at room–temperature above threshold power density. An offset was applied to the TE emission spectra for visual clarity.

Emission spectra for transverse electric (TE) and transverse magnetic (TM) orientations are shown in Fig. 48 for the optically pumped VCSEL operating above

the threshold power density. Stimulated emission from the structure demonstrated strong TE polarized with degree of polarization (P) defined as

$$P = \frac{I_{TE} - I_{TM}}{I_{TE} + I_{TM}} = 64\% \tag{48}$$

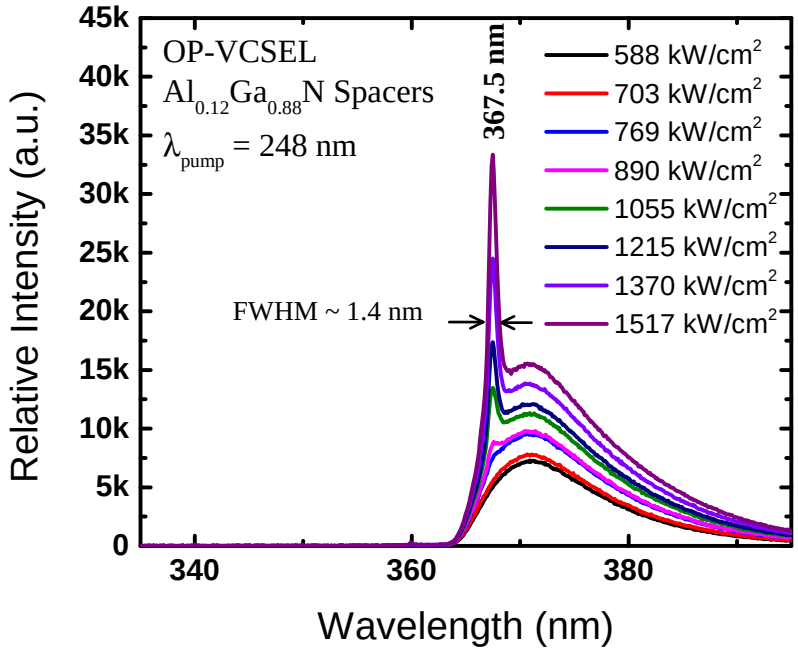

Figure 49: Optically pumped laser emission spectra with pump power densities below and above threshold at room–temperature. The spacer layers used in this case is $Al_{0.12}Ga_{0.88}N$.

For III–nitride material system, the emission polarization is typically TE dominated due to the fact that the band–to–band transition is typically dominated by conduction band to heavy hole (HH) band recombination instead of the crystal–field–split–off hole band. With the more probable transition from conduction to HH band, InGaN/AlGaN MQWs emitting near $\lambda = 375$ nm will have higher optical gain in the TE mode. Unlike edge–emitting lasers, VCSELs emit relatively strong TM polarized light and this is due to the fact that VCSELs are allowed to have both orthogonal

polarization states coexisting. In addition, the orthogonal polarization states cannot only co–exist but also the dominating state can be interchangeable.

Described in Fig. 49 is an optically pumped VCSEL emission spectra collected at room–temperature at various pumping power densities. The epitaxial structure is similar to the schematics diagram shown in Fig. 42, but with $Al_{0.12}Ga_{0.88}N$ spacer layers instead of $Al_{0.06}Ga_{0.94}N$ layers. Comparing the two emission spectra from Fig. 46 and Fig. 49, the spontaneous emission spectra under low pumping power density is nearly identical and this is due to the identical optical gain spectra from the identical active region structure. By increasing the pumping power density, the lasing peak wavelength was very different and an ~ 7 nm "blue–shift" was observed. This is because differences in the longitudinal mode alignment originated from the different AlGaN compositions of the spacer layer. Given the short–cavity nature of the VCSEL, the longitudinal modes were widely spread out as the mode spacings can be calculated as $\Delta\nu = c/(2nL)$. On the other hand, the edge–emitting lasers have very closely packed longitudinal modes given the fact that the cavity length is significantly longer by few orders of magnitude. This set of experiments provides clear evidence that the observed laser action was vertically confined due to the significant shift in the observed lasing peak wavelength and the details of the mode structure.

7.4 Summary

In summary, an optically pumped III–N UV VCSEL with an effective 8λ–thick cavity grown on an n–GaN template on sapphire substrates by MOCVD was demonstrated. The hybrid–mirror VCSEL employed a seven–pair HfO_2/SiO_2 dielectric stack as the top DBR while the bottom DBR was formed by forty–pair $Al_{0.12}Ga_{0.88}N$/GaN electrically conducting n–DBR. The peak emission wavelength of the VCSEL was $\lambda = 374.9$ nm with a threshold pumping power density of 1.62 MW/cm^2. The numerical simulations demonstrated that the epitaxial design perfectly aligned the active region

to the peak of the optical mode for maximizing the confinement factor. These results confirm that the previously reported n–DBR can be effective for use as a reflector in surface–emitting optical devices. In addition, by changing the material of the spacer layers, a significant change in lasing peak wavelength was observed and this further confirms the observed stimulated emission was due to vertical laser operation.

CHAPTER VIII

ULTRAVIOLET MICROCAVITY LIGHT EMITTING DIODES

8.1 Introduction

VCSELs are known to have advantages of lower threshold current operation, circular and low–divergence output beam, and lower temperature sensitivity compared to edge–emitting laser diodes. In conventional electrical injection VCSELs, the formation of a current aperture plays a vital role in the device characteristics. Low threshold and single–transverse-mode (i.e. TEM_{00}) operation would not be possible without a well–defined current aperture to confine carriers to generate photons between the two DBRs. Since the introduction of the controlled oxidation process for the $Al_xGa_{1-x}As$ material system by Dallesasse and Holonyak in 1989 [91, 92], most VCSELs have employed oxidation for current aperture formation as well as optical confinement [93–95]. This technique has become one of the most commonly used fabrication techniques for traditional III–V compound semiconductor infrared VCSELs. However, for III–nitride–based emitters with peak emission wavelength in the ultraviolet to green wavelength range, the formation of Al–based native oxide layers has not proven feasible [96, 97]. As a result, various techniques were introduced such as, selective area growth of buried AlN [98], oxidizing AlInN [99], and selective activation[100].

Ion implantation is a commonly used material engineering process in silicon to form both n–type and p–type semiconductor by implanting dopant ions into silicon wafers. In addition, this technique is also employed for preparing silicon on insulator (SOI) substrates from conventional silicon substrates by implanting a high dose of

oxygen atom into the substrate and subsequently covert it to silicon oxide through high–temperature annealing. In the case of III–N compound semiconductors, ion implantation has been employed for device lateral isolation instead of for doping. This is due to the damage created by the implantation process can be rather difficult to remove for III–N's which limits the electrical conductivity. To mitigate implantation damage, nitrogen species were chosen as the implant species for this work. In this chapter, an ultraviolet microcavity light–emitting diode (MCLED) was demonstrated by including N^+–implantation process for current aperture definition. The devices have peak emission wavelength of ∼371.4 nm with the spectral linewidth of 5.1 nm at the highest pulsed current injection level of 15 kA/cm^2.

8.2 Experimental Procedures

The epitaxial growth for UV LEDs and UV MCLEDs was carried out in an AIXTRON 6 × 2" close–coupled–showerhead MOCVD reactor system. EpiPure® Trimethylaluminum ($Al(CH_3)_3$, TMAl), trimethylgallium ($Ga(CH_3)_3$, TMGa), and trimethylindium ($In(CH_3)_3$, TMIn) were used for group III precursors while ammonia (NH_3) was used for the group V precursor. To obtain *n*–type electrical conduction properties, silane (SiH_4) was used as *n*–type dopant source. On the other hand, the *p*–type doping was established by utilizing bis–cyclopentadienylmagnesium (Cp_2Mg) as dopant source. Based on the Hall measurements, the optimized *n*–type and *p*–type $Al_{0.06}Ga_{0.94}N$ has bulk resistivity of 1.173 × 10^{-2} and 2.181 Ω–cm, mobility of 241 and 4.36 cm^2/V/s, and free carrier concentration of 2.2 × 10^{18} and 6.6 × 10^{17} cm^{-3}, respectively.

Described in Fig. 50 is the schematic cross–section view of the MCLED device which is similar to our previously reported optically pumped VCSEL [101]. To emit photons in the ultraviolet range, the active region was designed to consist of a five–pair InGaN/AlGaN MQW structure with well and barrier thicknesses of 3 nm and 5 nm, respectively. Both *n*–type and *p*–type spacer layers formed with 120 nm $Al_{0.06}Ga_{0.94}N$

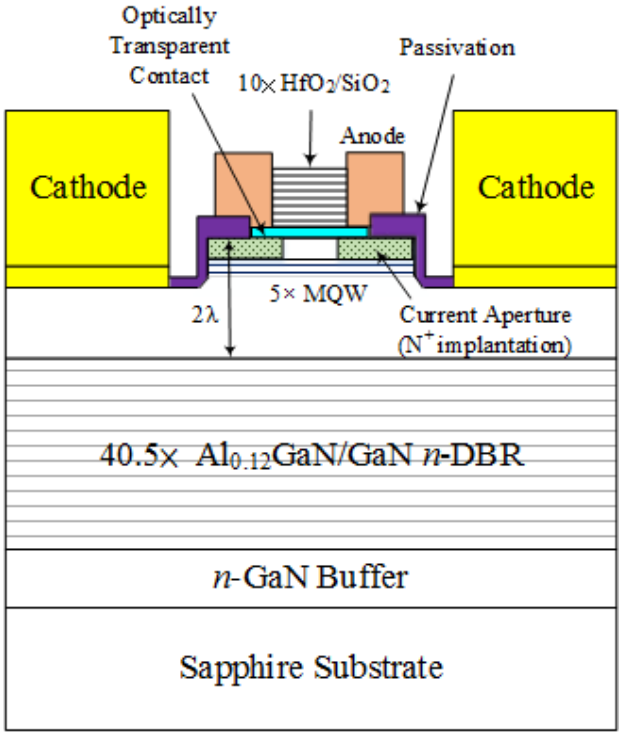

Figure 50: Cross–section schematic diagram for ultraviolet MCLED structure.

for aligning the peak optical mode to the active region. To enhance current spreading, a $\lambda/4$–thick (λ = 370 nm) indium–tin–oxide (ITO) layer was applied to the top of the p–AlGaN layer which created the nominal 9/4 λ–thick optical cavity of the MCLED structure. Among the optically transparent contacts available to date, ITO would probably be the only suitable choices of the material for near–UV VCSELs as it has a bandgap energy of $\sim$ 3.64 eV although it is not ideal due to optical absorption in the UV. Similar to a VCSEL, the MCLED structure requires both top and bottom distributed Bragg reflectors (DBRs) to form the optical cavity. In this work, the bottom DBR was composed with an electrically conducting AlGaN/GaN Si–doped n–DBR and detailed characterizations of the n–DBR can be found in our previous publication [67] and chapter IV. On the other hand, the top DBR was formed with SiO_2 and HfO_2 dielectric layers due to the fact that SiO_2 and HfO_2 are

both optically transparent as well as having a large refractive index contrast between the two materials (SiO_2: n $\sim$ 1.47, HfO_2: n $\sim$ 2.17) near the MCLED operating wavelength. In our previous reported work, SiO_2/HfO_2 DBRs were employed for deep–ultraviolet wavelengths and the obtained high reflectivity of 97% at 249.5 nm [90] shows these oxides are ideal for forming DBRs in the ultraviolet spectral range.

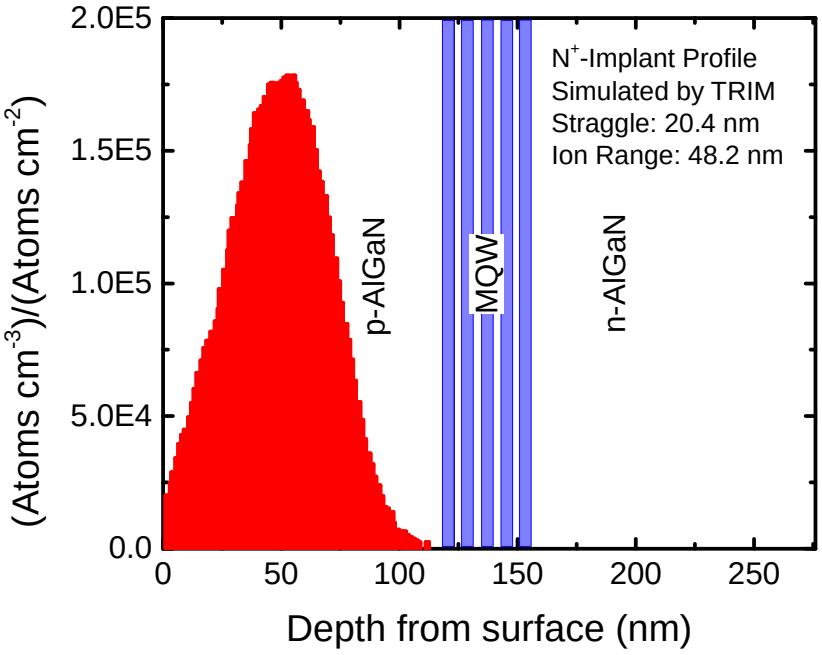

Figure 51: Simulated nitrogen ion distribution by TRIM. The effective N^+ ion implantation depth was estimated to be $\sim$ 482 $\mathring{A}$ with 204 $\mathring{A}$ of straggle. (Credit to Dr. Kao)

Following the MCLED growth, a series of fabrication process steps were performed by Dr. Kao to complete the device, beginning with the current aperture definition by N^+– implantation performed by an external company. The estimated implant profile simulated by Dr. Kao using the Transport of Ions in Matter (TRIM) software is shown in Fig. 51. To prevent the LED active region from being exposed to ion–bombardment damage, the N^+ implantation profile was designed to avoid ions penetrating the MQW

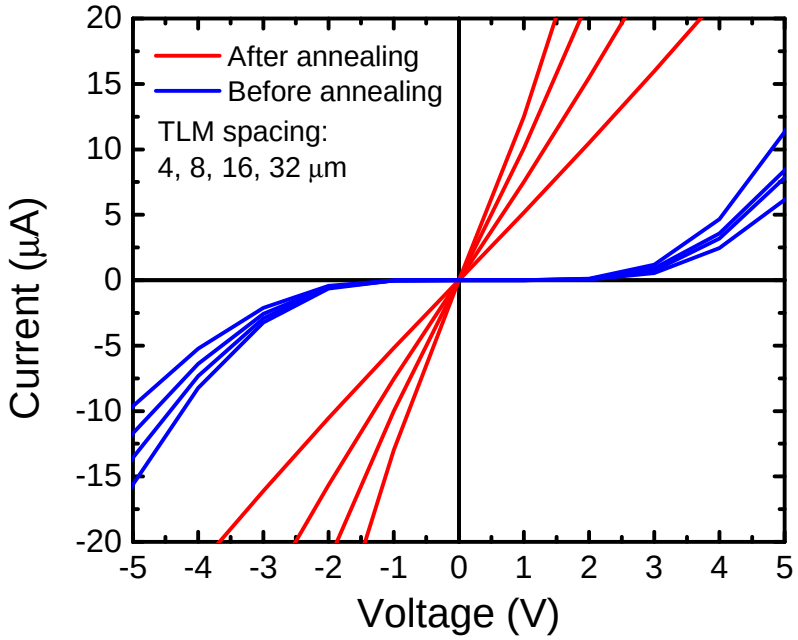

Figure 52: TLM results of ITO films before and after RTA annealing. (Credit to Dr. Kao)

structure; thus, an estimated implantation depth and straggle of 482 $\mathring{A}$ and 204 $\mathring{A}$ were used, respectively. Next, mesa etching with chlorine–based inductively coupled plasma (ICP) dry etching was performed to expose the n–spacer layer for n–type Ohmic contact formation. Vanadium–based V/Al/Ti/Au metal stacks were deposited to form an Ohmic contact with the n–$Al_{0.06}Ga_{0.94}N$ layer. To enhance current spreading for p–layers, ITO was used for a transparent p–type Ohmic contact. Owing to the fact that a ITO is placed within the optical cavity of the laser, it is important to understand the optical transparency of the material. With the optimized annealing condition of 500 °C, lowest optical loss (< 5 %) at $\lambda = 370$ nm can be achieved and the corresponding absorption coefficient (α) was measured as 4640 (cm^{-1}). The measured refractive indices (n) and the extinction coefficient (k) are 2.3 and 0.0855,

respectively, at $\lambda = 370$ nm. On the other hand, the ITO film also needs to achieve suitable contact resistance in addition to the given optical transparency. Shown in Fig. 52 are the TLM results on a p–$Al_{0.06}Ga_{0.94}N$ film with ITO contacts before and after annealing at 500 °C for 10 minutes in an oxygen ambient. ITO Ohmic contact is achieved on p–$Al_{0.06}Ga_{0.94}N$ and the specific contact resistance (ρ_c) is 7.4×10^{-2} Ω–cm^2.

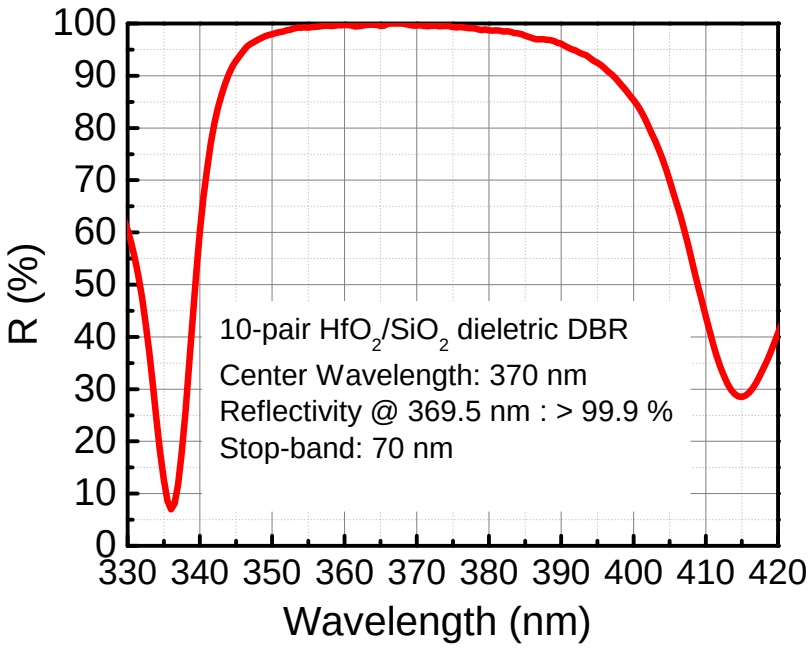

Figure 53: The measured reflectance for a ten–pairs dielectric DBR using SiO_2/HfO_2 quarter–wave plates with an intended center wavelength of 370 nm. (Credit to Dr. Kao)

To complete the optical cavity, a dielectric DBR consisting of ten–pair of $\lambda/4$–thick layers of HfO_2/SiO_2 was evaporated subsequently. The ten–pair DBR uses HfO_2/SiO_2 having a thickness of 42 nm/66 nm per pair with an intended center wavelength of the stop–band designed at 370 nm. Figure 53 show the measured reflectivity of the ten–pair HfO_2/SiO_2 DBR under normal incidence. The center wavelength is 370 nm

and the reflectivity at 369.5 nm is > 99.95 %. In spite of an asymmetric stop–band response due to the thickness uniformity in these DBR pairs, the achieved wide stop band (> 70 nm) ensures that it will effectively to cover the full range of the VCSEL emission at 370 nm. To complete the fabrication process, surface passivation using spin–on–glass (SOG) was performed and the electrical interconnects were formed by via etching as well as pad metal contact of Ti/Au deposition.

8.3 Results and Discussion

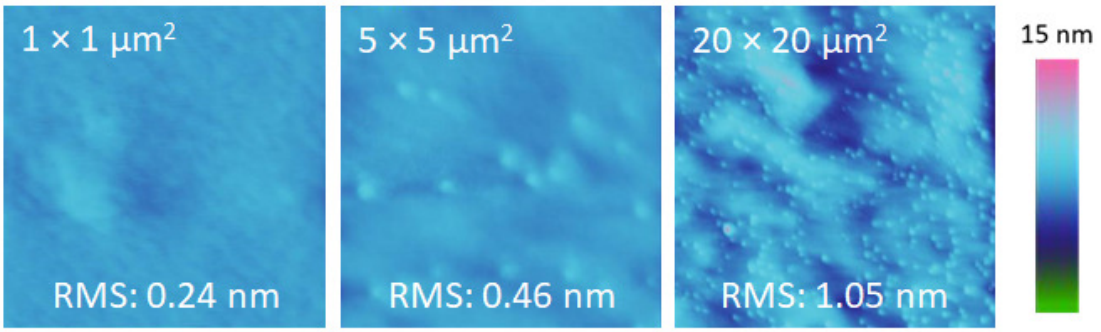

Figure 54: Atomic–force microscopy measurements of the MCLED on a sapphire substrate taken at 1×1 μm^2, 5×5 μm^2, and 20×20 μm^2 and the corresponding root–mean–square roughness is 0.24 nm, 0.46 nm, 1.05 nm, respectively.

After epitaxial growth, the wafer was inspected with different characterization methods prior to device fabrication. The wafer was first examined by AFM measurements as shown in Fig. 54. Compared to the previous AFM images for various structures, this set of images shows a lot of bumps (white dots) on the as–grown wafer and this surface feature originates from the p–type dopant, magnesium. Although such features increase the surface roughness, it is an expected characteristic of "properly" doped p–type material. Without Mg–bumps, the electrical conductivity of the p–type

material will be significantly degraded due to the corresponding low Mg doping. Even with these Mg–bumps, the overall surface is very smooth with a root–mean–square roughness of 0.24 nm, 0.46 nm, and 1.05 nm for 1 × 1 μm^2, 5 × 5 μm^2, and 20 × 20 μm^2 scans, respectively. The measured roughness is comparable to the same structure grown without any doping (0.11 nm, 0.38 nm, and 1.19 nm for 1 × 1 μm^2, 5 × 5 μm^2, and 20 × 20 μm^2); therefore, we can conclude that the high crystalline quality was maintained even with the introduction of dopants in the spacer layers.

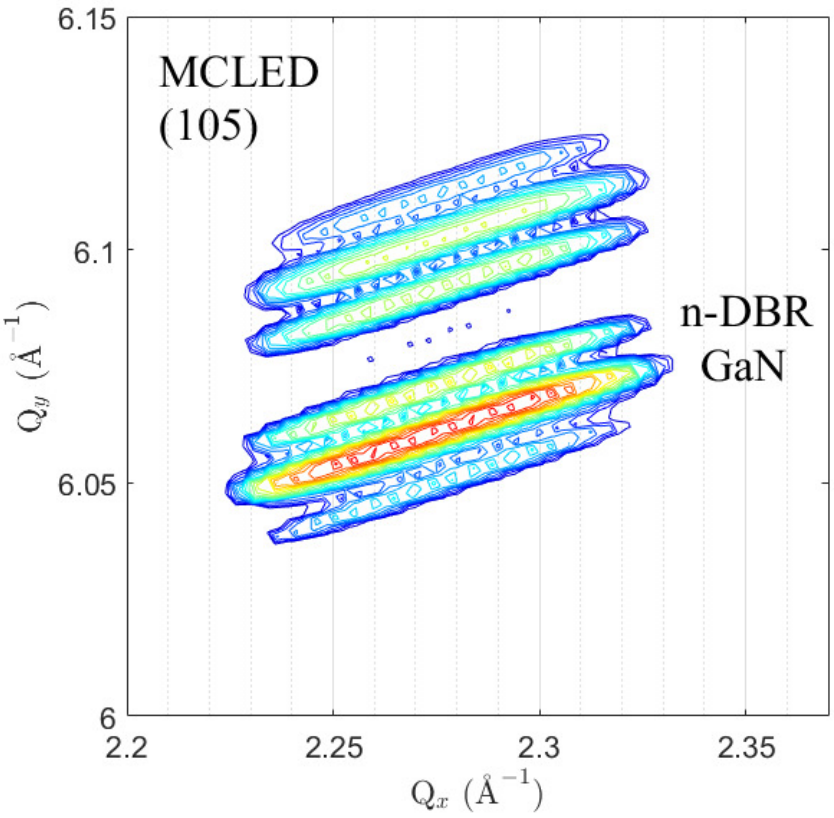

Figure 55: Asymmetric X–ray reciprocal–space mapping (RSM) based on the (105) diffraction peaks of the UV MCLED. The rlu variable represents the reciprocal lattice unit.

Shown in Fig. 55 is the reciprocal–space mapping (RSM) of the UV MCLED taken along the high angle asymmetric (105) reflection plane. The peak with highest

intensity can be easily identified as the n–GaN template as shown by the label in the figure. The immediate peak above the n–GaN template is the 40–pair n–DBR structure which is similar to the RSM presented earlier. Given that the cavity (spacer layers and MQW) structure is relatively thin compared to the rest of the structure and the average compositions are relatively close to the n–DBR, the cavity layers do not show up very distinctly. However, we are still able to conclude the entire epitaxial structure was grown pseudomorphically which eliminates defect formation due to strain relaxation.

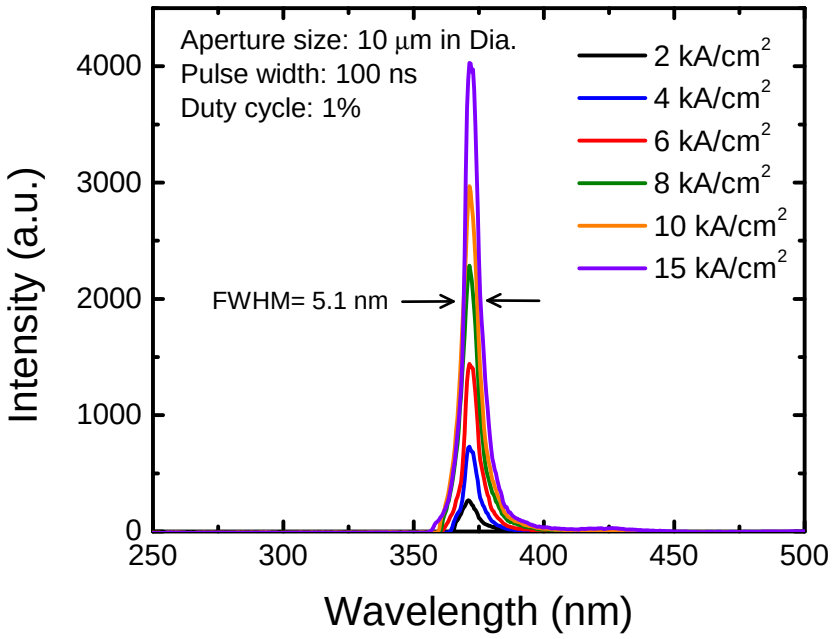

Figure 56: 300 K EL spectra of an ion–implanted MCLED at various pulsed current densities. (Credit to Dr. Kao)

Illustrated in Fig. 56 is the 300 K electroluminescence (EL) emission spectra of the fabricated ultraviolet MCLED with 10 μm diameter circular aperture measured by Dr. Kao. The EL measurements were performed at room temperature with a pulsed current source that had a pulse width of 100 ns and a 1% duty cycle. Laser action was

not observed at our highest measured pulsed current injection level of 15 kA/cm^2; however, spectral linewidth narrowing was observed with increased injected current

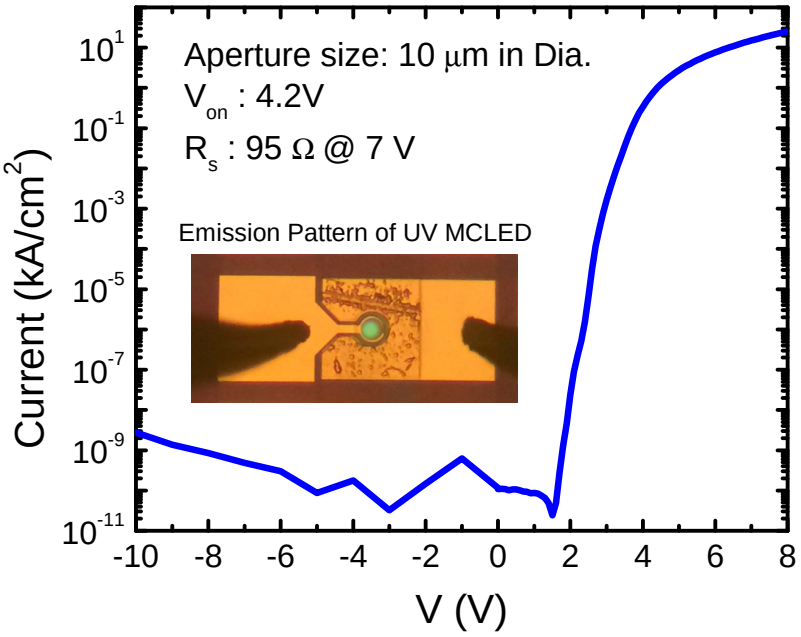

Figure 57: *I–V* characteristics of an implanted ultraviolet MCLED. The inset shows an optical microscope image of the visible "deep–level yellow emission" from the device. (Credit to Dr. Kao)

density. Under a current injection level of 2 kA/cm^2, the fabricated MCLED demonstrated a peak emission wavelength of 371.2 nm with a full–width half maximum (FWHM) of 6.1 nm. As the current density was increased from 2 kA/cm^2 to 15 kA/cm^2, a slight red–shift by 0.2 nm from a cavity mode was observed and the FWHM reduced down to 5.1 nm. The red–shift of the cavity mode is likely due to the heating under high current density injection conditions. While this LED emits primarily in the UV range, and this emission is therefore not seen with a standard optical microscope, the effectiveness of the carrier confinement can be observed from

the inset of Fig. 57 which shows the captured visible "deep–level" emission pattern from the 10 μm diameter device. This image shows the that the emitted photons are well confined and uniformly distributed within the defined circular aperture. Although N^+–implantation can be extremely limited in providing optical confinement owing to negligible change in the refractive index, the optical confinement achieved in this work can attributed to the hybrid mirror structure which provides large index contrast between dielectric DBR and air. Figure 57 also shows the I–V characteristic of an ultraviolet MCLED under DC measurement conditions at room temperature. The device has turn on voltage of $\sim$ 4.2 V and a series resistance of 95 Ω at 7V. The relatively low series resistance was partially due to the efficient lateral current transport by employing the n–DBR structure [67] beneath the n–spacer layer.

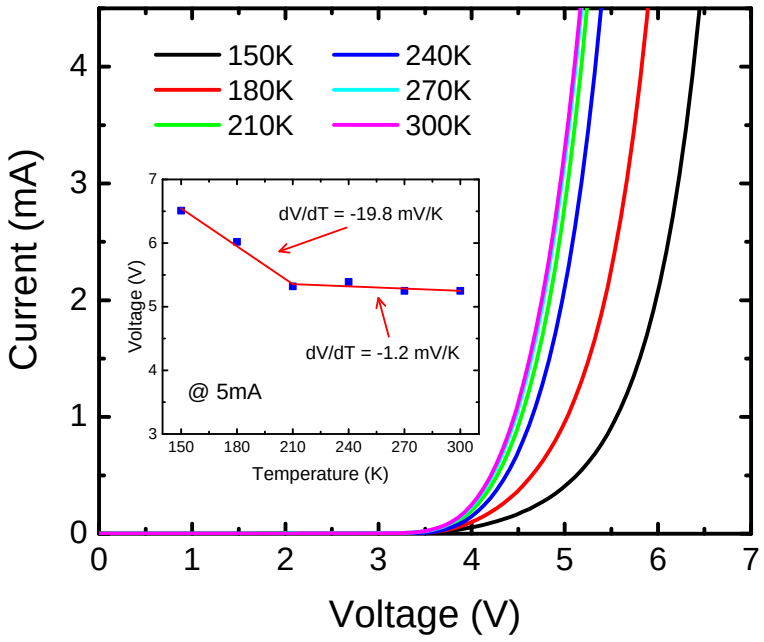

Figure 58: I–V characteristics of an implanted ultraviolet MCLED under various ambient temperature (150 K to 300 K). The inset shows the forward bias voltage for 5 mA under various temperature. (Credit to Mr. Mehta)

As the ambient temperature can have significant impact on device performance, another processed MCLED device was tested in our Lakeshore TTPX cryogenic probe station for temperature dependence measurements. The measurement was mainly performed by Mr. Mehta with my assistance. The Lakeshore TTPX probe station enables temperature–dependent measurement devices from 4.2 K to 475 K. The measurement chamber was first pumped down to 10^{-5} Torr to avoid ice formation from the water vapor in the air during the cooling process then temperature dependent electroluminescent measurements were performed between temperatures of 150 K to 300 K. Shown in Fig. 58 is the I–V characteristics of the MCLED from 150 K to 300 K with 30 K steps. As the ambient temperature decreases, the electrical properties of the diode degrade as expected. This is because the bandgap of material widens and the reduced thermal energy causes a reduction in the free–carrier concentration. The inset of Fig. 58 recorded the forward voltage at 5 mA current under various ambient temperatures. Two very distinctive slopes (dV/dT) were observed and the slopes were approximately -1.2 mV/K and -19.8 mV/K above and below 200 K, respectively. Utilizing the theoretical model in [102], the change in forward voltage in a p–n junction under various temperatures is given by

$$\frac{dV_j}{dT} = \left(\frac{qV_k - E_g}{qT} + \frac{1}{q}\frac{dE_g}{dT} - \frac{3k}{q} \right) \tag{49}$$

where V_j is the junction voltage, E_g is the bandgap energy, q is the elementary charge, and k is Boltzmann's constant. The above expression can be approximated as following [103]:

$$\frac{dV_j}{dT} \approx \frac{k}{q}\ln\left(\frac{N_D N_A}{N_C N_V}\right) - \frac{\alpha T(T+2\beta)}{q(T+\beta)^2} - \frac{3k}{q} \tag{50}$$

where N_D and N_A are the concentration of donors and acceptors, and α and β are the Varshni parameters. Given our p–n junction was formed by $Al_{0.06}Ga_{0.94}N$, linear interpolation was used to extract physical parameters of the material as shown in

table 8 (assuming density of states at 300K). Considering the doping density from

Table 8: Summary of the Physical Properties.

Material	N_C (cm^{-3})	N_V (cm^{-3})	α (meV/K)	β (K)
GaN	2.23E18	4.62E19	0.909	830
AlN	6.24E18	4.88E20	1.799	1462
$Al_{0.06}Ga_{0.94}N$	2.47E18	7.27E19	0.962	867.9

Assumed T = 300 K

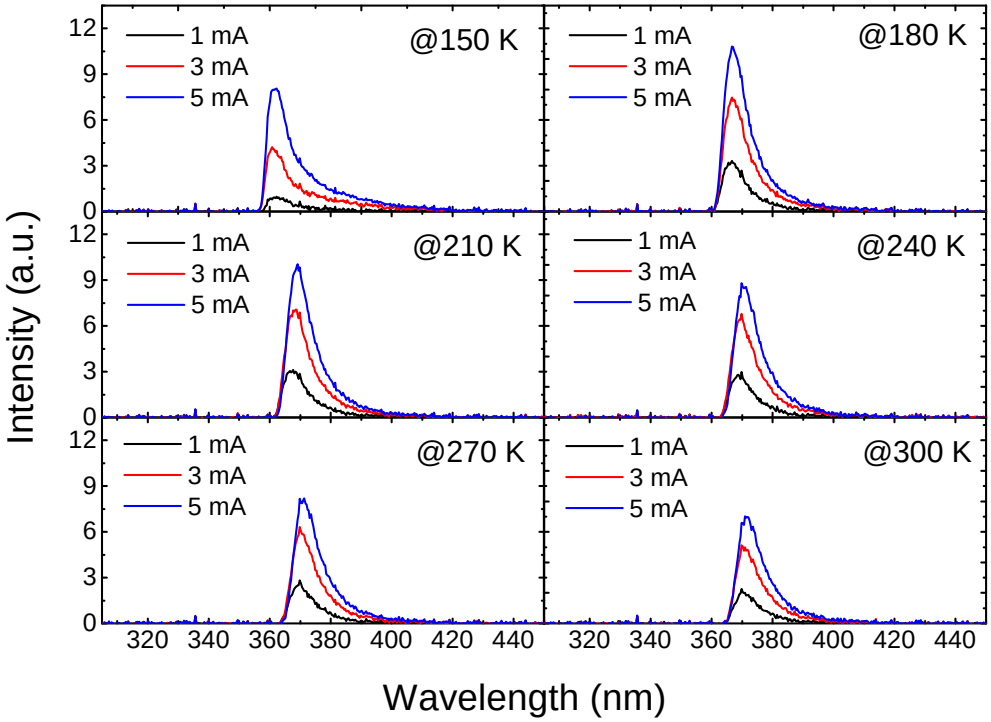

Figure 59: Electroluminescence spectra for UV MCLED under various temperature ambient from 150 K to 300 K under three different current levels (1 mA, 3 mA, and 5 mA). (Credit to Mr. Mehta)

Hall measurements described earlier (free carrier concentration of 2.2×10^{18} and 6.6×10^{17} cm^{-3} for n–type and p–type $Al_{0.06}Ga_{0.94}N$, respectively), the value of dV/dT for $Al_{0.06}Ga_{0.94}N$ p–n junction is -1.105 mV/K which matches our measured value very well. As the device temperature was cooled to cryogenic–temperature to $\sim$ 150 K, the dV/dT (-19.8 mV/K) is now determined by p–type layer characteristics and p–contact resistance [103].

Aside from the temperature dependence on the electrical properties, the EL characteristics also change with the decrease in the measurement temperature as shown in Fig. 59. All the panels in the figure were intentionally set to have identical ranges for visual clarity. From the luminescence spectra, we can notice that the optical intensity first increases as the temperature cooled down to 180 K then the intensity dropped off at 150 K and this phenomenon happened for all the three different applied currents as summarized in Fig. 60. The increases in the optical intensity as the device temperature decreases can be attributed to the fact that the MQW has a higher optical gain at lower temperature; however, this cannot explain the significant reduction (at least 20%) in the peak intensity as the device is cooled down to 150 K. Given that the p–side DBR has very wide stopband ($\sim$ 70 nm) and higher reflectivity, one of contributing factors for the reduction in the peak intensity may related to the relatively narrow band and lower reflectivity of the n–DBR. To verify this hypothesis, numerical analysis by Mr. Mehta was performed to extract reflectivity of n–DBR at 370 nm under various ambient temperatures as described in Fig. 60 by the green dashed curve. From the simulated result, the reflectivity increases with decreasing temperature and peaks near 258 K (R = 97.4 %). Once the temperature dropped below 200 K, the reflectivity at 370 nm decreases rapidly. As temperature cooled down to 150 K, the reflectivity of the n–DBR reduced to 92.2 %. Compared to these observations from the simulation in the ideal case, the reduction in reflectivity can be even more severe in the experimental case; however, there are other possibilities that

could help explain the intensity drop. The study of the peak wavelength provided additional insight.

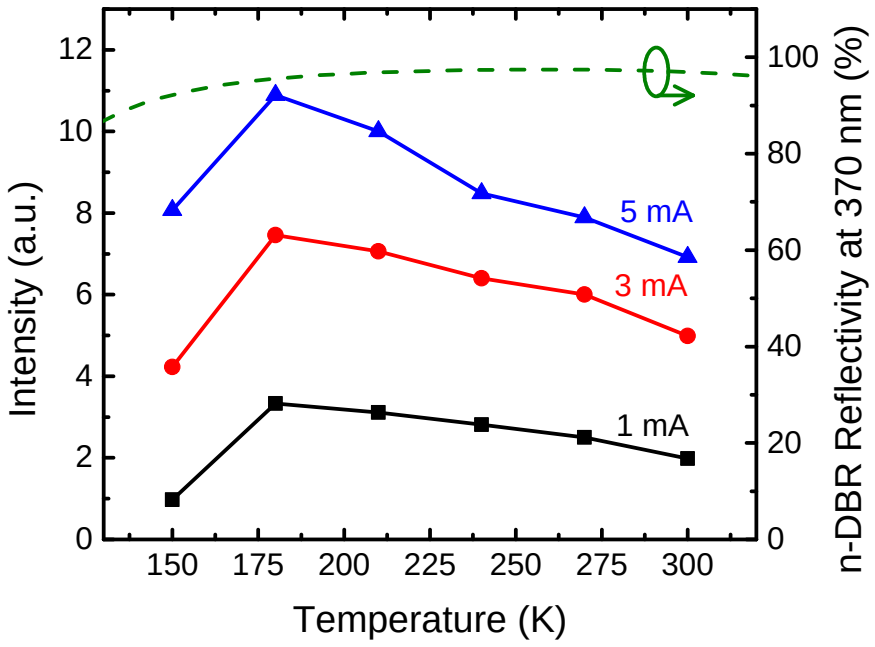

Figure 60: Peak electroluminescent intensity for a MCLED from 150 K to 300 K under three different current levels (1 mA, 3 mA, and 5 mA) versus simulated n–DBR reflectivity with same temperature range. (Credit to Mr. Mehta)

Described in Fig. 61 is the peak wavelength from the EL measurements under various temperatures and current levels. Regardless of the current level, the peak wavelength decreases with temperature until 180 K then a big decrease is observed for 150 K. The general trend of the decrease in the peak wavelength (or increase in the optical energy) is due to increases in the bandgap energy of material as the temperature decreases. Also shown in Fig. 61 is the bandgap energy of GaN at various temperatures based on the equation in Ref [104] and we also observed a similar decrease in the peak wavelength from our measurement. Keep in mind that the peak of the optical gain is not the sole factor in determining the peak wavelength,

the changes in the cavity mode also play a vital role. For GaN, the thermo–optic coefficient ($\partial n/\partial T$) is larger than 0 which means refractive index decreases with temperature. As a result, we can expect the cavity mode to under go a blue shift as we decrease the temperature given that the physical thickness of the device structure is fixed. With the thermo–optical coefficient at 369 nm $\sim 1.6 \times 10^{-4}$ [105] and 150 K change in temperature, we can expect the refractive index changed by 0.024 which translates to a change in the cavity mode by $3 \sim 4$ nm which isn't the result we observed at 150 K; therefore, the possible explanation is the cavity mode is no longer aligned to the optical gain profile which leads to significant decrease in the optical intensity as well as the abrupt peak wavelength change.

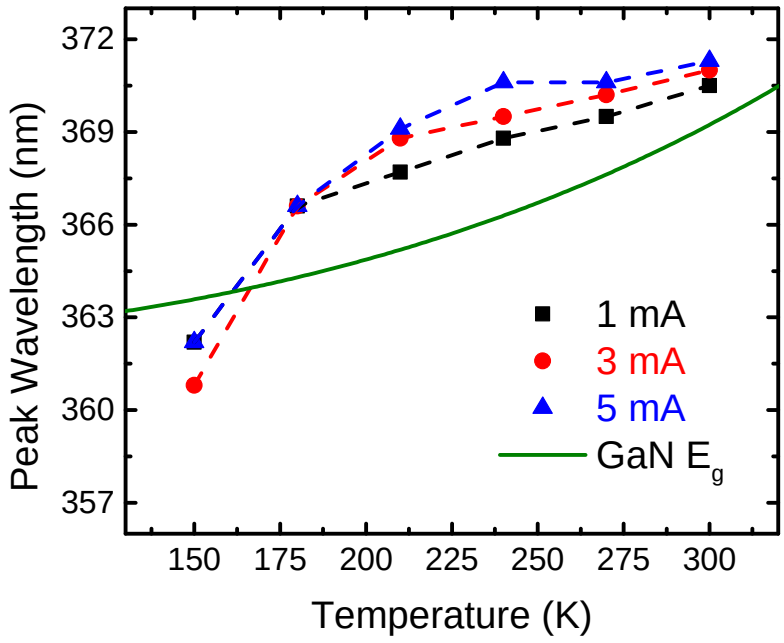

Figure 61: Peak electroluminescent wavelength for a MCLED from 150 K to 300 K under three different current levels (1 mA, 3 mA, and 5 mA) versus the bandgap energy of GaN.

In an effort to understand the full potential of this particular MCLED structure, the epitaxy was performed on a low dislocation density GaN "bulk substrate"; however, the fabricated devices demonstrated significant performance degradation compared to the ones simultaneously on an n–GaN/sapphire template. To achieve a high reflectivity DBR with a narrow bandwidth, precision growth rate control is required. Owing to the differences in the substrate thermal conductivity that causes differences in the epitaxial growth rate between sapphire and the GaN substrates, the growth process cannot be directly transferred since these growth–rate differences result in optical reflectivity of DBR to be severely degraded. To mitigate this issue, a wide stop–band DBR is desired and should be considered in future development. Aside from the non–optimal n–DBR originating from the differences in the thermal conductivity of substrate, the epitaxy performed on the GaN "bulk substrate" experienced a greater tensile strain than the corresponding layers on the n–GaN/sapphire template. As a result, the resulting cracks caused significant number of devices fabricated on the GaN "bulk substrate" to be shorted or have a higher leakage current which further limits the forward current drive of the devices.

To further study whether this particular device structure can be used to demonstrate an electrical injection VCSEL, a detailed analysis was performed to try to correlate the optically pumped VCSEL and this electrical injection MCLED. Utilizing the P_{th} obtained from the optical pumping experiment, a rough estimate of the threshold current density can be obtained. With the known material characteristics for our pump laser (KrF) wavelength of $\lambda = 248$ nm, the amount of light absorbed by the quantum wells at threshold can be estimated. After taking into account the reflectivity and the absorption from the dielectric DBR, the quasi–neutral region ($Al_{0.06}Ga_{0.94}N$), and the quantum barriers, it was estimated that ~ 34 % of the incident power reached quantum wells and that only 1.7 % of the incident photons would be absorbed by the wells. Furthermore, Auger or Shockley–Read–Hall recombination

further limits the amount of free–carrier concentration contributing to optical generation. For the worst–case–scenario assumptions, it was estimated that only ~ 1 % of the free carriers generated by the incident photon flux can contribute to optical emission. With the given photon energy of $h\nu = 5$ eV, a free–carrier concentration of 6.8×10^{14} cm^{-2} can be generated at P_{th}. The threshold current density can be estimated from

$$J_{th} = \frac{qn_{th}}{\tau_s} \tag{51}$$

where q is unit charge, n_{th} is the unit area threshold carrier density, and τ_s is carrier lifetime. With the given volumetric free carrier density at threshold ($N_{th} = 4.5 \times 10^{20}$ cm^{-3} for our 3 nm well), we can estimate the lifetime to be less than 1 ns [106]. For the purpose of estimation, free carrier lifetime of $\tau_s = 1$ ns was used for the calculation and the estimated threshold current density was determined to be ~ 109 kA/cm^2, which is $\sim$ 5x higher than current achievable current density.

8.4 Summary

In summary, an N^+–implantation process was employed for current aperture formation on a III–N ultraviolet MCLED structure. With the introduction of dopants for n and p spacer layers, high crystalline quality was observed by AFM and XRD measurement. Although laser action was not observed, the fabricated ultraviolet MCLEDs with the N^+–implant defined current aperture have a peak wavelength of ~ 371.4 nm with a spectral linewidth of 5.1 nm at the highest pulsed current injection level of 15 kA/cm^2 at 300 K. To realize a better electrically injected MCLED or even a VCSEL, a better n–side DBR with less tensile strain and higher reflectivity is an important requirement.

CHAPTER IX

ULTRAVIOLET LASER DIODE

9.1 Introduction

In the previous chapters, the detailed growth development for VCSELs was presented. With the best effort to this point, a VCSEL demonstration remained challenging. As a result, the development focus shifted to demonstrate edge–emitting laser diodes (LDs) with the same targeted wavelength of $\lambda = 369.5$ nm. Given an edge–emitting structure is known to have higher optical gain because of the optical cavity is formed orthogonal to the growth direction, the mirror loss and the cavity loss is less critical. Challenges such as high reflectivity DBRs and high–Q cavity in VCSEL study will no longer be a stepping stone to realize edge–emitting lasers. However, an edge–emitting laser structure does come with its own set of challenges. In the case of edge–emitting lasers, thick n–side and p–side claddings are required to confine optical mode and these claddings are typically consist of wider bandgap and low index material to minimize the optical absorption. As a result, thick $Al_xGa_{1-x}N$ layers with x $\sim$ 0.15 are required which can introduce significant tensile strain if the layers are epitaxially grown on GaN substrate. Once the material goes beyond the critical thickness, the tensile strain can cause fractures (cracks). Therefore, the usable area of wafer can be limited and the introduction of additional leakage path from cracks can limit the device performance. To mitigate the known tensile strain issue, an n–type $Al_{0.15}Ga_{0.85}N$ reduced threading–dislocation–density (reduced TDD) template on sapphire substrate from Sandia National Laboratories was used instead of GaN templates/substrates. The Si–doped $Al_{0.15}Ga_{0.85}N$ template has a typical doping level of $\sim 2 \times 10^{17} cm^{-2}$ with a low dislocation density of $2 \sim 3 \times 10^8$ cm^{-2} range.

The templates also exhibit a smooth surface with typical RMS roughness of < 0.2 nm under 9 μm^2 area and the detailed growth processes for such templates can be found in Ref. [107]. Given the same target wavelength and to maximize the optical gain, the optimized multi–quantum wells (MQWs) structure were inherited from the development in previous chapters. To efficiently inject holes into active region, inverse–tapered design will be employed for our p–layers.

9.2 Experimental Procedures

The epitaxial growth for edge–emitting lasers was carried out in an AIXTRON 6 $\times$ 2" close–coupled showerhead MOCVD reactor system. Metalorganic sources, Trimethylaluminum ($Al(CH_3)_3$, TMAl), trimethylgallium ($Ga(CH_3)_3$, TMGa), and trimethylindium ($In(CH_3)_3$, TMIn), with EpiPure® grade purity were used for group III precursors while ammonia (NH_3) was used for the group V precursor. To obtain n–type electrical conduction properties, silane (SiH_4) was used as the n–type dopant source. On the other hand, the p–type doping was established by utilizing bis–cyclopentadienylmagnesium (Cp_2Mg) as the dopant source. Based on the Hall measurements, the optimized n–type and p–type $Al_{0.1}Ga_{0.9}N$ has bulk resistivity of 4.925×10^{-3} and 7.35 Ω–cm, mobility of 626.5 and 2.313 $cm^2/V/s$, and free carrier concentration of 2.023×10^{18} and 3.672×10^{17} cm^{-3}, respectively. To achieve crack–free growth of $Al_{0.15}Ga_{0.85}N$ on GaN templates for Hall samples, the thicknesses of $Al_{0.15}Ga_{0.85}N$ layer must remain thin which can lead to the two–dimensional electron or hole gas (2DEG or 2DHG) at the $Al_{0.15}Ga_{0.85}N$ and GaN interface be detected by Hall measurement system. As a result, the measured bulk resistivity of material doesn't truly reflect the real material bulk resistivity due to the high carrier mobility distortion from either 2DEG or 2DHG. Therefore, the Hall data for the high aluminum mole fraction material is not available. Described in table 9 is the simulated epitaxial structure for 369 nm laser diodes by Mr. Mehta. Because of the high cost

for materials in each layers, similar growth conditions described in previous chapters are used in this study.

Table 9: A simulated 369 nm laser diode epitaxial structure.

Layer Name	Material	Thickness (nm)	Doping [Free Carrier] (cm^{-3})
p++ contact	GaN	20	Mg: 1E20
p–Taper	$Al_{0.15}Ga_{0.85}N$ → GaN taper	30	Mg: 5E18 [5.6E17]
p–Cladding	$Al_{0.15}Ga_{0.85}N$	500	Mg: 5E18 [5.6E17]
p–WG	$Al_{0.1}Ga_{0.9}N$	100	Mg: 5E18 [5.6E17]
EBL Taper	$Al_{0.25}Ga_{0.85}N$ → $Al_{0.1}Ga_{0.9}N$ taper	15	Mg: 5E18 [5E17]
EBL	$Al_{0.25}Ga_{0.85}N$	5	Mg: 5E18 [5E17]
MQW	$6\times Al_{0.12}Ga_{0.88}N$	7	Si: 1E16
	$5\times InGaN$	2.5	
n–WG	$Al_{0.1}Ga_{0.9}N$	100	Si: 3E18 [1.8E18]
n–Cladding (Template)	$Al_{0.15}Ga_{0.85}N$	semi–infinite	Si: 3E18 [1.8E18]

To verify the structural design experimentally, the growth was first performed on GaN templates (GaN on sapphire substrate) to demonstrate optically pumped lasers. Although the growth performed on GaN template will result in high tensile strain which generates cracks on the grown surface, these cracks won't be a limiting factor for optically pumped laser demonstration. Because of the simulation assumes the n–cladding is semi–infinite, a thick (> 1000 nm) n–$Al_{0.15}Ga_{0.85}N$ layer is required so the GaN templates has minimal effect on the optical mode of laser. In addition, the structure will only undergo optical pumping experiment, the p–taper layer and p++ contact layer will not be included as both layers are only required for electrical injection. Last but not least, doping is not included as well since the carriers will be injected through optical absorption of the excitation laser beam. Once the optically

pumped laser structure was grown, the wafer was cleaved into bars to form laser cavities. Then the laser bars will be characterized with our optical pumping measurement system similar to the schematic diagram in Fig. 44 in chapter VII except the pumping source is now 193 nm ArF excimer laser. The ArF excimer laser (193 nm, $\hbar\omega \approx 6.42$ eV) was running at a repetition rate of 10 Hz with a pulse width of 20 ns. The output of the laser passes through a series of steering mirrors and attenuators for power dependent measurements. At the exit of the attenuator, an optical aperture is used to shape the beam into a stripe geometry, which is 1.27 cm in height and 0.1 cm in width. The beam is either reflected to a power meter for power density measurements or illuminates the surface of laser bar. An optical fiber is placed in close proximity to the output facet of the laser bar to collect the emitted optical radiation. The far end of the fiber was connected to an Ocean Optics Maya 2000 Pro spectrometer ($\sim$ 0.1 nm resolution) by means of an SMA fitting.

After the demonstration of the optical pumped lasers, an electrical injection structure that would have grown on n–type $Al_{0.15}Ga_{0.85}N$ on SiC template purchased from Kyma Technologies Inc. will be first grown on n–type GaN template on sapphire substrate to check electroluminescence properties. Given magnesium atoms will bind with hydrogen atoms during growth, the standard 900°C for 3 min activation process (turn material to be p–type) is required prior to any characterizations. The wafer was then scratched with diamond cutter to expose n–layer to make electrical contacts. Indium balls were used to make contact with both n (on the scratch surface) and p layers. The electrical measurement was performed by using Keithley 2430 as power supply while the electroluminescence spectra were collected by the optical fiber placed on the surface of sample and analyzed by Ocean Optics Maya 2000 Pro spectrometer. The emission was collected from the surface is because the n–type GaN templates can absorb emission from the MQWs and alter the collected emission spectra.

After the demonstration of the optical pumped lasers and the characterization with

scratched diode, the real device growth will be performed on the n–type $Al_{0.15}Ga_{0.85}N$ on SiC template from Kyma Technologies Inc. Given the substrate is not ready prior to the completion of this thesis, growth and device fabrication processes cannot be completed in time. However, the characterizations performed on GaN templates/Sapphire substrate validates the growth development.

9.3 Results and Discussion

9.3.1 Optically Pumped Laser on GaN Templates

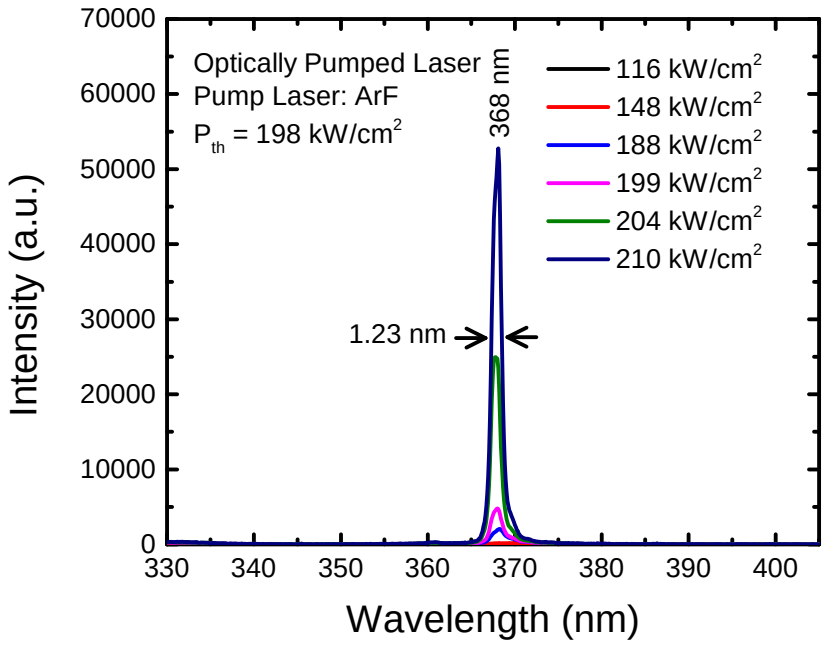

Figure 62: Optical emission spectra recorded at room temperature from an optically pumped laser bar under various excitation pumping power densities.

After the growth of the optically pumped laser structure on GaN templates, a Fabry–Perot etalon was formed by cleaving along m–plane of sapphire substrate (the crystal orientation between sapphire and III–nitride are off by 30°) to form a cavity with a length of 8.95 mm. The bar length was intentionally kept shorter than the height of

the optical aperture (12.7 mm) to ensure entire bar is uniformly illuminated by the pump laser (ArF). The optical emission spectra recorded at room–temperature with various pumping power densities are described in Fig. 62. The laser emission has a peak wavelength at 368 nm with a spectral linewidth reducing to 1.32 nm at the maximum measured excitation power density of 210 kW/cm^2.

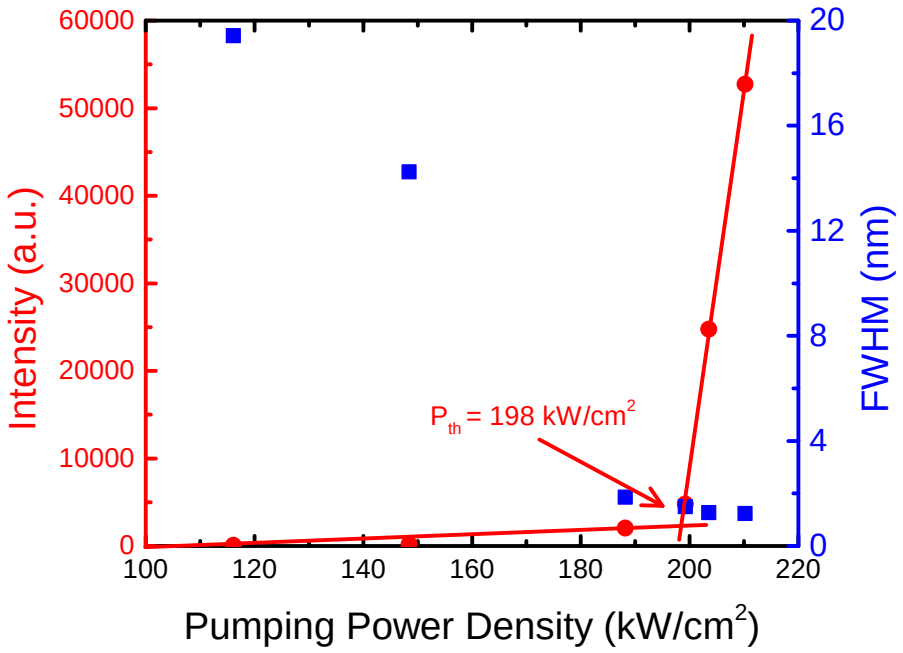

Figure 63: Laser bar emission intensity (in blue squares) and spectral linewidth (in red circles) as a function of pumping power density. The laser threshold is determined to be 198 kW/cm^2.

Shown in Fig. 63 is the optical output intensity as a function of excitation power density (L–L curve) and a distinct threshold power density (P_{th}) characteristics was observed at 198 kW/cm^2. Because of air and semiconductor material has an refractive index contrast that can cause optical reflection, the amount of excitation pumping power density that actually transmitted into the material can be estimated by the Fresnel equation. Given the pump laser beam is normal to the laser bar surface, the

amount of optical intensity that enters material is roughly 73.9 % of recorded values and the threshold pumping power density that enters the material was calculated to be 146 kW/cm^2 which is an achievable power density under electrical injection. In addition, the imaginary part of the dielectric function of $Al_xGa_{1-x}N$ material has an higher energy critical point near 7 eV as presented by Buchheim et al. [108]. As a result, an increase in optical attenuation coefficient can be expected based on following relation:

$$\alpha = \sqrt{\sqrt{\frac{\epsilon_i^2 + \epsilon_r^2}{2}} - \frac{\epsilon_r}{2}} \tag{52}$$

With the photon energy for our pump laser ($h\nu = 6.42$ eV), it is expected that the measured threshold pumping power density is substantially higher than it would be pumping with lower energy photons such as KrF excimer laser ($h\nu = 5$ eV). In Fig. 63, the full width at half maximum of spectra linewidth as a function of pumping power density is described as blue squares. Another laser characteristics is described as an abrupt narrowing (14 nm to 2 nm) was observed once the pumping power density nears the threshold pumping power density of the laser.

9.3.2 369 nm LD Structure on n–GaN Templates

After optical pumping characterizations, the next study is to understand how the devices behave under electrical injection. Figure 64 shows the I–V characteristics of the scratched diode under DC measurement conditions at room temperature. Although the diode didn't undergo a rigorous fabrication process, the measurement result can still be very insightful for predicting the electrical characteristics of the fabricated devices. One of the most valuable information is device has turn on voltage of ~ 5 V which indicates the proper doping level for all the layers in the epitaxial structure. Illustrated in Fig. 65 is the room temperature EL emission spectra of the scratched

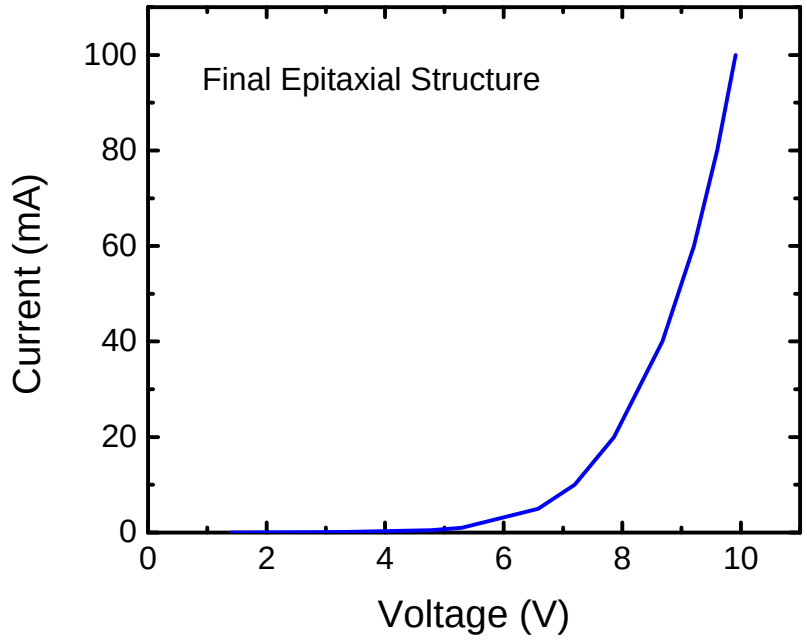

Figure 64: I–V characteristics of a scratched diode.

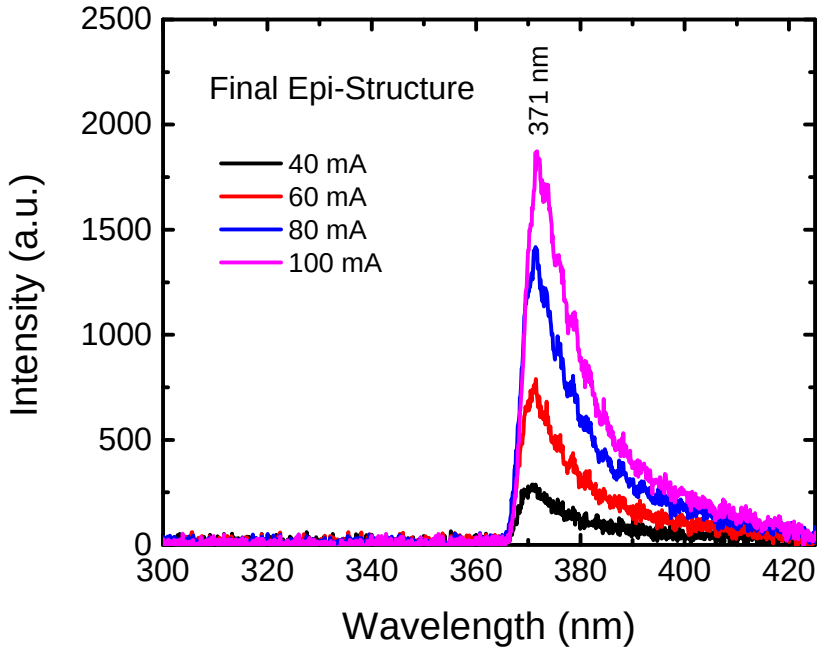

Figure 65: 300 K EL spectra of a scratched diode at various current injection.

diode under DC measurements condition. At the highest injected current level, the scratched diode demonstrated a peak emission wavelength of 371.9 nm with a spectral linewidth of 10.3 nm. In addition, the peak EL experienced a red–shift of $\sim$ 1.1 nm when the injected current increased from 40 mA to 100 mA and this is mainly because of quantum–confined Stark effect (QCSE). With the measured electrical and optical data, the growth process is ready to perform the final epitaxy growth on the substrates purchased from Kyma Technologies Inc.

9.4 Summary

In summary, the growth development for UV laser diodes with a peak emission wavelength of $\lambda = 369.5$ nm was described. An optically pumped III–N UV edge–emitting laser was grown on a GaN template on sapphire substrate by MOCVD was demonstrated. The peak photoluminescence emission wavelength of the laser was $\lambda = 371.9$ nm with a threshold pumping power density of 198 kW/cm^2 and a spectral linewidth of 1.32 nm under ArF excimer laser pumping. Then a scratched diode with the epitaxial structure identical to the one that will be performed on the AlGaN templates purchased from Kyma Technologies Inc. was fabricated. From the electrical characterizations, the scratched diode has a turn on voltage of $\sim$ 5V and a peak EL wavelength of 371 nm at room temperature. These results validate the growth development for the edge–emitting laser diodes and the growth can be directly performed on the reduced TDD AlGaN templates once they are available.

CHAPTER X

SUMMARY AND FUTURE WORK

Since the emergence of efficient III–nitride emitters in mid–/late– 1990s, researchers around the globe invested tremendous efforts and resources in the development of III–nitride technology for next–generation optoelectronic devices. With the great commercial success in III–N light–emitting diodes (LEDs), laser diodes (LDs), and photodiodes (PDs) operating from green to near–ultraviolet wavelength range in recent years, research efforts continue in working toward the ultraviolet and deep–ultraviolet wavelength ranges. While the nitride community has moved the focus research toward the ultraviolet wavelength range, the growth technology itself has been dominated by metalorganic chemical vapor deposition (MOCVD) due to its versatility and scalability.

With an increasing need in narrow linewidth ultraviolet lasers for critical applications, this study focused on the development of an ultraviolet vertical–cavity surface–emitting lasers (VCSELs) targeting a peak emission wavelength of $\lambda = 369.5$ nm for chip–scale Yb atomic clock applications. Given the nature of such a challenging program, the study focused on individual aspects of the growth and design of III–N diode lasers before demonstrating an ultraviolet p–n junction emitter. In additionally, a traditional electrical injection VCSEL consists of several key structural components including, top and bottom distributed Bragg reflectors (DBRs) for forming a high–quality–factor (high–Q) vertical cavity, spacer layers for optical mode alignment as well as lateral and vertical carrier transport from the anode and cathode, and multi–quantum wells (MQWs) for photon generation. Using the growth

and fabrication technologies developed to date, this study focused on solving the p–spacer vertical–hole–transport issue and growth of a high–quality n–side DBR. By integrating these developed technologies, VCSELs under optical pumping as well as electrically injected micro–cavity light–emitting diodes (MCLEDs) were developed. Although microcavity light–emitting diodes were the final electrical injection device demonstrated in this study, a list of potential solutions for further development of ultraviolet VCSELs will be discussed in the next section.

To achieve the final goal of the study, the first study focused on the development of proper p–spacer layer for vertical hole injection. Magnesium (Mg), the commonly used p–type dopant in III–N material system, has large activation energy which limits the p–type conductivity of the material. The situation worsens approaching wider bandgap material because of increase in activation energy of Mg dopants at the same time. To solve the problem of hole transport for vertical injection, a high–aluminum–containing ([Al]$\sim$0.6) AlGaN MQW double–heterojunction (DH) emitter grown by MOCVD on a c plane Al–polar AlN bulk substrate was demonstrated. Employing an inverse–tapered–composition AlGaN:Mg p–type waveguide design effectively reduces the forward resistance and leads to a reduced turn–on voltage while maintaining a high level of current conduction. The fabricated device can sustain a DC current of at least 500 mA and a pulsed current of at least 1.07 A, which corresponds to a current density of 10 and 18 kA/cm^2 at maximum measured voltage of 15 and 20 V with the measured series resistance of 15 and 11 Ω, respectively.

Next, the development focus shifted toward realizing the required n–side DBR. In this work, three different DBR approaches were demonstrated. First, an electrically conducting 40–pair silicon–doped $Al_{0.12}Ga_{0.88}N$/GaN n–type DBR grown by MOCVD on a silicon–doped n–type GaN template was developed. The n–DBR demonstrated a peak reflectivity of 91.6% at 368 nm with a bandwidth of 11 nm. A high crystalline

quality was verified by AFM and TEM imaging techniques. Be performing a mesa–etching and metal–contact formation on this 40–pair n–DBR, the vertical resistance of 5.5 Ω, which corresponds to bulk resistivity of 0.52 Ω–cm, near the maximum measured current of 100 mA was obtained.

To further increase the index contrast between the bilayers, a novel strain management approach utilizing GaN interlayers enables the possibility to increase the aluminum mole fraction without the formation of cracks. A crack–free growth of a 45–pair $Al_{0.30}Ga_{0.70}N/Al_{0.04}Ga_{0.96}N$ DBR by MOCVD on AlN template was demonstrated. We found that inserting an 11 nm–thick GaN interlayer upon the interface with the AlN template resulted in reduced strain so that smooth low–aluminum–content $Al_xGa_{1-x}N$ layers were formed. The DBR material quality as well as the interfaces were studied using STEM–HAADF imaging and smooth surfaces with sharp interfaces were observed throughout the structure. Furthermore, high–resolution XRD RSM scans and diffraction patterns showed that the GaN interlayer effectively relaxes the compressive strain from the AlN and enables smooth surface formation for the subsequently grown $Al_xGa_{1-x}N$ layers. The 45–pair AlGaN–based DBR has a peak reflectivity of 95.4% at 368 nm with a bandwidth of 15 nm.

Lastly, to improve the electrical characteristics for vertical electron transport, a compositionally graded $Al_xGa_{1-x}N$ silicon doped n–DBR with x varying from 0 to 0.12 was demonstrated. With the compositionally graded n–DBR the dominant transport mechanism changed from thermionic emission to drift–diffusion and the corresponding I–V characteristics also changed from an exponential curve to a linear behavior. However, the compositionally graded $Al_xGa_{1-x}N$ n–DBR suffers from more exitonic sub–bandgap absorption and a narrower bandwidth of the reflectivity spectrum. The achieved peak reflectivity for undoped and n–type compositionally graded $Al_xGa_{1-x}N$ DBRs are 70 and 60.5 %, respectively.

With the technology developed for both p–spacer and n–side DBR, an optically

pumped III–N VCSEL with an effective 8λ–thick cavity grown on an n–GaN template on a sapphire substrate by MOCVD was demonstrated. The hybrid–mirror VCSEL employed a seven-pair of HfO_2/SiO_2 dielectric stack as the top DBR, while the bottom DBR was formed by an electrically conducting n–type DBR composed of 40–pairs of $Al_{0.12}Ga_{0.88}N/GaN$. The peak emission wavelength of the VCSEL was $\lambda = 374.9$ nm with a threshold pumping power density of 1.64 MW/cm^2 with a spectral linewidth of 0.66 nm. Numerical simulations demonstrated that the epitaxial design perfectly aligned the active region to the peak of the optical mode to maximize the confinement factor. These results confirmed that the previously demonstrated n–DBR can be effective for surface–emitting devices.

With the great success in optically pumped VCSEL, the same n–DBR was employed for electrical injection surface–emitting devices. By integrating the growth technologies developed so far along with the development of indium–tin–oxide (ITO) for current spreading as well as using an N^+–implantation process for current aperture, a III–N ultraviolet MCLED was demonstrated on GaN template on sapphire substrate. The fabricated ultraviolet MCLED has a peak emission at $\lambda = 371.4$ nm while the spectra linewidth narrowed down to 5.1 nm at the highest measured current injection level of 15 kA/cm^2.

10.1 Future Work

To further improve the device performance for achieving a VCSEL or even high–Q MCLED, the future development will depend heavily on improvement in the n–side DBR. A more probable solution for achieving a high reflectivity n–side DBR may involve using materials outside of III–N material system. Below are the ideas that are certainly worthwhile for further study:

1. Double–sided Dielectric Mirrors VCSEL:

   One of the most intuitive way is to utilize the high reflectivity 10-pair HfO_2/SiO_2

dielectric stacks as the both top and bottom DBR. Since an epitaxially grown DBR is not required, a more complex cavity structure can be employed for reducing optical loss and lowering threshold current density. To deposit dielectric stacks on the n–side of cavity, substrate removal or backside via hole opening by chemical–mechanical polishing (CMP), inductively coupled plasma (ICP) dry etch process, and photo–enhanced chemical (PEC) wet etch can be considered.

2. Air–gap Based Mirror VCSEL:

   Another possible solution is to selectively remove nitride material to form air/III–N material DBR. The known selectively etching processes are photo–enhanced chemical (PEC) wet etch and electro–chemical wet etch with the means of selectivity based on bandgap and conductivity, respectively. Utilizing the air–gap based DBR can certainly reduce the challenges in epitaxial growth for managing tensile strain and enable a more complex cavity structure as mentioned earlier in double–sided dielectric mirror approach.

REFERENCES

[1] J. Hecht, "Short history of laser development," *Opt. Eng.*, vol. 49, p. 49, 2010.

[2] T. H. Maiman, "Stimulated Optical Radiation in Ruby," *Nature*, vol. 187, pp. 493–494, 1960.

[3] R. N. Hall, G. E. Fenner, J. D. Kingsley, T. J. Soltys, and R. O. Carlson, "Coherent Light Emission From GaAs Junctions," *Phys. Rev. Lett.*, vol. 9, p. 366, 1962.

[4] M. I. Nathan, W. P. Dumke, G. Burns, J. F. H. Dill, and G. Lasher, "STIMULATED EMISSION OF RADIATION FROM GaAs p–n JUNCTIONS," *Appl. Phys. Lett.*, vol. 1, p. 62, 1962.

[5] N. Holonyak and S. F. Bevacqua, "COHERENT (VISIBLE) LIGHT EMISSION FROM Ga($As_{1-x}P_x$) JUNCTIONS," *Appl. Phys. Lett.*, vol. 1, p. 82, 1962.

[6] T. M. Quist, R. H. Rediker, R. J. Keyes, W. E. Krag, B. Lax, A. L. McWhorter, and H. J. Zeigler, "SEMICONDUCTOR MASER OF GaAs," *Appl. Phys. Lett.*, vol. 1, p. 91, 1962.

[7] S. Nakamura, M. Senoh, S.-I. Nagahama, N. Iwasa, T. Yamada, T. Matsushita, H. Kiyoku, and Y. Sugimoto, "InGaN–Based Multi–Quantum–Well-Structure Laser Diodes," *Jpn. J. Appl. Phys.*, vol. 35, p. L74, 1996.

[8] P. Quayle, K. He, J. Shan, and K. Kash, "Synthesis, lattice structure, and band gap of $ZnSnN_2$," vol. 3, 2013.

[9] H. Soda, K. i. Iga, C. Kitahara, and Y. Suematsu, "GaInAsP/InP Surface Emitting Injection Lasers," *Jpn. J. Appl. Phys.*, vol. 18, p. 2329, 1979.

[10] Y. Higuchi, K. Omae, H. Matsumura, and T. Mukai, "Room–Temperature CW Lasing of a GaN–Based Vertical–Cavity Surface–Emitting Laser by Current Injection," *Appl. Phys. Express*, vol. 1, p. 121102, 2008.

[11] T.-C. Lu, S.-W. Chen, T.-T. Wu, P.-M. Tu, C.-K. Chen, C.-H. Chen, Z.-Y. Li, H.-C. Kuo, and S.-C. Wang, "Continuous wave operation of current injected GaN vertical cavity surface emitting lasers at room temperature," *Appl. Phys. Lett.*, vol. 97, p. 071114, 2010.

[12] D. Kasahara, D. Morita, T. Kosugi, K. Nakagawa, J. Kawamata, Y. Higuchi, H.Matsumura, and T. Mukai, "Demonstration of Blue and Green GaN–Based Vertical–Cavity Surface–Emitting Lasers by Current Injection at Room Temperature," *Appl. Phys. Express*, vol. 4, p. 072103, 2011.

[13] T. Onishi, O. Imafuji, K. Nagamatsu, M. Kawaguchi, K. Yamanaka, and S. Takigawa, "Continuous Wave Operation of GaN Vertical Cavity Surface Emitting Lasers at Room Temperature," *IEEE J. Quantum Elect.*, vol. 48, p. 1107, 2012.

[14] G. Cosendey, A. Castiglia, G. Rossbach, J.-F. Carlin, and N. Grandjean, "Blue monolithic AlInN–based vertical cavity surface emitting laser diode on free–standing GaN substrate," *Appl. Phys. Lett.*, vol. 101, p. 151113, 2012.

[15] C. Holder, J. S. Speck, S. P. DenBaars, S. Nakamura, and D. Feezell, "Demonstration of Nonpolar GaN–Based Vertical–Cavity Surface–Emitting Lasers," *Appl. Phys. Express*, vol. 5, p. 092104, 2012.

[16] Y. C. Cheng, X. L. Wu, J. Zhu, L. L. Xu, S. H. Li, and P. K. Chu, "Optical properties of rocksalt and zinc blende AlN phases: First–principles calculations," *J. Appl. Phys.*, vol. 103, p. 073707, 2008.

[17] X. M. Zhang, R. S. Ma, X. C. Liu, G. Z. Xu, E. K. Liu, G. D. Liu, Z. Y. Liu, W. H. Wang, and G. H. Wu, "Topological insulators with unexpectedly HgTe–like band inversion in hexagonal wurtzite–type binary compounds," *Europhysics Lett.*, vol. 103, p. 57012, 2013.

[18] S. R. Lee, A. F. Wright, M. H. Crawford, G. A. Petersen, J. Han, and R. M. Biefeld, "The band–gap bowing of $Al_xGa_{1-x}N$ alloys," *Appl. Phys. Lett.*, vol. 74, p. 3344, 1999.

[19] Q. S. Paduano, D. W. Weyburne, L. O. Bouthillette, S.-Q. Wang, and M. N. Alexander, "The Energy Band Gap of $Al_xGa_{1-x}N$," *Jpn. J. Appl. Phys.*, vol. 41, p. 1936, 2002.

[20] W. Shan, J. W. A. III, K. M. Yu, W. Walukiewicz, E. E. Haller, M. C. Martin, W. R. McKinney, and W. Yang, "Dependence of the fundamental band gap of $Al_xGa_{1-x}N$ on alloy composition and pressure," *J. Appl. Phys.*, vol. 85, p. 8505, 1999.

[21] J. Wu, W. Walukiewicz, K. M. Yu, J. W. A. III, E. E. Haller, H. Lu, and W. J. Schaff, "Small band gap bowing in $In_{1-x}Ga_xN$ alloys," *Appl. Phys. Lett.*, vol. 80, p. 4741, 2002.

[22] W. Walukiewicz, S. Li, J. Wu, K. Yu, J. A. III, E. Haller, H. Lu, and W. J. Schaff, "Optical properties and electronic structure of InN and In–rich group III–nitride alloys," *J. Cryst. Growth*, vol. 269, p. 119, 2004.

[23] A. E. Romanov, T. J. Baker, S. Nakamura, J. S. Speck, and E. U. Group, "Strain–induced polarization in wurtzite III–nitride semipolar layers," *J. Appl. Phys.*, vol. 100, p. 023522, 2006.

[24] M. Suzuki and T. Uenoyama, " Biaxial Strain Effect on Wurtzite GaN/AlGaN Quantum Well Lasers," *Jpn. J. Appl. Phys.*, vol. 35, pp. 1420–1423, 1996.

[25] S. L. Chuang and C. S. Chang, "A band–structure model of strained quantum–well wurtzite semiconductors," *Semicond. Sci. Technol.*, vol. 12, p. 252, 1997.

[26] H. Morkoç, S. Strite, G. B. Gao, M. E. Lin, B. Sverdlov, and M. Burns, "Large–band–gap SiC, III–V nitride, and II–VI ZnSe–based semiconductor device technologies," *J. Appl. Phys.*, vol. 76, p. 1363, 1994.

[27] I. Vurgaftman and J. R. Meyer, "Band parameters for nitrogen–containing semiconductors," *J. Appl. Phys.*, vol. 94, p. 3675, 2003.

[28] H. M. Manasevit, "SINGLE–CRYSTAL GALLIUM ARSENIDE ON INSULATING SUBSTRATES," *Appl. Phys. Lett.*, vol. 12, p. 156, 1968.

[29] A. Cho and J. Arthur, "Molecular beam epitaxy," *Prog. Solid State Chem.*, vol. 10, Part 3, p. 157, 1975.

[30] H. M. Manasevit and W. I. Simpson, "The use of metal-organics in the preparation of semiconductor materials," *J. Electrochem. Soc.*, vol. 116, p. 623., 1984.

[31] R. D. Dupuis, P. D. Dapkus, R. D. Yingling, and L. A. Moudy, "High–efficiency GaAlAs/GaAs heterostructure solar cells grown by metalorganic chemical vapor deposition," *Appl. Phys. Lett.*, vol. 31, p. 201, 1977.

[32] R. D. Dupuis, P. D. Dapkus, J. N. Holonyak, E. A. Rezek, and R. Chin, "Room–temperature laser operation of quantum–well $Ga_{1-x}Al_xAs$–GaAs laser diodes grown by metalorganic chemical vapor deposition," *Appl. Phys. Lett.*, vol. 32, p. 295, 1978.

[33] J. Kim, *Growth and characterization of III-nitride semiconductors for high-efficient light-emitting diodes by metalorganic chemical vapor deposition* . PhD thesis, Georgia Institute of Technology, 2014.

[34] G. Binnig and H. Rohrer, "Scanning tunneling microscopy," *IBM J. Res. Dev.*, vol. 44, pp. 279–293, 2000.

[35] G. Binnig, C. F. Quate, and C. Gerber, "Atomic Force Microscope," *Phys. Rev. Lett.*, vol. 56, pp. 930–933, 1986.

[36] "Atomic force microscopy," 2018. [Online; accessed 26-Mar-2018].

[37] "Basic Contact AFM & Dynamic Force Microscope (DFM)," 2018. [Online; accessed 26-Mar-2018].

[38] L. J. van der Pauw, "A Method of Measuring Specific Resistivity and Hall Effect of Discs of Arbitrary Shapes," *Philips Res. Rep.*, vol. 13, pp. 1–9, 1958.

[39] L. J. van der Pauw, "A Method of Measuring the Resistivity and Hall Coefficient on Lamellae of Arbitrary Shape," *Philips Tech. Rev.*, vol. 20, pp. 220–224, 1958.

[40] Accent, *Hall Effect Measurement System with HL5550PC Liquid Nitrogen Cryostat Stage HL5580PC Buffer Amplifier*, 5 ed., 2003.

[41] S. Nakamura, N. Iwasa, M. Senoh, and T. Mukai, "Hole Compensation Mechanism of P–Type GaN Films," *Jpn. J. Appl. Phys.*, vol. 31, pp. 1258–1266, 1992.

[42] H. Amano, M. Kito, K. Hiramatsu, and I. Akasaki, "P–Type Conduction in Mg-Doped GaN Treated with Low-Energy Electron Beam Irradiation (LEEBI)," *Jpn. J. Appl. Phys.*, vol. 28, pp. L2112–L2114, 1989.

[43] S. Nakamura, T. Mukai, M. Senoh, and N. Iwasa, "Thermal Annealing Effects on P–Type Mg–Doped GaN Films," *Jpn. J. Appl. Phys.*, vol. 31, pp. L139–L142, 1992.

[44] M. Knoll and E. Ruska, "Das Elektronenmikroskop," *Z. Phys.*, vol. 78, pp. 318–339, 1932.

[45] "Basic principal of transmission electron microscope," 2018. [Online; accessed 26-Mar-2018].

[46] G. S. Marlow and M. B. Das, "The effects of contact size and non–zero metal resistance on the determination of specific contact resistance," *Solid State Electron.*, vol. 25, pp. 91 – 94, 1982.

[47] S. Choi, *GROWTH AND CHARACTERIZATION OF III–NITRIDE MATERIALS FOR HIGH EFFICIENCY OPTOELECTRONIC DEVICES BY METALORGANIC CHEMICAL VAPOR DEPOSITION* . PhD thesis, Georgia Institute of Technology, 2012.

[48] M. A. Moram and M. E. Vickers, "X–ray diffraction of III–nitrides," *Rep. Prog. Phys.*, vol. 72, p. 036502, 2009.

[49] P. F. Fewster and N. L. Andrew, "Strain analysis by X–ray diffraction," *Thin Solid Films*, vol. 319, pp. 1 – 8, 1998.

[50] B. Cheng, S. Choi, J. E. Northrup, Z. Yang, C. Knollenberg, M. Teepe, T. Wunderer, C. L. Chua, and N. M. Johnson, "Enhanced vertical and lateral hole transport in high aluminum–containing AlGaN for deep ultraviolet light emitters," *Appl. Phys. Lett.*, vol. 102, p. 231106, 2013.

[51] M. Satter, Z. Lochner, T.-T. Kao, Y.-S. Liu, X.-H. Li, S.-C. Shen, R. Dupuis, and P. Yoder, "AlGaN–Based Vertical Injection Laser Diodes Using Inverse Tapered p–Waveguide for Efficient Hole Transport," *IEEE J. Quantum Elect.*, vol. 50, p. 166, 2014.

[52] H. Yoshida, Y. Yamashita, M. Kuwabara, and H. Kan, "Demonstration of an ultraviolet 336 nm AlGaN multiple–quantum–well laser diode," *Appl. Phys. Lett.*, vol. 93, p. 241106, 2008.

[53] A. Rice, R. Collazo, J. Tweedie, R. Dalmau, S. Mita, J. Xie, and Z. Sitar, "Surface preparation and homoepitaxial deposition of AlN on (0001)–oriented AlN substrates by metalorganic chemical vapor deposition," *J. Appl. Phys.*, vol. 108, p. 043510, 2010.

[54] R. D. Dupuis and P. D. Dapkus, "Room-temperature operation of distributed-Bragg-confinement $Ga_{1-x}Al_xAs$-GaAs lasers grown by metalorganic chemical vapor deposition," *Appl. Phys. Lett.*, vol. 33, p. 68, 1978.

[55] K. E. Waldrip, J. Han, J. J. Figiel, H. Zhou, E. Makarona, and A. V. Nurmikko, "Stress engineering during metalorganic chemical vapor deposition of AlGaN/GaN distributed Bragg reflectors," *Appl. Phys. Lett.*, vol. 78, p. 3205, 2001.

[56] G. S. Huang, T. C. Lu, H. H. Yao, H. C. Kuo, S. C. Wang, C.-W. Lin, and L. Chang, "Crack–free GaN/AlN distributed Bragg reflectors incorporated with GaN/AlN superlattices grown by metalorganic chemical vapor deposition," *Appl. Phys. Lett.*, vol. 88, p. 061904, 2006.

[57] J.-F. Carlin, J. Dorsaz, E. Feltin, R. Butté, N. Grandjean, M. Ilegems, and M. Laügt, "Crack–free fully epitaxial nitride microcavity using highly reflective AlInNGaN Bragg mirrors," *Appl. Phys. Lett.*, vol. 86, p. 031107, 2005.

[58] M. Abid, T. Moudakir, Z. Djebbour, G. Orsal, S. Gautier, A. E. Naciri, A. Migan-Dubois, and A. Ougazzaden, "Blue–violet boron–based Distributed Bragg Reflectors for VCSEL application," *J. Cryst. Growth*, vol. 315, p. 283, 2011.

[59] M. Abid, T. Moudakir, G. Orsal, S. Gautier, A. En Naciri, Z. Djebbour, J.-H. Ryou, G. Patriarche, L. Largeau, H. J. Kim, Z. Lochner, K. Pantzas, D. Alamarguy, F. Jomard, R. D. Dupuis, J.-P. Salvestrini, P. L. Voss, and A. Ougazzaden, "Distributed Bragg reflectors based on diluted boron–based BAlN alloys for deep ultraviolet optoelectronic applications," *Appl. Phys. Lett.*, vol. 100, p. 051101, 2012.

[60] T. Mitsunari, T. Tanikawa, Y. Honda, M. Yamaguchi, and H. Amano, "AlN/air distributed Bragg reflector by GaN sublimation from microcracks of AlN ," *J. Cryst. Growth*, vol. 370, p. 16, 2013.

[61] D. Chen and J. Han, "High reflectance membrane–based distributed Bragg reflectors for GaN photonics," *Appl. Phys. Lett.*, vol. 101, p. 221104, 2012.

[62] M. Arita, M. Nishioka, and Y. Arakawa, "InGaN Vertical Microcavity LEDs with a Si–Doped AlGaN/GaN Distributed Bragg Reflector," *Phys. Status Solidi (a)*, vol. 194, pp. 403–406, 2002.

[63] R. Goldhahn, C. Buchheim, P. Schley, A. T. Winzer, and H. Wenzel, *Optical Constants of Bulk Nitrides*, pp. 95–115. Wiley-VCH Verlag GmbH & Co. KGaA, 2007.

[64] J. F. Muth, J. H. Lee, I. K. Shmagin, R. M. Kolbas, H. C. C. Jr., B. P. Keller, U. K. Mishra, and S. P. DenBaars, "Absorption coefficient, energy gap, exciton binding energy, and recombination lifetime of GaN obtained from transmission measurements," *Appl. Phys. Lett.*, vol. 71, pp. 2572–2574, 1997.

[65] J. Piprek, H. Wenzel, and M. Kneissl, "Analysis of wavelength–dependent performance variations of GaN–based ultraviolet lasers," *Proc. SPIE*, vol. 6766, pp. 67660H–67660H–8, 2007.

[66] T.-C. Lu, C.-C. Kao, H.-C. Kuo, G.-S. Huang, and S.-C. Wang, "CW lasing of current injection blue GaN–based vertical cavity surface emitting laser," *Appl. Phys. Lett.*, vol. 92, p. 141102, 2008.

[67] Y.-S. Liu, A. F. M. S. Haq, T.-T. Kao, K. Mehta, S.-C. Shen, T. Detchprohm, P. D. Yoder, R. D. Dupuis, H. Xie, and F. A. Ponce, "Electrically conducting n–type AlGaN/GaN distributed Bragg reflectors grown by metalorganic chemical vapor deposition," *J. Crys. Growth*, vol. 443, pp. 81 – 84, 2016.

[68] H. Li, T. C. Sadler, and P. J. Parbrook, "AlN heteroepitaxy on sapphire by metalorganic vapour phase epitaxy using low temperature nucleation layers," *J. Crys. Growth*, vol. 383, pp. 72 – 78, 2013.

[69] T. Wang, K. B. Lee, J. Bai, P. J. Parbrook, R. J. Airey, Q. Wang, G. Hill, F. Ranalli, and A. G. Cullis, "Greatly improved performance of 340nm light emitting diodes using a very thin GaN interlayer on a high temperature AlN buffer layer," *Appl. Phys. Lett.*, vol. 89, p. 081126, 2006.

[70] S. Bals, B. Kabius, M. Haider, V. Radmilovic, and C. Kisielowski, "Annular dark field imaging in a {TEM} ," *Solid State Commun.*, vol. 130, pp. 675 – 680, 2004.

[71] Z. Ren, Q. Sun, S.-Y. Kwon, J. Han, K. Davitt, Y. K. Song, A. V. Nurmikko, H.-K. Cho, W. Liu, J. A. Smart, and L. J. Schowalter, "Heteroepitaxy of AlGaN on bulk AlN substrates for deep ultraviolet light emitting diodes," *Appl. Phys. Lett.*, vol. 91, p. 051116, 2007.

[72] J. D. Acord, S. Raghavan, D. W. Snyder, and J. M. Redwing, "In situ stress measurements during {MOCVD} growth of AlGaN on SiC ," *J Crys. Growth*, vol. 272, pp. 65 – 71, 2004.

[73] H. E. Bennett and J. O. Porteus, "Relation Between Surface Roughness and Specular Reflectance at Normal Incidence," *J. Opt. Soc. Am.*, vol. 51, pp. 123–129.

[74] B. Liu, R. Zhang, J. G. Zheng, X. L. Ji, D. Y. Fu, Z. L. Xie, D. J. Chen, P. Chen, R. L. Jiang, and Y. D. Zheng, "Composition pulling effect and strain relief mechanism in AlGaN/AlN distributed Bragg reflectors," *Appl. Phys. Lett.*, vol. 98, p. 261916, 2011.

[75] T. Gibbon, K. Prince, T. Pham, A. Tatarczak, C. Neumeyr, E. Rnneberg, M. Ortsiefer, and I. T. Monroy, "VCSEL transmission at 10Gb/s for 20km single mode fiber WDM–PON without dispersion compensation or injection locking," *Opt. Fiber Technol.*, vol. 17, pp. 41 – 45, 2011.

[76] P. Moser, J. A. Lott, P. Wolf, G. Larisch, A. Payusov, N. N. Ledentsov, W. Hofmann, and D. Bimberg, "99 fJ/(bit·km) Energy to Data–Distance Ratio at 17 Gb/s Across 1 km of Multimode Optical Fiber With 850–nm Single–Mode VCSELs," *IEEE Photonics Tech. Lett.*, vol. 24, pp. 19–21, 2012.

[77] P. Schnitzer, M. Grabherr, R. Jager, F. Mederer, R. Michalzik, D. Wiedenmann, and K. J. Ebeling, "GaAs VCSEL's at λ=780 and 835 nm for short–distance 2.5–Gb/s plastic optical fiber data links," *IEEE Photonics Tech. Lett.*, vol. 11, pp. 767–769, 1999.

[78] R. Zhou, E. Li, H. Li, P. Wang, and J. Yao, "Continuous–wave, 15.2 W diode–end–pumped Nd:YAG laser operating at 946 nm," *Opt. Lett.*, vol. 31, pp. 1869–1871, 2006.

[79] L. Goldberg, C. McIntosh, and B. Cole, "VCSEL end–pumped passively Q–switched Nd:YAG laser with adjustable pulse energy," *Opt. Express*, vol. 19, pp. 4261–4267, 2011.

[80] Y. P. Lan, Y.-F. Chen, K. F. Huang, H. C. Lai, and J. S. Pan, "Oxide–confined vertical–cavity surface–emitting laser pumped Nd:YVO_4 microchip lasers," *IEEE Photonics Tech. Lett.*, vol. 14, pp. 272–274, 2002.

[81] M. J. Mescher, R. Lutwak, and M. Varghese, "An ultra–low–power physics package for a chip–scale atomic clock," in *The 13th International Conference on Solid-State Sensors, Actuators and Microsystems, 2005. Digest of Technical Papers.*, vol. 1, pp. 311–316, 2005.

[82] S. Knappe, P. Schwindt, V. Shah, L. Hollberg, J. Kitching, L. Liew, and J. Moreland, "A chip–scale atomic clock based on 87Rb with improved frequency stability," *Opt. Express*, vol. 13, pp. 1249–1253, 2005.

[83] R. Lutwak, P. Vlitas, M. Varghese, M. Mescher, D. K. Serkland, and G. M. Peake, "The MAC – a miniature atomic clock," in *Proceedings of the 2005 IEEE International Frequency Control Symposium and Exposition, 2005.*, p. 6, 2005.

[84] D. K. Serkland, G. M. Peake, K. M. Geib, R. Lutwak, R. M. Garvey, M. Varghese, and M. Mescher, "VCSELs for atomic clocks," *Proc. SPIE*, vol. 6132, p. 6132, 2006.

[85] Y.-S. Liu, A. F. M. S. Haq, T.-T. Kao, K. Mehta, S.-C. Shen, T. Detchprohm, P. D. Yoder, R. D. Dupuis, H. Xie, and F. A. Ponce, "Electrically conducting n-type AlGaN/GaN distributed Bragg reflectors grown by metalorganic chemical vapor deposition," *J. Cryst. Growth*, vol. 443, pp. 81 – 84, 2016.

[86] G. Brummer, D. Nothern, A. Y. Nikiforov, and T. D. Moustakas, "Deep ultraviolet distributed Bragg reflectors based on graded composition AlGaN alloys," *Appl. Phys. Lett.*, vol. 106, p. 221107, 2015.

[87] W.-J. Liu, X.-L. Hu, L.-Y. Ying, J.-Y. Zhang, and B.-P. Zhang, "Room temperature continuous wave lasing of electrically injected GaN–based vertical cavity surface emitting lasers," *Appl. Phys. Lett.*, vol. 104, p. 251116, 2014.

[88] J. M. Redwing, D. A. S. Loeber, N. G. Anderson, M. A. Tischler, and J. S. Flynn, "An optically pumped GaNAlGaN vertical cavity surface emitting laser," *Appl. Phys. Lett.*, vol. 69, pp. 1–3, 1996.

[89] H. Zhou, M. Diagne, E. Makarona, A. Nurmikko, J. Han, K. Waldrip, and J. Figiel, "Near ultraviolet optically pumped vertical cavity laser," *Electron. Lett.*, vol. 36, pp. 1777–1779, 2000.

[90] T.-T. Kao, Y.-S. Liu, M. Satter, X.-H. Li, Z. Lochner, P. D. Yoder, T. Detchprohm, R. D. Dupuis, S.-C. Shen, J.-H. Ryou, A. M. Fischer, Y. Wei, H. Xie, and F. A. Ponce, "Sub–250nm low–threshold deep–ultraviolet AlGaN–based heterostructure laser employing HfO_2/SiO_2 dielectric mirrors," *Appl. Phys. Lett.*, vol. 103, p. 211103, 2013.

[91] J. M. Dallesasse, N. Holonyak, A. R. Sugg, T. A. Richard, and N. El-Zein, "Hydrolyzation oxidation of $Al_xGa_{1x}As$-AlAs-GaAs quantum well heterostructures and superlattices," *Appl. Phys. Lett.*, vol. 57, p. 2844, 1990.

[92] J. M. Dallesasse and N. Holonyak, "Native-oxide stripe-geometry $Al_xGa_{1x}As$-GaAs quantum well heterostructure lasers," *Appl. Phys. Lett.*, vol. 58, p. 394, 1991.

[93] K. Choquette, R. Schneider, K. Lear, and K. Geib, "Low threshold voltage vertical–cavity lasers fabricated by selective oxidation," *Electron. Lett.*, vol. 30, p. 2043, 1994.

[94] K. D. Choquette, K. L. Lear, R. P. Schneider, K. M. Geib, J. J. Figiel, and R. Hull, "Fabrication and performance of selectively oxidized vertical–cavity lasers," *IEEE Photonic. Tech. L.*, vol. 7, p. 1237, 1995.

[95] D. L. Huffaker, D. G. Deppe, K. Kumar, and T. J. Rogers, "Native-oxide defined ring contact for low threshold vertical-cavity lasers," *Appl. Phys. Lett.*, vol. 65, p. 97, 1994.

[96] N. J. Watkins, G. W. Wicks, and Y. Gao, "Oxidation study of GaN using x–ray photoemission spectroscopy," *Appl. Phys. Lett.*, vol. 75, p. 2602, 1999.

[97] E. D. Readinger, S. D. Wolter, D. L. Waltemyer, J. M. Delucca, S. E. Mohney, B. I. Prenitzer, L. A. Giannuzzi, and R. J. Molnar, "Wet thermal oxidation of GaN," *J. Electron. Mater.*, vol. 28, p. 257, 1999.

[98] B.-S. Cheng, Y.-L. Wu, T.-C. Lu, C.-H. Chiu, C.-H. Chen, P.-M. Tu, H.-C. Kuo, S.-C. Wang, and C.-Y. Chang, "High Q microcavity light emitting diodes with buried AlN current apertures," *Appl. Phys. Lett.*, vol. 99, p. 041101, 2011.

[99] J. Dorsaz, H.-J. Bhlmann, J.-F. Carlin, N. Grandjean, and M. Ilegems, "Selective oxidation of AlInN layers for current confinement in III–nitride devices," *Appl. Phys. Lett.*, vol. 87, p. 072102, 2005.

[100] C.-M. Lee, C.-C. Chuo, Y.-C. Liu, I.-L. Chen, and J.-I. Chyi, "InGaN–GaN MQW LEDs with current blocking layer formed by selective activation," *IEEE Electr. Device L.*, vol. 25, p. 384, 2004.

[101] Y.-S. Liu, A. F. M. S. Haq, K. Mehta, T.-T. Kao, S. Wang, H. Xie, S.-C. Shen, P. D. Yoder, F. A. Ponce, T. Detchprohm, and R. D. Dupuis, "Optically pumped vertical–cavity surface–emitting laser at 374.9 nm with an electrically conducting *n*–type distributed Bragg reflector," *Appl. Phys. Express*, vol. 9, p. 111002.

[102] Y. Xi and E. F. Schubert, "Junction-temperature measurement in GaN ultraviolet light–emitting diodes using diode forward voltage method," *Appl. Phys. Lett.*, vol. 85, pp. 2163–2165, 2004.

[103] D. S. Meyaard, J. Cho, E. F. Schubert, S.-H. Han, M.-H. Kim, and C. Sone, "Analysis of the temperature dependence of the forward voltage characteristics of GaInN light-emitting diodes," *Appl. Phys. Lett.*, vol. 103, p. 121103, 2013.

[104] B. Monemar, "Fundamental energy gap of GaN from photoluminescence excitation spectra," *Phys. Rev. B*, vol. 10, pp. 676–681, 1974.

[105] N. Watanabe, T. Kimoto, and J. Suda, "Thermo-Optic Coefficients of 4H-SiC, GaN, and AlN for Ultraviolet to Infrared Regions up to 500 °C," *Jpn. J. Appl. Phys.*, vol. 51, p. 112101, 2012.

[106] T. Honda, A. Katsube, T. Sakaguchi, F. Koyama, and K. Iga, "Threshold Estimation of GaN–Based Surface Emitting Lasers Operating in Ultraviolet Spectral Region," *Jpn. J. Appl. Phys.*, vol. 34, p. 3527, 1995.

[107] M. H. Crawford, A. A. Allerman, A. M. Armstrong, M. L. Smith, and K. C. Cross, "Laser diodes with 353 nm wavelength enabled by reduced–dislocation–density AlGaN templates," *Applied Physics Express*, vol. 8, p. 112702, 2015.

[108] C. Buchheim, R. Goldhahn, M. Rakel, C. Cobet, N. Esser, U. Rossow, D. Fuhrmann, and A. Hangleiter, "Dielectric function and critical points of the band structure for AlGaN alloys," *Phys. Status Solidi B*, vol. 242, pp. 2610–2616, 2005.